UNIVERSIDADE ESTADUAL DE CAMPINAS
FACULDADE DE ENGENHARIA MECÂNICA
E INSTITUTO DE GEOCIÊNCIAS

BENARD OLUSEGUN AKINMUDA

FORWARD TIME LAPSE SEISMIC MODELING FROM NUMERICAL SIMULATION MODELS

MODELAGEM SÍSMICA DE LAPSO DE TEMPO AVANÇADO A PARTIR DE MODELOS DE SIMULAÇÃO NUMÉRICA

CAMPINAS
2025

BENARD OLUSEGUN AKINMUDA

FORWARD TIME LAPSE SEISMIC MODELING FROM NUMERICAL SIMULATION MODELS

MODELAGEM SÍSMICA DE LAPSO DE TEMPO AVANÇADO A PARTIR DE MODELOS DE SIMULAÇÃO NUMÉRICA

Dissertation presented to the Mechanical Engineering Faculty and Geosciences Institute of the University of Campinas in partial fulfillment of the requirements for the degree of Master in Petroleum Science and Engineering in the area of Reservoirs and Management.

Dissertação de Mestrado apresentada à Faculdade de Engenharia Mecânica e Instituto de Geociências da Universidade Estadual de Campinas como parte dos requisitos exigidos para obtenção do título de Mestre em Ciências e Engenharia de Petróleo, na área de Reservatórios e Gestão.

Orientador: Profa. Dra. Alessandra Davólio Gomes
Coorientador: Dra. Daiane Rossi Rosa Lessa

Este exemplar corresponde à versão final da Dissertação defendida pelo aluno Benard Olusegun Akinmuda e orientadora pelo Profa. Dra. Alessandra Davólio Gomes.

CAMPINAS

2025

Ficha catalográfica
Universidade Estadual de Campinas (UNICAMP)
Biblioteca da Área de Engenharia e Arquitetura
Rose Meire da Silva - CRB 8/5974

Ak52f

Akinmuda, Olusegun Benard, 1989-
Forward time lapse seismic modeling from numerical simulation models / Olusegun Benard Akinmuda. – Campinas, SP : [s.n.], 2025.

Orientador: Alessandra Davolio Gomes.
Coorientador: Daiane Rossi Rosa Lessa.
Dissertação (mestrado) – Universidade Estadual de Campinas (UNICAMP), Faculdade de Engenharia Mecânica.
Em regime multiunidades com: Instituto de Geociências.

1. Prospecção sísmica - Modelos matemáticos. 2. Reservatórios (Simulação). 3. Sismologia. 4. Análise de forma de onda. 5. Tomografia sísmica. I. Gomes, Alessandra Davolio, 1980-. II. Lessa, Daiane Rossi Rosa, 1986-. III. Universidade Estadual de Campinas (UNICAMP). Faculdade de Engenharia Mecânica. IV. Título.

Informações complementares

Título em outro idioma: Modelagem sísmica de lapso de tempo avançado a partir de modelos de simulação numérica
Palavras-chave em inglês:
Seismic prospecting - Mathematical models
Reservoirs (Simulation)
Seismology
Waveform analysis
Seismic tomography
Área de concentração: Reservatórios e Gestão
Titulação: Mestra em Ciências e Engenharia de Petróleo
Banca examinadora:
Alessandra Davolio Gomes [Orientador]
Célio Maschio
João Paulo Pereira Nunes
Data de defesa: 23-01-2025
Programa de Pós-Graduação: Ciências e Engenharia de Petróleo

Objetivos de Desenvolvimento Sustentável (ODS)
Não se aplica

Identificação e informações acadêmicas do(a) aluno(a)
- ORCID do autor: https://orcid.org/0009-0005-5592-1434
- Currículo Lattes do autor: http://lattes.cnpq.br/6456267424387491

Profa. Dra. Alessandra Davólio Gomes, Presidente
REIT – Unicamp

Prof. Dr. Célio Maschio
Centro de Estudo de Petróleo – Unicamp

Dr. João Paulo Pereira Nunes
Technical Advisor (Geomechanics/Geophysics) – Petrobras, Brasil

A Ata de Defesa com as respectivas assinaturas dos membros encontra-se no SIGA/Sistema de Fluxo de Dissertação/Tese e na Secretaria do Programa da Unidade.

DEDICATION

This Dissertation is dedicated to Almighty God, my parents and my loved ones.

ACKNOWLEDGMENTS

I express my profound gratitude to the Almighty God for His unwavering affection, nurturing, and direction bestowed upon me, as well as for affording me the priceless opportunity to develop these competencies.

I wish to articulate my heartfelt gratitude to my esteemed supervisor, Prof. Dr. Alessandra Davolio, for her steadfast support and mentorship, alongside the provision of exceptional resources, knowledge, opportunities, and thought-provoking projects. She epitomizes the qualities of knowledge, humility, benevolence, and exemplary leadership. She will forever occupy a cherished position in my heart.

I am particularly appreciative of my co-supervisor, Dr. Daiane Rosa, for her encouragement, the privilege of joining the group, and her commitment to sharing her invaluable expertise. I will eternally acknowledge your significant contributions. I also wish to convey my appreciation to the Coordinator of Research in Reservoir Simulation and Management, Prof. Dr. Denis José Schiozer, and my esteemed professors: Dr. Célio Maschio, Dr. Michelle Avansi, Dr. Guilherme Daniel Avansi, Dr. João Carlos Von Hohendorff Filho, Dr. Manuel Gomes Correia, Dr. Alessandro Batezelli, Dr. Alexandre Campane, Vidal, Dr. Emilson Leite, and Dr. Rosangela Barros, for their support, contributions, and the knowledge imparted throughout my academic journey. May divine blessings be upon them all (Amen).

To my research group, I express my gratitude for your unwavering assistance and responsiveness to inquiries; thank you for the enriching discussions and contributions to both my work and our collective projects. I also extend my appreciation to the administrative staff, particularly Guilherme Roberto Tonin, and the IT support team who consistently demonstrate readiness to assist.

This research endeavor was conducted in conjunction with the ongoing project registered under ANP number 23095-3, titled “Seismic forward modeling tool for reservoir monitoring and CO2 injection and storage projects (RESSIMFORM CO2) (UNICAMP/DeepSoft/Repsol Sinopec Brasil/ANP) funded by Repsol Sinopec Brasil Ltda. I am thankful for the support received from the Center for Petroleum Studies (CEPETRO-UNICAMP/Brazil), the Department of Energy (DE-FEM-UNICAMP/Brazil), the Research Group in Reservoir Simulation and Management (UNISIM-UNICAMP/Brazil), and Energi Simulation. Furthermore, I extend special thanks to Marcos Sebastião, Guenther Schwedersky, and Lúcia Duarte Dillon for their technical guidance and insightful discussions throughout the

duration of the project. I also express my gratitude to SLB, CMG, and GeoSoftware for the provision of software licenses.

To my late father, Henry Olatunde Akinmuda, thank you for instilling in me the principles of diligence and integrity. To my mother, Grace Bola Akinmuda, I am deeply appreciative of your efforts in ensuring I received the highest quality education. To my aunt, Oluwafunmilayo Ayetiran, for her unwavering support and prayers.

To my cherished friends, your steadfast support holds immense significance for me: Marx Vladimir, João Ricardo, Salomon Dominique, Sadeeq Bello, Ali Rezaei Nayeh, Andrés Peralta, Jose Maria Herrera thank you for your unconditional friendship. Isabela Magalhães, I appreciate your continual reminders of Jesus Christ and His love for humanity. I extend my heartfelt thanks to all for your enduring support. I value each and every one of you. May divine blessings be upon you all.

RESUMO

A modelagem sísmica direta é um processo que gera dados sísmicos sintéticos a partir de dados de registro de poços ou modelos de simulação de reservatórios. No segundo caso, esse processo permite o acesso à qualidade dos modelos comparando amplitudes sísmicas sintéticas com dados medidos. Para garantir comparações precisas, é essencial definir as propriedades elásticas das rochas não reservatórios, bem como dos intervalos de sobrecarga e subcarga (localizados acima e abaixo do reservatório de interesse). Este estudo tem como objetivo avaliar a modelagem sísmica 4D em um reservatório real, comparando três abordagens para melhor comparar os dados sísmicos observados e simulados, focando especificamente nos reservatórios complexos dos arenitos siliciclásticos do Mioceno da bacia de Campos. Exploramos três cenários distintos de modelagem: modelagem direta tradicional com um valor constante de impedância acústica na sobrecarga e na subcarga (FMCOU); modelagem direta tradicional usando resultados de inversão para definir sobrecarga e subcarga (FMIOU); e modelagem direta a partir do resultado da inversão (FMFI). A fase inicial do nosso fluxo de trabalho envolve a realização de um estudo de viabilidade 1D na escala do poço com base no método de substituição de fluidos de Gassman para avaliar a força dos sinais 4D em diferentes cenários de produção. Em seguida, avançamos para o domínio da simulação e empregamos um modelo petroelástico para calcular as propriedades elásticas, como impedâncias acústicas e de cisalhamento. Além disso, aplicamos um modelo de velocidade ao modelo de simulação para conversão de profundidade para tempo, facilitando a transferência de escala para dados sísmicos e convertendo as propriedades de impedância em cubos sísmicos. Em nossa modelagem sísmica 4D, traços sísmicos sintéticos são criados calculando perfis de refletividade a partir das impedâncias acústicas em ângulo de incidência zero para diferentes datas, correspondentes aos levantamentos sísmicos adquiridos da base e monitor. Esses perfis são então convolvidos com uma wavelet, que é estimada estatisticamente a partir dos dados sísmicos post-stack adquiridos no levantamento da base. A modelagem sísmica foi realizada em dois intervalos de tempo de simulação correspondentes aos anos de 2006 (antes da produção) e 2012, que correspondem às datas dos levantamentos sísmicos adquiridos. Nas abordagens FMCOU e FMIOU, as amplitudes da base e do monitor são calculadas usando os resultados da

simulação por meio do fluxo de trabalho descrito. No FMFI, as amplitudes da base são calculadas a partir da inversão sísmica, enquanto os dados do monitor são calculados somando às impedâncias da base o delta deimpedância acústica obtido a partir da modelagem petroelástica. Os resultados obtidos de FMCOU, FMIOU e FMFI são comparados com os dados sísmicos observados, o que nos permitiu destacar regiões de ajustes bons/ruins entre eles e fornecer informações sobre o modelo de reservatório. Nossas descobertas indicam que os resultados 3D do FMIOU e do FMFI se alinham melhor com a sísmica real, mas na análise 4D as diferentes abordagens não têm impacto. As amplitudes 4D modeladas de FMCOU e FMIOU são idênticas e muito semelhantes às do FMFI, mostrando uma correspondência justa com a sísmica real.

Palavras-chave: modelagem sísmica direta, sísmica 4D, simulação de reservatório, sísmica para simulação, modelo de reservatório, modelo petroelástico.

ABSTRACT

Seismic forward modeling is a process that generates synthetic seismic data from well log data or reservoir simulation models. In the second case, this process enables the access of models' quality by matching synthetic seismic amplitudes with measured data. To ensure accurate comparisons, it is essential to define the elastic properties of non-reservoir rocks, as well as of the overburden and underburden intervals (located above and below the reservoir of interest). This study aims to evaluate 4D seismic forward modeling in a real reservoir by comparing three approaches to better match observed and simulated seismic data, specifically focusing on the complex reservoirs of the Campos basin's siliciclastic Miocene sandstones. We explore three distinct modeling scenarios: traditional forward modeling with a constant value of acoustic impedance in the overburden and underburden (FMCOU); traditional forward modeling using inversion results to define overburden and underburden (FMIOU); and forward modeling from inversion result (FMFI). The initial phase of our workflow involves conducting a 1D feasibility study at the well scale based on Gassman's fluid substitution method to evaluate the strength of 4D signals across different production scenarios. We then progress to the simulation domain and employ a petro-elastic model to calculate the elastic properties such as acoustic and shear impedances. Additionally, we apply a velocity model to the simulation model for depth-to-time conversion, facilitating scale transference to seismic data and converting the impedance properties into seismic cubes. In our 4D seismic modeling, synthetic seismic traces are created by calculating reflectivity profiles from the acoustic impedances at zero incident angle for different dates corresponding to the acquired base and monitor seismic surveys. These profiles are then convolved with a wavelet, which is statistically estimated from the full-stack seismic data acquired in the baseline survey. The seismic modeling was performed in two simulation timesteps corresponding to the years 2006 (before production) and 2012, which correspond to the dates of the acquired seismic surveys. In FMCOU and FMIOU approaches, the baseline and monitor amplitudes are calculated using simulation results through the described workflow. In FMFI, the amplitudes for the baseline are calculated from seismic inversion, while the monitor data is calculated by summing to the baseline the delta acoustic impedances obtained from petro-elastic modeling. The results obtained from FMCOU, FMIOU, and FMFI are compared

with the observed seismic data, which allowed us to highlight regions of good/bad mismatches between them and provide insights into the reservoir model. Our findings indicate that the 3D results from FMIOU and FMFI better align with the real seismic, but in the 4D analysis the different approaches do not have an impact. The modeled 4D amplitudes from FMCOU and FMIOU are identical and very similar to FMFI, showing a fair match with the real seismic.

Keywords: seismic forward modeling, 4D seismic, reservoir simulation, seismic to simulation, reservoir model, petro-elastic model.

LIST OF FIGURES

TABLE OF CONTENT

1 INTRODUCTION

The efficient management and optimal production of hydrocarbon reservoirs are critical aspects of the petroleum industry. To achieve these goals, geoscientists and reservoir engineers rely on various tools and techniques, one of which is time-lapse (4D) seismic monitoring. The concept of 4D seismic monitoring emerged in the late 1980s and early 1990s, driven by the need to better understand and manage reservoirs over their production life. Since then, 4D seismic technology has significantly improved reservoir monitoring, becoming an essential tool in the strategic management and optimization of oil and gas production. This technology enables the active tracking of changes in reservoir pressure and fluid saturation over time, providing insights that can serve to reduce models' uncertainties and improve decision-making for reservoir drainage strategies. The integration of 4D seismic data with dynamic reservoir models enhances the understanding of reservoir characteristics, crucial for effective management and maximized recovery.

Santos et al. (2022) proposed a fast-diagnostic approach using 4D seismic similarity indicators to accelerate the analysis and interpretation of reservoir simulation models. This development significantly speeds up the decision-making process by providing quick and accurate insights into reservoir dynamics by converting hundreds of models from the reservoir engineering domain to the seismic domain. Dillon et al. (2023) presents a comprehensive approach to enhance 4D Quality Indicator (QI) process through a case study of a Brazilian turbidite field. This research underscores the essential function of 4D seismic data in delineating the dynamic characteristics of complex deep-water reservoirs, proven particularly beneficial in illustrating fluid dynamics and pressure fluctuations within the Miocene turbidite field and suggesting promising avenues for future advancements in seismic data analysis and interpretation.

The integration between simulation models and seismic data requires modeling techniques that can simulate the expected seismic behavior based on reservoir properties and production scenarios. This process is called seismic forward modeling, which determines the seismic amplitudes of geological formations using simulation outputs. This method facilitates the comparison with the real seismic and plays a pivotal role in 4D feasibility studies, interpretation of 4D seismic data as well as reservoir models' update. Mello et al. (2019) conducted a feasibility study through 4D petro-elastic modeling in Brazilian Pre-Salt Fields to

examine how fluid variations influence the elastic attributes and seismic signatures. Formento et al. (2007) utilized refined seismic forward modeling techniques to develop a comprehensive workflow for 4D seismic modeling in the Marlim Field, a workflow that has since become a reference point for similar studies. Their approach involved calibrating the reservoir model by comparing the observed 4D seismic data with the synthetic response from dynamic simulations. By using this methodology, they were able to predict future 4D signatures and optimize the timing for subsequent seismic acquisitions.

This study focuses on time-lapse seismic modeling from numerical simulation of Albacora Leste (ABL) field, located in the Brazilian Campos basin. The aim is to assess the alignment between synthetic and acquired data, exploring how different modeling techniques impact reservoir signals. More specifically, in addition to evaluating the quality of the model, we aimed to investigate whether defining the overburden and underburden using different approaches would impact the modeled signals within the thin Albacora reservoir. We also sought to determine if adopting a more complex seismic forward modeling approach would be beneficial to the comparison with observed data. It is important to note that the analysis presented in this study applies specifically to reservoirs where compaction effects are negligible, as the tested methodologies do not account for compaction driven amplitude variations.

1.1 Motivation

This research is driven by the significant potential of integrating 4D seismic data with reservoir simulation models to unlock insights into the behavior of reservoirs. The motivation of this study is to improve the accuracy and reliability of seismic forward modeling, essential for aligning modeled and observed data. By comparing these data, we can refine production strategies, ensuring optimal reservoir management.

1.2 Aim/Objectives

The aim of this study is to evaluate different approaches for seismic forward modeling, using a simulation model of Albacora Leste in the Campos Basin. The objectives are

designed to identify the most effective forward modeling approach to achieve a closer alignment between modeled and observed 4D seismic data. Specifically, the research will:

Evaluate traditional forward modeling (FMCOU): This conventional approach involves applying a constant value of acoustic impedance in the overburden and underburden intervals to model the synthetic seismic volume.

1. **Integrate inversion results with traditional forward modeling (FMIOU):** This method improves upon the previous approach by integrating inversion results to define the overburden and underburden.

2. **Implement inversion-based forward modeling (FMFI):** A forward modeling technique that directly utilizes inversion results to model the synthetic seismic response for the baseline survey and petro-elastic impedance differences to obtain monitor data.

1.3 Contributions of Research to Knowledge

This work contributes to an improved confidence in performing seismic forward modeling from numerical simulation models by validating the model reliability through FMCOU, FMIOU, and FMFI approaches. This research will also analyze the 4D signals of the field, to increase confidence in reservoir characterization and help in the uncertainty reduction in production forecasts .

1.4 Thesis structure

This dissertation is structured in seven chapters. The first chapter is an introduction to time lapse 4D seismic, discussing the motivations behind this work, its objectives and contribution to knowledge. The second chapter provides a theoretical background to facilitate understanding of the key concepts necessary for forward time-lapse seismic modeling. A literature review of different methods for 4D seismic analysis is done in the third chapter. This explains how previous works integrates 4D seismic (4DS) into reservoir simulation models.

The project's methodology is described in detail in Chapter 4. It explores how engineering and seismic data are integrated to achieve the research objectives. The fifth chapter focuses on how the procedure described above is applied to the Albacora Leste field. It contains a thorough explanation of the data availability, field's location, geological environment,

stratigraphy, environment during deposition and production strategy. It also clarifies how these elements connect to 4D seismic qualitative interpretation.

The sixth chapter presents the outcomes of the integrated interpretation, showcasing the results derived from applying the proposed workflow to the study area. This includes an initial examination of seismic data, a 1D feasibility study, and analysis of P-impedances from petro-elastic modeling at two-time steps to evaluate expected 4D seismic signals. The section also discusses the impact of adding noise to the synthetic amplitudes to simulate realistic conditions and improve model alignment with observed data. The work is concluded in Chapter 7 with a summary of the findings and recommendations for additional research projects.

2 THEORETICAL BACKGROUND

This chapter provides an overview of 4D seismic data and its applications in reservoir monitoring and management. The 4D seismic, also known as time-lapse seismic, involves acquiring, processing, and interpreting 3D seismic surveys conducted at different time intervals over an oil or gas field. Each 3D survey provides a snapshot of the subsurface conditions at a specific time. By comparing data volumes acquired at different times, it becomes possible to identify changes in amplitudes caused by fluid movement and pressure variations. This happens because these changes affect the rocks' elastic properties and thus the seismic amplitudes recorded during the surveys. The access to fluid movement and pressure changes in the reservoir through 4D seismic analysis has significant implications for reservoir management.

The model-based interpretative framework, facilitated through simulation-to-seismic (sim2seis) modeling, serves as a mechanism for the validation and optimization of geological and simulation models. Amini (2014) characterizes simulation-to-seismic modeling as the procedure of generating synthetic seismic responses from a simulator at various stages of production. Seismic modeling is executed through two primary phases. Initially, reservoir parameters are transposed into seismic parameters, for instance, the saturated P-wave velocity or the density of the fluid mixture, utilizing rock physics models. Subsequently, synthetic seismic sections are computed based on these parameters (Fahimuddin et al. 2010). A variety of modeling methodologies exist, including simple 1D convolution and full-wavefield-based techniques; however, the most frequently reported methodology for sim2seis applications is 1D convolution (Ribeiro et al., 2007; Allo et al., 2013).

One-Dimensional (1D) convolution is a mathematical operation commonly used in seismic processing to model wave propagation by convolving a source wavelet with reflectivity series. Despite its widespread use, 1D convolution is limited in its ability to represent illumination, resolution, and acquisition effects. More especifically, this method, while fast and cost-effective, struggles to capture complex subsurface dynamics, such as local blurring, amplitude fidelity, and acquisition geometry limitations. To overcome these challenges, more sophisticated forward modeling techniques, such as finite difference (Fichtner, 2011) and ray tracing methods (Chapman, 2004), have been used. Finite difference modeling, as demonstrated by Amini et al. (2020), provides detailed wavefield simulations and superior lateral continuity

compared to 1D convolution. However, it is computationally demanding, often requiring several days for processing a single survey.

Ray tracing offers a balance between simplicity and computational demand. As an asymptotic approximation of the wave equation for high frequencies, ray tracing describes the kinematic and dynamic behavior of seismic waves by tracing their trajectories through subsurface layers (Červený, 2001). While more robust than 1D convolution, ray tracing is limited in its ability to handle high model complexities, such as faults and dikes, and requires seismic processing for effective implementation. These limitations make it less versatile in highly heterogeneous reservoirs.

Advanced forward modeling techniques have been applied extensively in challenging reservoir environments, such as the pre-salt fields offshore Brazil. For instance, Deplante et al. (2019) utilized full-wave seismic modeling to test 4D repeatability, focusing on both elastic and acoustic responses. Their study demonstrated the ability to detect depletion-induced velocity changes of approximately 1.5% and time shifts of around 1ms in thick reservoir intervals. Such high-resolution modeling provides valuable insights into production-induced reservoir changes, enabling more effective monitoring and optimization of field development strategies.

Despite the advancements in forward modeling techniques to significantly expand the capabilities of 4D seismic analysis in complex reservoirs, Amini et al. (2020) demonstrated that 1D convolution produces results comparable to more sophisticated approaches while being computationally efficient. Therefore, this approach will be employed in this study.

This dissertation focuses on changes in the magnitude of reflections, which are referred to as "hardening" when there is an increase in impedance (IP) from the baseline to the monitor survey, and "softening" when the IP decreases. Figure 2.1 visually illustrates the impact of an impedance increase caused by water replacing oil in a producing zone of the reservoir. The P-wave velocity and density change from the baseline (Figure 2.1a) to the monitor survey (Figure 2.1b) in the swept zone, leading to changes in reflection coefficients and amplitudes at the reservoir.

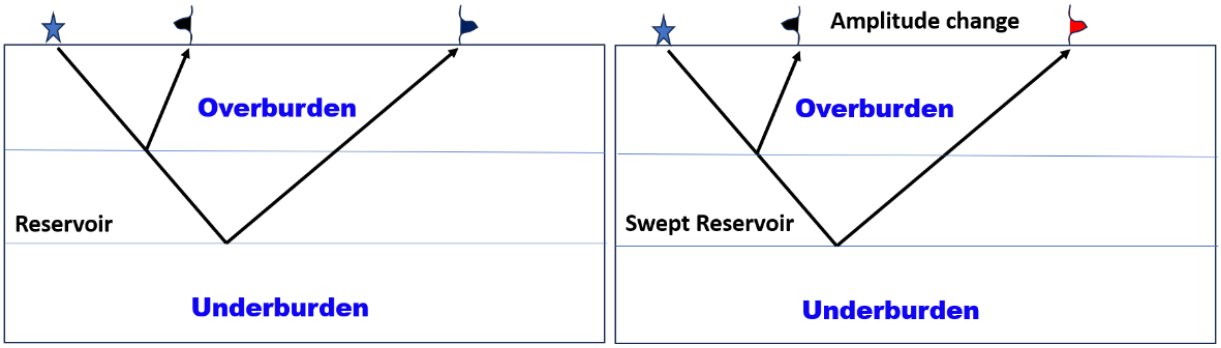

Figure 2.1: Pre-production baseline seismic survey (left) and monitor survey (right), recorded after waterflood production. The monitor detects the changes in amplitudes. Adapted from Johnston (2013).

2.1 Petro-elastic modeling (PEM)

Integrating seismic data with simulation models is crucial because it allows us to visualize and understand changes within the reservoir more accurately. By linking seismic data with simulation models, we can predict seismic responses based on current reservoir conditions. This integration enhances our ability to make reliable interpretations, track reservoir performance and model reliability, and make informed decisions in reservoir management. Petro-elastic modeling (PEM) provides a direct link between reservoir simulation outputs and seismic attributes by converting reservoir static and dynamic properties into rocks' elastic properties. The theoretical principles underlying PEM include, for instance, fluid substitution models, effective medium theories, and pressure sensitivity concepts. The Gassmann's fluid substitution theory (Gassmann 1951) estimates changes in the rock's elastic properties under varying fluid saturations based on the following fundamental assumptions:

- The rock must be homogeneous and isotropic, composed of the same minerals and grains making up the rock frame.
- The pore space should be completely connected and saturated, allowing fluid to flow and maintain pressure equilibrium.

Gassmann's equations relate the fluid-saturated bulk and shear moduli, as well as rock density, to the dry-rock-frame moduli, fluid bulk modulus, and porosity. Johnston (2013) presents Gassmann's equations as follows:

$$\frac{Ksat}{Kmin-Ksat} = \frac{Kdry}{Kmin-Kdry} + \frac{Kfl}{(Kmin-Kfl)\phi},$$

2.1

$$\mu sat = \mu dry,$$

2.2

$\rho sat = \rho dry + \phi \rho fl$

2.3

where Ksat, μsat and ρsat are the fluid-saturated bulk moduli, shear moduli and rock density, respectively; Kdry, μdry and ρdry are the dry-rock-frame bulk moduli, shear moduli and density, respectively; Kmin is the equivalent mineral bulk modulus of the solid mineral grains that form the rock frame; Kfl and ρfl are the fluid bulk modulus and density, respectively; and ø is the porosity. Kdry, Kmin, and ø are assumed to be constant before and after the fluid substitution. In practice, equation (2.1) is rearranged to solve for Kdry, given Kfl for the rock at the initial saturation state. Then it is solved for Ksat, given Kfl for the new saturation state (Johnston, 2013). The bulk modulus or incompressibility Ksat of an isotropic rock filled with a fluid is the ratio of hydrostatic stress to volumetric strain. The higher the bulk modulus the stiffer the rock. The shear modulus of an isotropic rock is the ratio of shear stress to shear strain; it is not affected by pore fill because shear waves do not travel through fluids (Simm & Bacon, 2014). The bulk and shear moduli of the saturated rock are shown in equations (2.4) and (2.5), and the P and S wave velocities are shown in equations (2.6) and (2.7).

$$Ksat = \rho sat\left(Vp^2 - \frac{4}{3}Vs^2\right) \quad 2.4$$

$$\mu sat = \rho sat \times Vs^2 \quad 2.5$$

$$Vp = \sqrt{\frac{Ksat + \frac{4}{3}\mu sat}{\rho sat}} \quad 2.6$$

$$Vs = \sqrt{\frac{\mu sat}{\rho sat}} \quad 2.7$$

$$IP = \rho sat \times Vp \quad 2.8$$

$$IS = \rho sat \times Vs \quad 2.9$$

2.1.1 Mineral moduli

Effective medium theory considers factors such as porosity, grain size, grain shape, and mineralogy to estimate how the combined properties of different minerals within a rock influence its overall elastic response. By integrating these factors, the theory provides a framework for understanding how individual mineral moduli (elastic properties) contribute to the rock's bulk and shear moduli (Mukerji & Dvorkin, 1998). The Voigt-Reuss bounds and Hashin–Shtrikman bounds, for example, are two distinct foundational approaches for determining the elastic moduli of composite minerals of reservoir rocks. These theories provide ways of estimating the effective bulk modulus and shear modulus of a rock matrix composed of different mineral components. The Voigt bound for bulk/shear moduli (M_V), Reuss bound for bulk/shear moduli (M_R) and Voigt-Reuss-Hill average of the bulk/shear moduli (M_{min}) are given by:

$$M_v = \sum_{i=1}^{N} v_i M_i \qquad 2.10$$

$$\frac{1}{M_R} = \sum_{i=1}^{N} \frac{v_i}{M_i} \qquad 2.11$$

$$M_{min} = \frac{M_V + M_R}{2} \qquad 2.12$$

where v_i is the volume fraction of i-th mineral, M_i can be either the bulk or the shear moduli of the i-th mineral, M_V is the Voigt bound for either the bulk or shear moduli, M_R is the Reuss bound for either the bulk or shear moduli and M_{min} is the average for either the bulk or shear moduli.

2.1.2 Fluid moduli

The properties of the fluids within the pore spaces such as the bulk modulus (Kfl) and the density (ρfl) are essential for understanding the rock fluid system. The Batzle-Wang equations provide a means to calculate the fluid properties based on their composition, temperature and pressure (Batzle & Wang 1992). The bulk modulus and the density of a heterogeneous mixture of fluids (patchy saturation) can be calculated using the Voigt average (Johnston, 2013):

$$K_{fl} = S_w K_w + S_o K_o + S_g K_g \qquad 2.13$$

$$\rho_{fl} = S_w \rho_w + S_o \rho_o + S_g \rho_g \qquad 2.14$$

where S_w, S_o, S_g, are the saturations of water, oil and gas, respectively, and K_w, K_o, K_g and ρ_w, ρ_o, ρ_g, are the bulk modulus and density of water, oil and gas, respectively.

2.1.3 Dry-rock moduli

The dry rock moduli are critical for understanding how the rock behaves under mechanical stress in a dry state, which is essential for various geophysical and engineering applications. The dry bulk modulus measures a rock's resistance to volumetric compression when subjected to pressure without considering fluid saturation. It quantifies how much the rock's volume decreases under applied pressure. The calculation of dry-rock moduli can be approached through several models, including the Uncemented and Unconsolidated Sand Models. The uncemented sand model is particularly relevant for granular materials such as unconsolidated sands where porosity and effective pressure play a significant role. This model grounded in Hertz-Mindlin contact theory predicts elastic moduli of uncemented granular materials under effective stress by assuming spherical grains and that cementation is deposited far from grain contacts (Mavko et al., 2020). The model accounts for coordination number (C) and grain properties to derive the dry rock moduli (Dvorkin & Nur, 1996). It also incorporates parameters such as critical porosity (ϕC), friction coefficient (FC), grain angularity (RR), and matrix stiffness index (MSI) to better characterize the granular medium (Allo, 2019).

In this method, the dry bulk modulus (K_{dry}) and shear modulus μ_{dry} are calculated as follows (Mavko et al., 2020):

$$K_{dry} = \left[\frac{C^2(1-\phi)^2\mu^2}{18\pi^2(1-\nu)^2}P\right]^{\frac{1}{3}} \quad 2.15$$

$$\mu_{dry} = \frac{5-4\nu}{5(2-\nu)}\left[\frac{3C^2(1-\phi)^2\mu^2}{2\pi^2(1-\nu)^2}P\right]^{\frac{1}{3}} \quad 2.16$$

where C is the Coordination number representing the average number of contacts per grain, ϕ is the porosity representing the void fraction in the granular pack, P is the effective pressure applied to the granular pack, ν is the poison ratio of the grain material and μ is the grain shear modulus. The extended unconsolidated sandstone model integrates a weighted modified Hashin-Shtrikman bound, which interpolates between the soft sandstone model (Dvorkin & Nur, 1996) and the stiff sandstone model (Mavko et al., 1998). The Matrix Stiffness Index

(MSI) serves as an interpolation weight, governing the transition between poorly consolidated and well-cemented formations. The weighted interpolation follows the equation:

$$M = MSI \times M_{stiff} + (1 - MSI) \times M_{soft} \quad 2.17$$

where M_{stiff} and M_{soft} represent the upper and lower Hashin-Shtrikman bounds respectively.

To calculate the effective bulk modulus (K_{eff}) and the shear modulus (μ_{eff}) for granular materials at different porosities (ϕ_n), the model uses the following(Mavko et al., 2020):

$$K_{eff} = \left[\frac{\frac{\phi_n}{\phi}}{K_{dry} + \frac{4}{3}\mu_{dry}} + \frac{1 - \frac{\phi_n}{\phi}}{K + \frac{4}{3}\mu_{dry}}\right]^{-1} - \frac{4}{3}\mu_{dry} \quad 2.18$$

$$\mu_{eff} = \left[\frac{\frac{\phi_n}{\phi}}{\mu_{dry} + \frac{\mu_{dry}}{6}\left(\frac{9K_{dry+}\,8\mu_{dry}}{K_{dry+}\,2\mu_{dry}}\right)} + \frac{1 - \frac{\phi_n}{\phi}}{\mu + \frac{\mu_{dry}}{6}\left(\frac{9K_{dry+}\,8\mu_{dry}}{K_{dry+}\,2\mu_{dry}}\right)}\right]^{-1} - \frac{\mu_{dry}}{6}\left(\frac{9K_{dry+}\,8\mu_{dry}}{K_{dry+}\,2\mu_{dry}}\right) \quad 2.19$$

where K is the bulk modulus of the grain material.

These equations provide reliable estimates for the effective elastic properties of granular materials under varying porosities and effective pressures, making them particularly suited for geophysical analyses of the extended unconsolidated sandstone model, which integrates both the soft sandstone model and the stiff sandstone model (Mavko et al., 1998). This integration is achieved by incorporating a weighted modified Hashin-Shtrikman bound, where the Matrix Stiffness Index (MSI) acts as the interpolation weight, controlling rock stiffness across different porosity conditions.

2.2 Seismic forward modeling and addition of noise

Seismic forward modeling involves predicting seismic responses based on a reservoir model. This process includes calculating synthetic seismic traces using the reflectivity profiles. Reflectivity is a measure of how seismic waves are reflected at boundaries between layers with different acoustic impedances. After the reflectivity profiles are computed, they are convolved with a seismic wavelet estimated from the actual seismic data. However, in this approach, the synthetic seismic responses often lack the inherent noise and uncertainties present in real-world seismic data. By adding seismic noise to the synthetic amplitudes, we can better simulate the complexities and challenges encountered when working with actual 4D seismic data and improve their comparison. The noise introduced in the synthetic data can include various types of noise, such as random noise, coherent noise, repeatability noise, and noise derived from the

residuals of inversion. The later provides a closer-to-reality noise simulation, capturing the wave propagation phenomena and acquisition problems occurring in the reservoir (Rosa et al. 2024).

2.3 Evaluating model's accuracy

It is crucial to assess the validity of a reservoir simulation model by juxtaposing the modeled data derived from it with the observed data. While production data remains a primary source of comparison, the use of 4D seismic data provided additional insights into fluid movement within the reservoir. Thus, the analysis of both data allows for a more informed decision on the accuracy and the need for refinement of the model. To systematically quantify the divergence between the observed and simulated production data, the Normalized Quadratic Distance with Sign (NQDS) is routinely employed (Cavalcante et al., 2017). NQDS evaluates the degree to which the simulated data corresponds with the observed data, considering not only the discrepancies between the two datasets but also the permissible range of error (tolerance) inherent in the observed data. As elucidated by Maschio & Schiozer (2016), there exists no universally accepted guideline for the selection of tolerance (Tol) and constant parameters (Cp), as these determinations are often contingent upon engineering discretion. The selection of parameters is shaped by the dependability of the observed data and the specific nature of the data under scrutiny. These are the formulations commonly used (Maschio & Schiozer, 2016):

$$NQDS = \frac{LD}{|LD|}\frac{QD}{AQD} \quad 2.19$$

$$QD = \sum_{i=1}^{n} (Sim_i - Hist_i)^2 \quad 2.20$$

$$AQD = \sum_{i=1}^{n} (Tol \times Hist_i + C_P)^2 \quad 2.21$$

$$LD = \sum_{i=1}^{n} (Sim_i - Hist_I) \quad 2.22$$

where AQD is the acceptable quadratic distance, QD is quadratic deviation and LD is the simple distance.

2.4 Seismic similarity measures

Repeatability is the measure of the similarity of two or more vintages of seismic data. In 4D seismic monitoring, achieving high repeatability is crucial for minimizing uncertainties in time-lapse interpretations and enhancing the effectiveness of 4D initiatives. Repeatability ensures that differences observed between surveys are due to actual reservoir changes rather than variations in acquisition parameters. Kragh & Christie (2002) emphasize that "seismic repeatability is essential for the success of time-lapse seismic surveys" and discuss methods to

quantify and improve it. Similarly, Calvert (2005) notes that "the success of 4D seismic monitoring depends on the ability to repeat seismic surveys with high precision", highlighting the importance of consistent acquisition conditions. A multitude of factors contributes to the presence of noise caused by repeatability issues, including variations in acquisition geometry, the specific types of equipment utilized for both sources and recording, the complexities inherent in the overburden, static shifts, imaging parameters, ambient noise, as well as environmental factors such as tidal fluctuations, salinity, and the presence of rigs. To attain repeatability, seismic data acquisition and processing methodologies must prioritize the reproducibility of seismic events within non-productive zones where seismic events should remain unchanged. While repeatability is vital in 4D seismic processing, it is important to note that many other factors and steps contribute to seismic data quality that are not addressed here. Metrics for assessing repeatability encompass the Normalized Root Mean Square difference (NRMS) and predictability (PRED), as elucidated by Kragh & Christie (2002). NRMS is one of the primary metrics for assessing repeatability. It measures the noise level between two seismic traces and reveals the quality of the seismic data. The formula for NRMS is:

$$\text{NRMS} = \frac{200 \times \text{RMS}(a_t - b_t)}{\text{RMS}(a_t) + \text{RMS}(b_t)} \quad 2.23$$

The RMS operator is defined as:

$$\text{RMS}(x_t) = \sqrt{\frac{\sum_{t_1}^{t_2}(x_t)^2}{N}} \quad 2.24$$

where N is the number of samples in the interval $t_1 - t_2$, x_t represents the amplitude of the seismic signal at a given time t and a_t and b_t represent the two seismic traces within the selected time window. NRMS values vary by acquisition type. In marine acquisitions, for example, streamer-type acquisitions often exhibit lower repeatability than permanent reservoir monitoring (PRM) acquisitions, resulting in higher NRMS values (dos Santos, 2015).

3 LITERATURE REVIEW

This chapter provides an overview of the relevant literature, focusing on key aspects of time-lapse seismic analysis, particularly its application in monitoring reservoir dynamics. The review will address topics such as qualitative and quantitative approaches to 4D seismic interpretation.

3.1 Qualitative application of 4D seismic data

The qualitative interpretation of 4D data has the potential to fulfill specific objectives, such as identifying bypassed or undrained zones, assessing sweep efficiencies, recognizing baffles, analyzing flood fronts, monitoring contact movement, evaluating connectivity, and examining fault sealing mechanisms. In such instances, it is customary to correlate seismic attributes with dynamic data, including production and injection fluid rates, variations in pressure, and cumulative production and injection volumes. This combination with engineering data addresses numerous reservoir management aims and aids in mitigating uncertainties.

Davolio et al. (2021) conducted a 4D feasibility analysis utilizing a synthetic carbonate reservoir model inspired by a pre-salt reservoir, concluding that the synthetic seismic data exhibited pronounced amplitude changes attributed to the presence of a volcanic rock nearby an injector well, which is anticipated due to its substantial impedance contrast with neighboring strata. The outcomes of the forward modeling also enabled the researchers to discern pronounced 4D signals associated with increments in pore pressure resulting from the injector wells, alongside variations in water and gas saturations surrounding the water alternating gas injection (WAG) wells. Webb et al. (2019) concluded that the execution of a 4D feasibility study facilitated the assessment of both the mechanisms and magnitude of the 4D effect, thereby providing a structured framework for the interpretation and application of 4D data upon its acquisition. Maleki et al. (2018) investigated the complexities linked to the interpretation of 4D seismic data in the Norne field, situated in the Norwegian Sea. The study emphasizes the importance of 4D seismic data in enhancing reservoir characterization and reducing uncertainties, particularly in distinguishing fluid movements from pressure changes. The authors illustrated how the interpretation of time-lapse seismic data can improve understanding of reservoir dynamics, contributing to more informed decision-making in field development. The use of amplitude data in this context was crucial for identifying production-induced changes and optimizing sweep efficiency within the reservoir. This approach underscored the

role of 4D seismic in providing valuable insights into reservoir performance and aiding in the reduction of subsurface uncertainties. Oliveira (2008) presents the application of 4D seismic technology to manage a reservoir in the Marlim Field. Their research shows how 4D seismic data helps track changes in reservoir conditions over time, giving a clearer and more detailed picture of the reservoir. The findings highlight the potential of 4D seismic technology to optimize well placement and improve production strategies. Furthermore, they show how 4D seismic data can help identify risks, such as water or gas breakthrough and fault reactivation, enabling proactive risk mitigation.

Calvert et al. (2016) provided an example that demonstrates how 4D seismic data can be used qualitatively to show how variations in porosity affect fluid movement across the reservoir, particularly in the Halfdan field. Their study highlighted the influence of localized changes in porosity on the efficiency of lateral sweep during production. Furthermore, the 4D data indicated the potential for certain faults to serve as ingress points for formation water into the oil-producing strata. Additionally, by synthesizing the 4D seismic data with geological and production information, numerous well-intervention opportunities were identified.

Mello et al. (2019) conducted a study on 4D petro-elastic modeling in Brazilian pre-salt carbonate reservoirs. Their research focused on generating synthetic 4D responses to evaluate production effects such as water flooding and gas injection. However, their work primarily targeted carbonate reservoirs, which differ significantly in geologic and petrophysical characteristics from the siliciclastic reservoirs studied here. While Mello et al. (2019) addressed carbonate reservoirs, this study focuses on siliciclastic Miocene sandstones in the Campos Basin.

3.2 Quantitative 4D seismic data integration

In quantitative 4D interpretation, seismic data is integrated with reservoir models to improve the history-matching process. This approach uses 4D seismic data not only for visualization but also as a tool to update reservoir models and improve the accuracy of predictions by reducing the error between modeled and observed seismic data. The integration of 4D seismic data into the data assimilation process has proven effective in refining dynamic reservoir models and enhancing the accuracy of fluid movement and pressure change predictions. Studies such as Rosa et al. (2023) and Emerick (2016) highlight how incorporating 4D seismic information improves the match between observed and simulated data, leading to better reservoir characterization and production forecasting. Integrating simulation and seismic

domains can be a complex process that involves various conversions, including seismic forward modeling and seismic inversions. Among the domains used for incorporating seismic data, seismic impedance is often the most familiar domain (Neto et al., 2021; Oliver et al., 2021). In this case, for the data to be comparable, it is required running a petro-elastic modeling using the simulation model output and executing a 4DS inversion to convert observed seismic amplitudes into impedance changes. Rosa et al. (2023) conducted a comprehensive investigation regarding the influence of 4D seismic in data assimilation to enhance reservoir models and the accuracy of production forecasts. Their study emphasized the importance of addressing seismic artefacts, such as side-lobe effects, that can distort seismic interpretations and hinder accurate monitoring of pressure and saturation changes happening due to hydrocarbon production. By applying various treatments to these artefacts, excluding unreliable data showed significant improvements in well and seismic matches, which also resulted in better production predictions. Davolio et al. (2013) introduced an approach for integrating 4D seismic data within the context of history matching, with particular emphasis on specific regions surrounding injection wells and their corresponding production wells. Instead of applying a global approach to match dynamic information across the entire reservoir, their method concentrated on matching the water front movement observed in 4D seismic data with simulation responses specific to individual injectors. This local history matching approach allowed for better alignment of seismic-derived saturation data with reservoir simulation models. Danaei et al. (2022) introduce the DAI-Proxy, a novel petro-elastic proxy model designed to substitute the traditional PEM in 4D seismic data assimilation. The DAI-Proxy simplifies the process by using a computationally efficient approach to relate time-lapse acoustic impedance to saturation and pressure changes, reducing the need for complex model extractions. The approach includes methods to account for model errors, ensuring data assimilation quality comparable to the PEM, and demonstrates that DAI-Proxy provides reliable performance with less computational demand, making it suitable for applications like permanent reservoir monitoring.

This study underscores the critical role of seismic forward modeling in both qualitative and quantitative applications of 4D seismic data. While qualitative approaches rely on amplitude changes to infer reservoir dynamics, quantitative methods integrate seismic data into reservoir models, refining history matching and enhancing prediction accuracy. It is worth noting that seismic history matching could be performed in the amplitude domain, although

impedance-based approaches are prevalent as they are easily estimated for each model in data assimilation.

In summary, while previous works have laid the foundation for 4D petro-elastic modeling and seismic forward modeling, this study differs in its scope, methodology, and focus. Specifically, it evaluates the performance of three forward modeling approaches (FMCOU, FMIOU, FMFI) in matching observed and simulated seismic data in a comparative analysis not present in previous studies.

4 METHODOLOGY

This chapter outlines the comprehensive approach undertaken to achieve the research objectives, focusing on time-lapse seismic forward modeling from simulation models. The methodology is designed to be detailed and reproducible, ensuring alignment with the research goals.

The methodology begins with acquired seismic data analysis, focusing on a detailed evaluation of the observed 4D seismic signals to evaluate data quality and reliability. Following this, a 1D feasibility study serves as a screening process to assess and interpret the strength of the 4D signals considering different production scenarios in the well scale. This initial screening is crucial for understanding the seismic responses and relating them to production changes considering hard data acquired in the field.

Following the feasibility study, Petro-elastic modeling (PEM) is employed to estimate the reservoir's elastic properties in a 3D context using simulation outputs. This involves calculating acoustic and shear impedances from reservoir specific conditions of porosity, pressure and fluid saturation. The outputs of this process are used in the scale transfer from the simulation domain to the seismic domain after applying the conversion from depth to time. These steps are fundamental to perform seismic forward modeling.

The 4D seismic forward modeling creates synthetic seismic from the estimated impedances. This can be performed, for example, by calculating reflectivity profiles from the estimated impedances and convolving them with a wavelet estimated from the observed seismic data. The resulting synthetic data is then compared with observed seismic data to validate the modeling approaches. During this process, noise was added to the synthetic data to mimic real world conditions followed by calibration to enhance misalignment between the observed and the synthetic seismic data. Important differences were found in this comparison, which led us to conclude, along with other analyses using production data, some misalignment of the simulation model. In a tentative to better represent the reservoir's dynamic behavior and improve alignment between synthetic and observed data, the simulation model properties were updated. These updates focused on critical parameters such as porosity, which directly influence the model's predicted impedance accuracy. In this sense, adjustments were manually made to the model´s porosity using multipliers. After each considered change in the porosity, the model

was simulated again and passed through the described workflow for the seismic data generation. More details on the described steps are given below.

4.1 Seismic Data Analysis

This step involves a thorough evaluation of the observed 4D seismic signal to ensure its quality and reliability and to improve reservoir understanding. The analysis is guided by the 4DS standards outlined by Stammeijer & Hatchell (2014) using the difference in the root mean square amplitude (dRMS) seismic attribute map. Furthermore, vertical sections of 4D seismic data, including amplitude and P-impedance, were analyzed to validate and complement the findings from the attribute maps. We also performed quality checks using normalized root mean square (NRMS) metric as defined in Kragh & Christie (2002). This includes assessing how the seismic signals change over time to ensure these changes are consistent with expected reservoir behavior.

4.2 1D Feasibility Study

The feasibility study assesses the strength of 4D seismic signals in reservoirs across various production scenarios, with a particular focus on changes in fluid saturations. This involves employing Gassmann's equation in log data from one well (1D) to predict how the seismic response of the rock is affected by changes in pore fluids. In more details, the fluid substitution exercise employed Gassmann's equations to simulate the effects of water and gas replacing oil, using key inputs such as oil saturation logs, water saturation logs, effective porosity (PHIE), and mineral properties.

4.3 Seismic Forward Modeling (FMCOU and FMIOU)

The seismic forward modeling process is depicted in Figure 4.1. It encompasses the traditional forward modeling approach here called FMCOU, which uses a constant value to define overburden and underburden, as well as FMIOU, the forward modeling that utilizes inversion results to define such intervals. This process was applied at two simulation time steps, considering both the base and monitor survey acquisition dates, using a plugin currently being developed for the Schlumberger Petrel 2021 software platform. The plugin is a specialized tool

designed to estimate elastic rock properties from direct reservoir simulation outputs and generate synthetic seismic amplitude volumes at various timesteps.

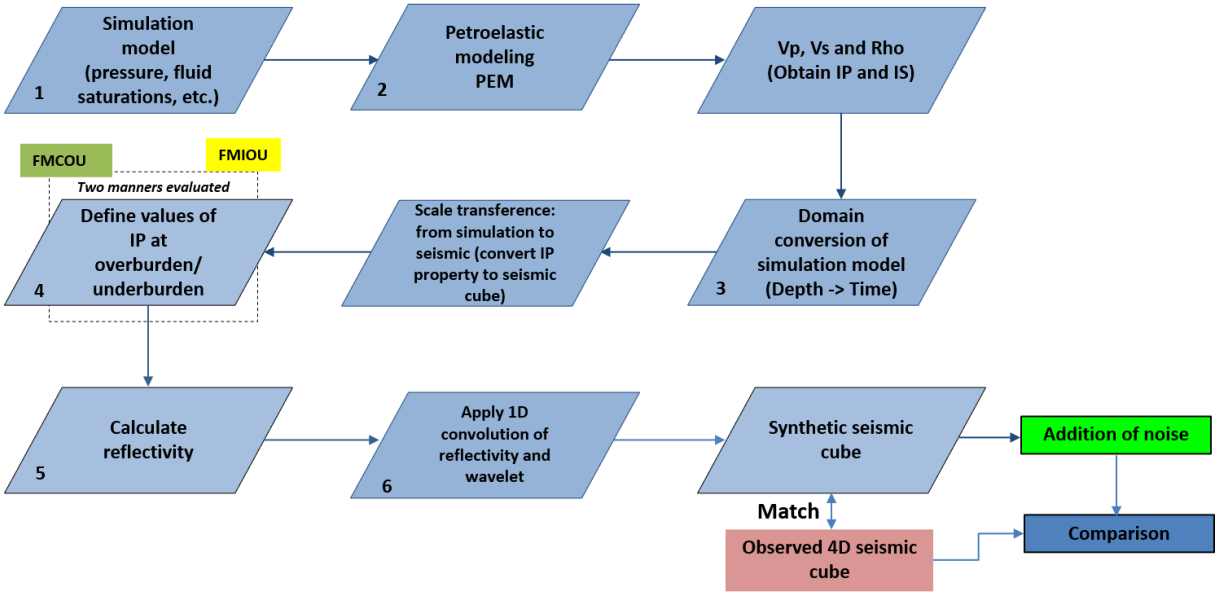

Figure 4.1: Seismic forward modeling workflow for the approaches FMCOU and FMIOU.

4.3.1 Running simulation model

The process begins by running a simulation model to extract both static and dynamic grid properties, including porosity, pressure, and fluids saturation, for the specified time steps corresponding to the acquired base and monitor seismic surveys.

4.3.2 Petro-elastic model calibration

The Petro-elastic model is then performed in the simulation grid. It is a set of equations that describes the link between reservoir rock and fluid properties and elastic properties. This phase involves the calculation of elastic parameters such as: P-wave velocity (Vp), S-wave velocity (Vs), density (Rho), P-wave impedance (Ip), and S-wave impedance (Is), through the utilization of reservoir outputs derived from the preceding phase.

4.3.3 Domain conversion

The velocity model is used to convert the simulation grid from depth to time domain. This conversion is needed because the 1D convolution must be performed in time. Besides,

converting the simulation grid into the time domain ensure it aligns with acquired seismic data, facilitating a more accurate comparison and integration of simulation and seismic data.

4.3.4 Scale transference

This step ensures scale transference by translating reservoir properties from a stratigraphic grid to a regular seismic grid, required for the seismic modeling, thus allowing for accurate integration and comparison of simulation results with seismic observations.

4.3.5 Non-reservoir and underburden/ overburden filling

This step focuses on defining the elastic attributes for the non-reservoir, i.e., overburden and underburden regions, to establish reliable reflections at the interfaces of the top and base of the reservoir. Understanding how overburden and underburden modeling influences the reflection response from the reservoir is vital, particularly in this study where the reservoir is thin and usually close to the vertical seismic resolution. Here we investigate different approaches. In the FMCOU scenario, a constant impedance value was used, which corresponds to the average shale impedance of the ABL reservoir, based on the impedance logs. This method is fast and computationally efficient, and does not require running a seismic inversion in the field. In the FMIOU case, the seismic inversion cube generated from the base seismic data was used to define these regions, which brings more robustness to the seismic modeling. This work is focused on the acoustic case, therefore only P-wave impedance (Ip) is considered.

4.3.6 Reflectivity calculations

Reflectivity was calculated from the estimated elastic attributes for each sample within the seismic volume. Specifically, we focus on normal incidence reflectivity, which pertains to the scenario where seismic waves are incident perpendicular to the interface between different geological layers. The normal incidence reflectivity equation is given by:

$$R = \frac{Z_2 - Z_1}{Z_2 + Z_1} \quad (4.1)$$

where Z_1 and Z_2 are the acoustic impedances of the two adjacent layers at each interface. These impedances are calculated as the product of density (ρ) and the seismic wave velocity (Vp) of each respective layer.

4.3.7 Convolution

This step, named 1D convolution, convolves the calculated reflectivity with a wavelet in a trace-by-trace manner. The wavelet can be statistically derived from the observed seismic data within the reservoir interval to ensure consistency between the synthetic and observed data. The outcome is a synthetic seismic cube of post-stack amplitudes, that is compared with the observed data to validate the model's accuracy and effectiveness.

4.4 Seismic Forward Modeling from Inversion (FMFI)

We introduce an approach to perform seismic forward modeling based on results from 3D seismic inversion differently from the FMIOU case. Figure 4.2 illustrates this approach, in which the PEM is run for both base and monitor, and the ΔIP (absolute difference) is calculated. The process begins with the utilization of the acoustic impedance cube derived from a previously 3D seismic inversion run on the base survey (Ip_base). Then, we calculate the impedances of the monitor seismic survey by summing the differences in impedance from the petro-elastic modeling (PEM) result to the inversion cube (Ip_mon = Ip_base + ΔIP_PEM). It is important to mention that for this methodology to be applied (i.e., the sum of the modeled absolute differences to inversion), one has to ensure accurate seismic inversion results, with a good mathcing with well log data. When this is not the case, adding the relative impedance differences from PEM would be more appropriate. This workflow enabled the subsequent calculation of reflectivity for the base and new monitor seismic surveys. The workflow's final stage involves convolving the reflectivity data with the same wavelet used in the traditional approaches, obtaining the synthetic amplitudes of two seismic cubes. These synthetic

amplitudes are then compared with the observed seismic amplitude data and to the other approaches (FMCOU and FMIOU).

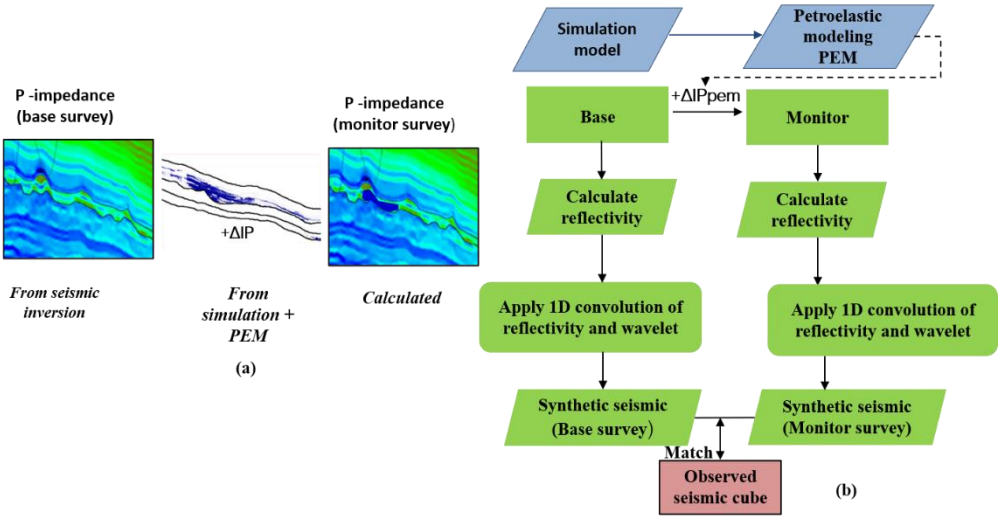

Figure 4.2: (a) Schematic showing the summation of the base seismic survey (from inversion) and the impedance differences derived from PEM used to calculate the monitor survey; b) workflow of FMFI.

4.5 Noise addition

In this study, noise was added to synthetic seismic amplitudes to simulate real-world seismic acquisition and processing conditions. Two distinct types of noise were introduced: random noise, which was added to the synthetic amplitudes of case FMCOU, and residual noise, added to the data of FMIOU and FMFI. For each seismic acquisition date, noise volumes were generated to simulate the noise associated with each vintage acquisition. Random noise was generated to mimic the frequency and visual characteristics of actual seismic data, considering a case where no inversion results are available. To refine the random noise and ensure its resemblance to real seismic attributes, a frequency filter and a structural smoothing filter were applied, as described in Rosa et al. (2024).

For the FMIOU and FMFI cases, residual noise volumes for each vintage were obtained by subtracting the observed amplitudes from the synthetic amplitudes generated through inversion. This approach reproduces the real effects of wave propagation happening in the field. The residual noise volumes are added directly to the synthetic data for the monitor and baseline surveys to enhance the simulation of real-world seismic acquisition conditions (Rosa et al., 2024).

To further adjust the noise levels, noise scaling was employed. The noise intensity calibration, in both cases (random and residual), was carried out using the normalized root mean

square (NRMS) metric. To calculate NRMS, RMS maps were generated for both the baseline and monitor amplitude data with added noise in a time window located above the reservoir. This region was chosen to minimize the influence of production changes and 4D seismic effects. In some cases, such as FMCOU, in which no reflection exists above the reservoir, two independent noise volumes were generated for the baseline survey, and the NRMS was computed over a wider time window encompassing the entire reservoir, still ensuring no 4D signals influenced the results. The calibration was performed by searching for the optimal scaling factor to be applied in the noise to guarantee a similar NRMS map of modeled amplitudes as the observation. After calibration, one of the noisy volumes was added to the synthetic amplitudes of the monitor survey, allowing for a more controlled evaluation of the effects of noise addition.

4.6 Comparison to the observation: 4DS amplitude and impedance dRMS attributes

In this study, dRMS attributes (Stammeijer & Hatchell (2014) were calculated in both the amplitude and impedance domains for both observed and synthetic data to facilitate their comparison and provide insights into reservoir dynamics.

4.6.1 Amplitude Domain

In the amplitude domain, maps of dRMS attribute are calculated in a specific reservoir interval for the observed and for the three seismic forward modeling approaches.

The observed 4DS map of amplitude differences between the baseline and monitor surveys for an acoustically soft reservoir is defined by:

$$dRMS_{amp\_obs} = RMS_{amp\_obs\_base} - RMS_{amp\_obs\_mon} \quad 4.2$$

where $RMS_{amp\_obs\_base}$ and $RMS_{amp\_obs\_mon}$ are the RMS amplitudes extracted from the observed baseline and monitor surveys, respectively, within the interval from top to base of the reservoir. The synthetic dRMS maps were calculated for each seismic forward modeling approach similarly as for the observed, being defined by:

$$dRMS_{amp\_syn} = RMS_{amp\_syn\_base} - RMS_{amp\_syn\_mon} \quad 4.3$$

where $RMS_{amp\_syn\_base}$ and $RMS_{amp\_syn\_mon}$ are the RMS amplitudes extracted from the modeled amplitudes of baseline and monitor respectively, within the same interval as the observed data.

4.6.2 Impedance Domain

In the impedance domain, maps of dRMS attribute were also calculated for the observed data (from inversion) and for the three modeled cases. These maps were compared to the ones from the amplitudes to evaluate the consistency and reliability of the seismic attribute. The observed 4D impedance differences between the monitor and baseline are defined by:

$$dRMS_{IP\_obs} = RMS_{IP\_obs\_mon} - RMS_{IP\_obs\_base} \quad 4.4$$

where $RMS_{IP\_obs\_mon}$ and $RMS_{IP\_obs\_base}$ are the RMS impedances for the monitor and baseline, respectively, extracted from the inversion impedance within the top and base of the reservoir. By explicitly calculating dRMS for both amplitude and impedance attributes, this study ensures consistency across multiple seismic parameters. This approach validates the reliability of both observed and synthetic data in capturing reservoir dynamics. Similarly, for the synthetic data, the modeled 4D impedance dRMS attribute is calculated as:

$$dRMS_{IP\_mod} = RMS_{IP\_mod\_mon} - RMS_{IP\_mod\_base} \quad 4.5$$

where $RMS_{IP\_mod\_mon}$ and $RMS_{IP\_mod\_base}$ are the RMS impedances for monitor and baseline, extracted from the synthetic modeled impedance of each modeling case within the same interval as the observed impedance maps.

4.7 Model adjustment

The model adjustment is a critical component in achieving a more accurate reservoir model. In the process of model adjustment, the objective is to improve the matching with observed data and its predictive capability over time. In this sense, several properties may be adjusted, such as porosity, permeability, aquifer properties, water-oil contact, fault transmissibility and relative permeability. Performing a proper data assimilation to update model's properties and improve data mismatch is out of scope of this study, therefore manual model adjustments were performed to try to improve general aspects, using the following steps:

- Initial Comparison: the process begins by comparing the initial modeled results with observed seismic and production data. It was observed that the seismic data did not match visually, and discrepancies were also noted in the BHP, Qo, GOR and Qw production data.

- Parameter Adjustment: based on the discrepancies, the model parameters are modified. In this case, only the porosity was adjusted through a multiplier applied uniformly across the reservoir.
- Simulation Re-run: With the updated model, new simulations were run to generate production and synthetic seismic data. The updated results were then compared with the observed data.
- Evaluation: The comparison assessed whether the adjustments improved the match between simulated and observed production data.

5 APPLICATION

The methodology was applied to the Albacora Leste field, using a real dataset provided by Repsol Sinopec. This chapter describes the ABL field and the data available for this work.

5.1 Location and tectonic settings

The study area is located in the Campos basin offshore Brazil. Figure 5.2 illustrates the location map of the field. The ABL field is notable for its extensive unconsolidated sandstone reservoirs, such as those identified as 'AB-140' and 'AB-210' (see Figure 5.1).

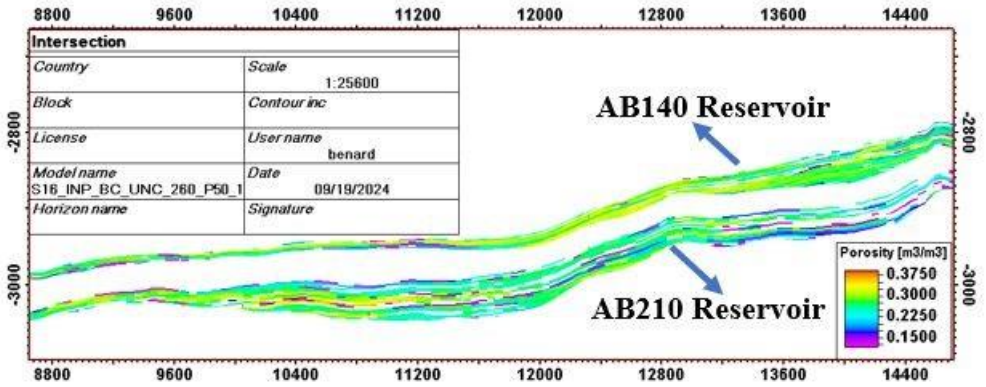

Figure 5.1: Vertical section of ABL upper and lower reservoir zones.

The field's complex geology, influenced by both high- and low-density turbidity currents, plays a significant role in its hydrocarbon trapping mechanisms, which are primarily stratigraphic with some structural contributions (Lemos et al., 2006). The Albacora Leste deepwater oilfield has reservoir depths ranging between 2300 and 2600 meters. The reservoirs are high-grade siliciclastic Miocene sandstones with an average porosity of 30%, an average absolute permeability of 3000 millidarcies, and oil with an API gravity range of 16.5 to 21.5 degrees.

The reservoirs in the field are influenced by structural features, including faults, which may act as conduits or barriers to fluid flow depending on their properties (Lemos et al., 2006).

The orientation and position of these geological features also influence the distribution of hydrocarbons within the reservoir, as well as production performance. For instance, a well placed near a fault with good connectivity to the reservoir may yield higher production rates,

while wells near sealing faults may experience pressure compartmentalization, requiring targeted reservoir management strategies (Lemos et al., 2006).

These structural complexities, combined with the high porosity (30%) and permeability (3000 md) of the siliciclastic sandstones, make the Albacora Leste Field a challenging yet highly productive hydrocarbon reservoir (Bybee, 2006). The interplay between geological features and reservoir properties underscores the importance of detailed reservoir characterization and model's accuracy analysis to optimize production. This reservoir complexity also highlights the need for integrating seismic interpretation and modelling techniques to simulation models to address the dynamic behaviour of such reservoirs effectively.

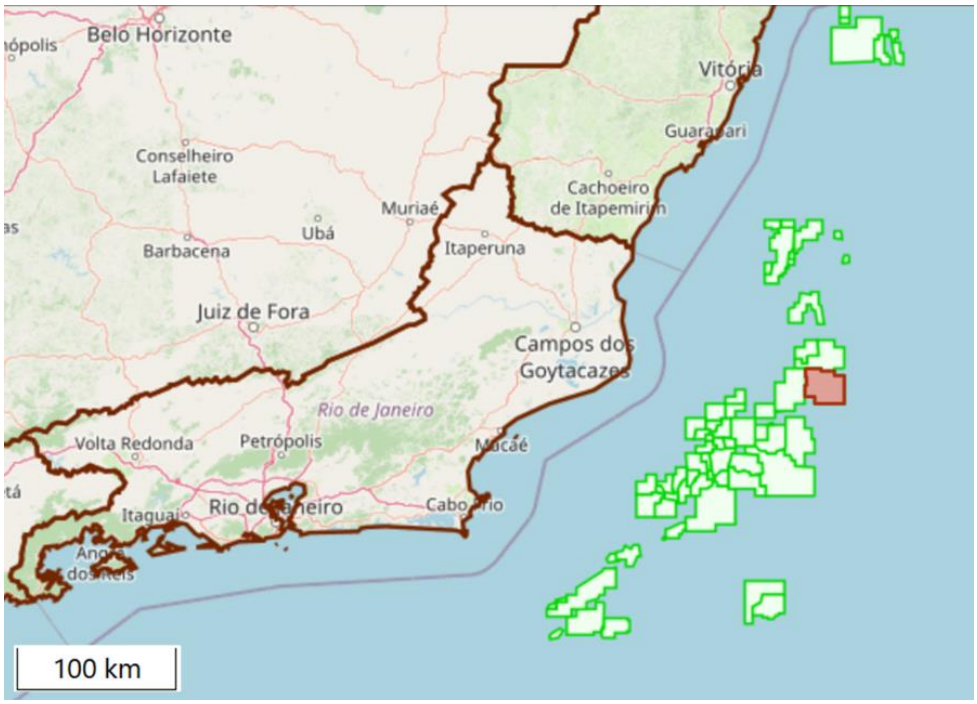

Figure 5.2: Location map of ABL field (red rectangle offshore) – from ANP website.

5.2 Field development strategy

The Albacora Leste field was discovered in 1986 by Petrobras, which initially formed a consortium with Repsol, holding a 90% working interest while Repsol held 10%. In 2010, Petrobras divested a 60% stake in the field to Repsol Sinopec Brasil, transferring operatorship as part of its strategic portfolio management. This transition allowed Repsol Sinopec to expand its offshore presence in Brazil while implementing advanced reservoir management strategies and technologies. Despite the change in operatorship, Petrobras retained a 30% minority stake, ensuring strategic involvement in the field's ongoing development. In April 2022, Petrobras announced the sale of its remaining 90% stake in Albacora Leste to PRIO

(formerly PetroRio), a subsidiary of PRIO S.A., for up to $2.2 billion. With the completion of the transaction, PRIO became the operator, holding 90%, while Repsol Sinopec Brasil retained its 10% interest. The partnership in Albacora Leste has played a crucial role in enhancing production efficiency and integrating innovative reservoir monitoring and management solutions. The development strategy for the Albacora Leste field focuses on optimizing oil recovery through the implementation of high-productivity wells, effective water injection, and advanced well completion techniques (Bybee, 2006). The primary target of this study is the AB140 zone, characterized by Miocene sandstones with high porosity and permeability. The development plan includes 12 horizontal producer wells and 9 strategically placed horizontal injector wells to provide pressure support (Figure 5.3). These injector wells are crucial, especially given the absence of significant natural aquifer influx, for maintaining reservoir pressure in the AB140 reservoir.

At the onset of production, the reservoir pressure was measured at approximately 25 MPa, which is close to the bubble point. Maintaining this pressure is essential to keeping the oil in a single phase and preventing gas breakout, which would negatively affect oil recovery efficiency.

Reservoir simulation results provide estimates of the Original Oil in Place (OOIP) and initial hydrocarbon volumes, which are fundamental to the field development strategy. The OOIP is estimated at 807,669,428 sm^3, while the Original Water in Place (OWIP) and Original Gas in Place (OGIP) are 1,328,437,798 sm^3 and 59,701,617,315 sm^3, respectively. These values, derived from simulation outputs, form the basis for implementing water injection as the primary pressure maintenance mechanism. Production from the Albacora Leste field commenced in March 2006, as confirmed by cumulative production data. The early production phase was characterized by stable oil production, with minimal water production and controlled gas production. The gradual increase in oil recovery, alongside steady pressure support from water injection, confirms the effectiveness of the field development strategy.

Figure 5.4 presents the cumulative production and injection performance over time, illustrating trends in cumulative oil (green), gas (red), and water production (blue), along with cumulative water injection (light blue). The production trends indicate that continuous water injection has effectively maintained reservoir pressure, with no major fluctuations, confirming stable injection performance. Oil production initially increased steadily but began plateauing after 2010, indicating the effects of reservoir depletion. However, water injection helped slow the decline and sustain oil recovery. Gas production trends suggest that gas liberation occurs mainly from solution, with no significant gas breakthrough observed. The controlled increase

in cumulative gas production aligns with effective reservoir depletion management. Water production remained low initially but gradually increased over time, indicating delayed water breakthrough and confirming an efficient waterflooding strategy.

A comprehensive analysis of well performance over time has been conducted to assess reservoir management effectiveness, as illustrated in Figure 5.5. This heatmap provides an overview of daily oil production and bottom hole pressure (BHP) variations across the producer and injector wells. The top section of the heatmap visualizes the daily oil production (in bbl/day) and BHP (in bar) for producer wells, highlighting production trends and pressure fluctuations over time. The bottom section represents BHP changes in injector wells, demonstrating the role of water injection in maintaining reservoir pressure. The color intensity in the heatmap reflects production and pressure magnitudes, allowing for better visualization of well behavior and performance over time.

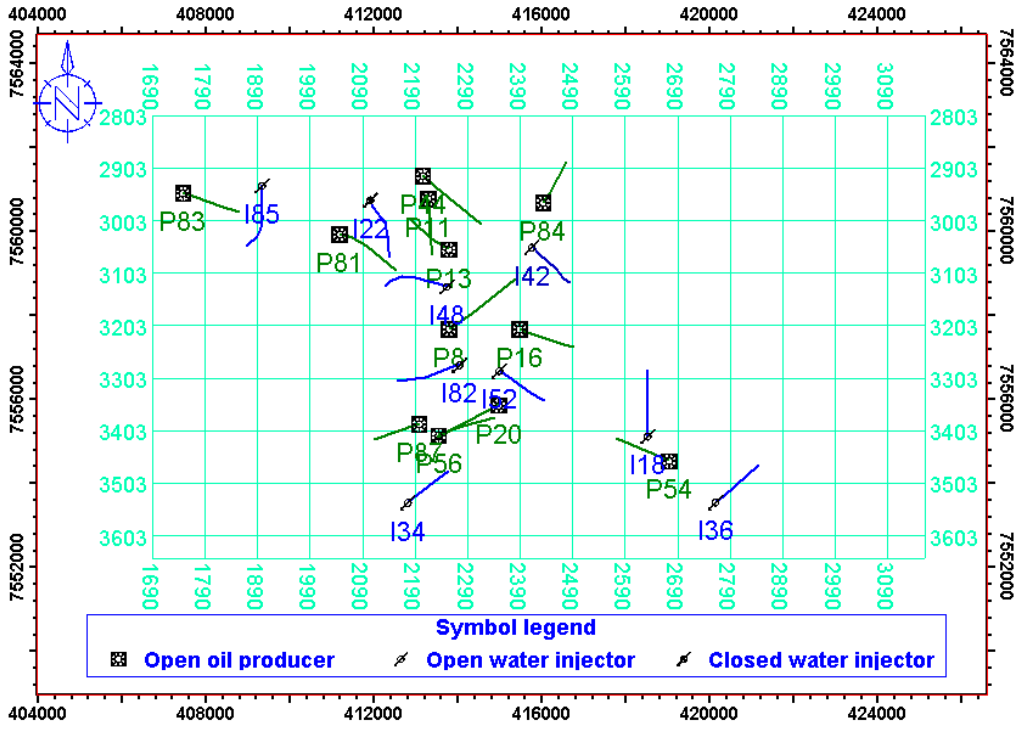

Figure 5.3: Base map with seismic lines and well locations. Water injection wells are denoted by blue and production wells by green.

Additionally, 4D seismic surveys are utilized in ABL to evaluate pressure and saturation changes over time, supporting dynamic reservoir monitoring and field management (Lemos et al., 2006). This is possible due to the soft nature of these reservoir (i.e., high bulk modulus), making them very sensible to reservoir condition changes and good candidates for 4D studies. The integration of time-lapse seismic data and well performance analysis enables the identification of reservoir depletion zones, improving sweep efficiency and guiding future development strategies.

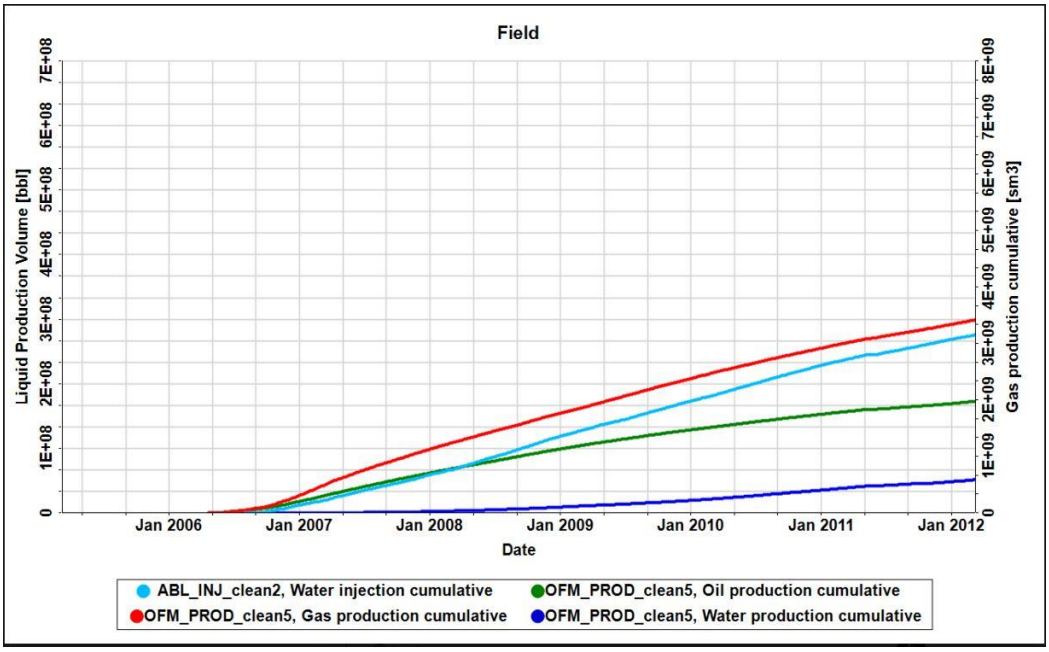

Figure 5.4: Cumulative production and injection trends for the ABL field (March 2006 -2012).

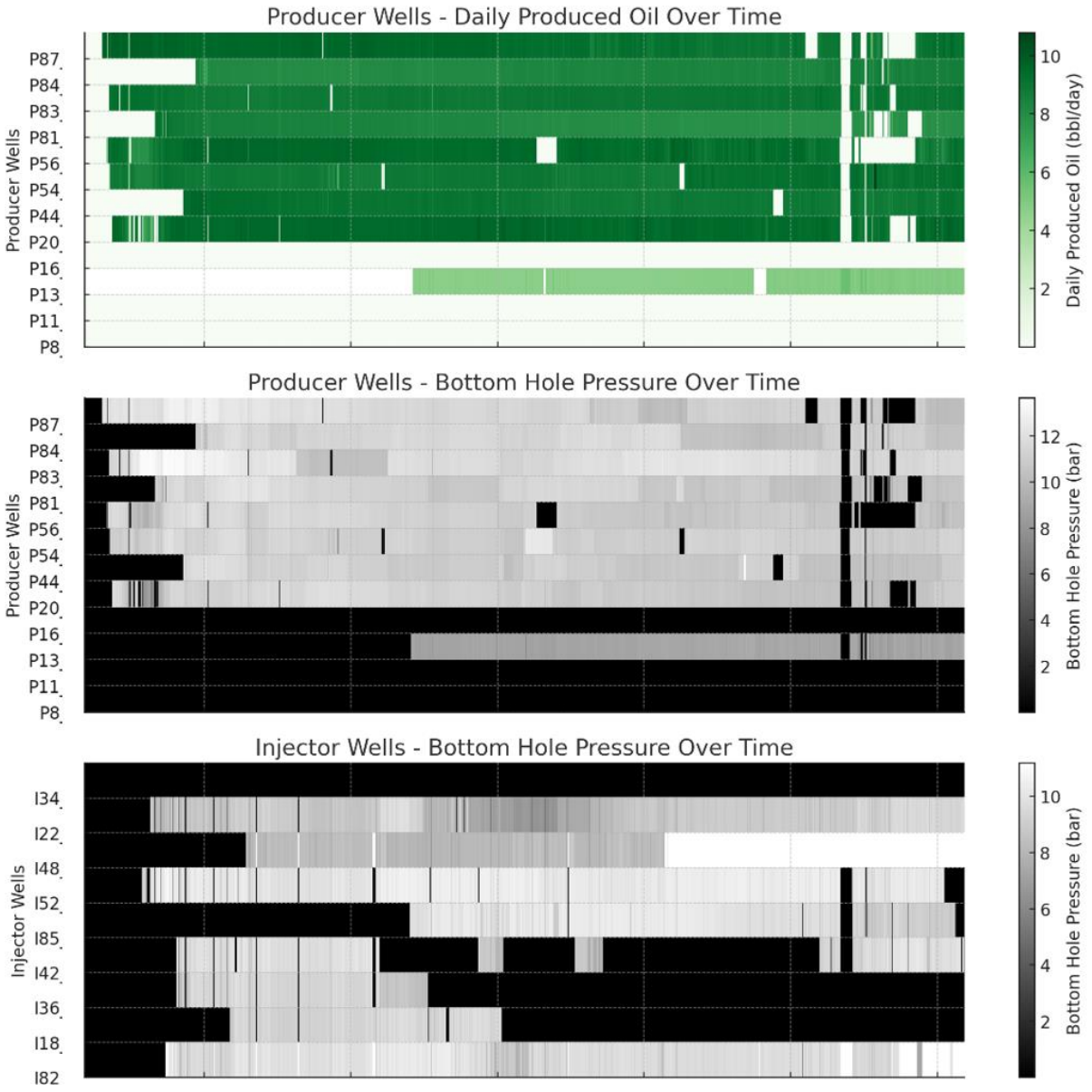

Figure 5.5: Heatmap of well performance over time daily oil production and bottom hole pressure for producer and injector wells.

5.3 Data Availability

The dataset utilized in this study comprises data collected during various stages of exploration, appraisal, and production. It includes 3D seismic data such as post-stack amplitude cubes in SEG-Y format, as well as acoustic inversion cubes, amplitude residual datasets and petro-elastic model templates for the different facies developed by Dillon et al. (2023). A statistically extracted wavelet was also provided. Reservoir structural information was available, including well tops and reservoir top/base horizons in time, along with a preliminary velocity model for depth conversion. A facies model provided the lithology

distribution. Simulation model in Eclipse 100 format, with production and injection history were also available.

The well history included bottom-hole and wellhead pressures, oil rates for producers, and water rates for injectors. Additionally, well logs such as p-wave velocity (Vp), s-wave velocity (Vs), density (RHOB), volume of shale (VCL), and effective porosity (PHIE) were accessible, being employed for fluid substitution analysis. Effective porosity (PHIE) was applied to correct for shale content, ensuring the appropriate application of Gassmann's theory. Two scenarios were modeled after initial conditions: in the first, 100% water saturation was assumed, meaning water replacing oil. This simplified scenario, which does not account for residual oil, allowed focus on the broader impact of fluid substitution on seismic response. In the second scenario, oil was replaced by a mixture of 60% gas, 20% oil, and 20% water, representing a gas-replacing-oil condition with residual oil and water. This integrated dataset formed the foundation for analyzing the seismic forward modeling, facilitating detailed evaluations of seismic responses derived from reservoir simulation models.

5.3.1 Seismic domain and elastic attributes

The seismic dataset used in this study includes streamer acquisition data featuring a baseline survey from 2005 and a monitor survey from 2012, which are fundamental for the seismic analysis and time-lapse evaluation performed in this study.

Earlier seismic acquisitions in the Albacora Leste field, including the initial 3D seismic survey from 1987 and a subsequent survey in 2001, contributed to the field's reservoir characterization but had notable limitations. The 1987 data suffered from inadequate acquisition parameters and suboptimal processing routines, which limited its effectiveness for detailed reservoir characterization. The 2001 survey improved seismic resolution, enhancing the definition of reservoir boundaries, sandstone channels, and erosive features. However, despite these advancements, challenges remained in identifying features such as small gas caps and thin interlaminated rock sequences due to resolution constraints (Lemos et al. 2006).

Figure 5.7 shows the Normalized root mean square (NRMS) map of the observed seismic data, considering the surveys of 2005 and 2012. The mean NRMS value over the studied region was 27% indicating low repeatability. However, problematic regions with higher NRMS values exceeding 30% (red regions on the map) were observed, suggesting significant noise or inconsistencies. These high-NRMS areas are critical for further evaluation, as they

could impact the reliability of the seismic interpretation and require additional data processing to improve repeatability.

Besides post-stack amplitude data, it was also provided acoustic inversion cubes for both vintages. These inversion cubes were generated using model based inversion within the Jason suite software and were obtained by Dillon et al. (2023) along with the corresponding residual noise data (i.e., the difference between the observed and the synthetic amplitudes from inversion). Additionally, a facies volume was provided, which is instrumental in the petro-elastic modeling (PEM) application.

The Petro-elastic modeling (PEM) in this study was performed using the plugin developed under the RESSIM-FORM.CO2 project, which is integrated into the Schlumberger Petrel 2021 software platform. This plugin is a specialized tool designed to estimate elastic rock properties from reservoir simulation outputs and generate synthetic seismic amplitude volumes across different timesteps.

The mineral elastic moduli were calculated using the Voigt-Reuss-Hill average to provide an effective approximation of the bulk and shear moduli, considering the different rock minerals. Fluid properties were determined using the empirical relationships proposed by Batzle & Wang (1992) to define the bulk modulus ensuring accurate representation of oil, gas, and water properties within the PEM. To enhance the accuracy of fluid saturation effects on the elastic properties, the Patchy saturation model was applied, accounting for the heterogeneous distribution of fluids within the pore spaces. Reservoir-specific parameters, such as pore pressure and overburden pressure, were incorporated into the PEM, adjusted using Biot's coefficient. These adjustments ensured that stress changes caused by fluid extraction or injection were accurately captured and translated into the rock matrix's elastic response.

The extended unconsolidated sand model described in Allo (2019) was utilized to estimate the dry rock's elastic properties, considering factors such as porosity, grain size, grain shape, mineralogy, and critical porosity. Eventually, our approach incorporates Gassmann's theory for estimating the saturated rock elastic properties under two scenarios, corresponding to the timesteps of the baseline and the monitor.

The PEM incorporated rock-physics templates characterized by four facies: shale, shaly-sand, intercalated sand, and sand. These templates captured variations in elastic properties considering reservoir-specific scenarios of clay volume, porosity and fluid saturations. The facies were also characterized based on their cohesion, friction coefficients, and other key parameters. The mechanical behavior of these facies is influenced by coordination number (C), critical porosity (ϕC), friction coefficient (FC), grain angularity (RR), and matrix stiffness index

(MSI). The coordination number (6–15) governs grain contacts and rock stiffness, while ϕC (0.36–0.40) separates suspension supported and load bearing grains. The friction coefficient (0–1) controls grain-to-grain adhesion, and the grain angularity (RR) affects compaction, with irregular grains (RR < 1) packing differently from spherical grains (RR = 1) or mixed-size grains (RR > 1). MSI regulates rock stiffness, transitioning from soft (MSI = 0, Reuss bound) to intermediate (MSI = 0.5, Hill bound) and stiff (MSI = 1, Voigt bound) sandstones. These parameters define facies dependent variations in rock stiffness and elastic properties.

The characteristics of the facies used in the study are summarized in Table 1, which highlights the mechanical and petrophysical differences among them. The table demonstrates how variations in these properties influence reservoir quality, ranging from poor-quality shaly facies to high-quality sand facies. The elastic properties of the facies, such as bulk modulus, shear modulus, and density, are detailed in Table 2. The "mixture" values represent composite elastic properties derived from the volumetric fractions of the facies' constituents (except clay).In contrast, the clay properties reflect the elastic characteristics of pure shale.

Table 1: Facies characteristics.

Facies	Shale volume	Cohesion	Friction coefficient	Critical porosity	Reservoir quality
Shale	0.72	10	1	0.40	Poor quality due to high clay content
Shaly sand	0.21	6	0.8	0.40	Reduced mechanical strength
Intercalated sand	0.29	6	1	0.40	Moderate reservoir quality
Sand	0.12	12	1	0.40	Good quality with highest cohesion value

Table 2: Elastic properties of facies.

Facies	Bulk Modulus (K)	Shear Modulus (G)	Density (ρ)
Shale	22 GPa (clay), 35 GPa (mixture)	7 GPa (clay), 37 GPa (mixture)	2.6 g/cm³ (clay), 2.64 g/cm³ (mixture)
Shaly sand	22 GPa (clay), 35 GPa (mixture)	7 GPa (clay), 37 GPa (mixture)	2.6 g/cm³ (clay), 2.64 g/cm³ (mixture)
Intercalated sand	22 GPa (clay), 35 GPa (mixture)	7 GPa (clay), 37 GPa (mixture)	2.6 g/cm³ (clay), 2.64 g/cm³ (mixture)
Sand	22 GPa (clay), 35 GPa (mixture)	7 GPa (clay), 37 GPa (mixture)	2.6 g/cm³ (clay), 2.64 g/cm³ (mixture)

After running PEM, the estimated P-impedances were converted from depth to the time domain using a velocity model, and transferred to the seismic scale using the same resolution grid as of the observed seismic data.

To define the overburden and underburden for the FMCOU case, an impedance value of 6462.5 (g/cm³) * (m/s) was assigned, corresponding to the ABL-140 shale impedance value. In contrast, the acoustic inversion results from the baseline survey were utilized to define the overburden and underburden for the FMIOU and FMFI cases.

Furthermore, a wavelet statistically extracted from the baseline survey's full-stack seismic data was utilized for seismic forward modeling. This wavelet is the identical to the one used in the seismic inversion process. Vertical sections depicting 3D seismic amplitude and P-impedance for baseline are shown in Figure 5.6.

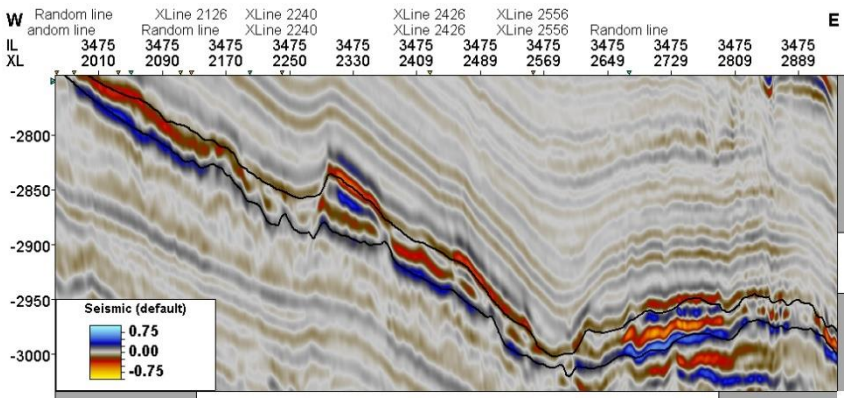

(a)

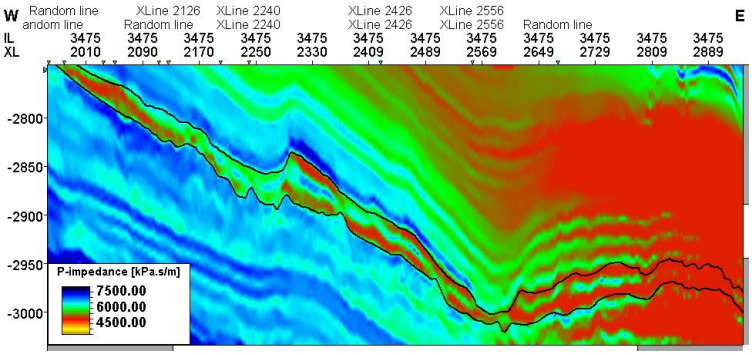

(b)

Figure 5.6: Observed 3D seismic data for the baseline survey: (a) seismic amplitude and (b) inverted acoustic impedance.

For FMIOU and FMFI, residual noise was calculated by subtracting observed amplitudes from synthetic amplitudes obtained from inversion. Synthetic amplitude data for both baseline and monitor surveys served as inputs. Random noise was generated using spectrally shaped noise, with an RMS signal of 0.15, an RMS noise of 0.063, and signal to noise ratio (S/N) ratio of 14.9 dB. The noise was refined using a frequency filter with a cosine taper, applying a high-pass cutoff of 60 Hz and a high-frequency cutoff of 80 Hz. To ensure spatial consistency, structural smoothing was applied with parameters Sigma X = 10.0, Sigma Y = 5.0, and Sigma Z = 0.0. Noise scaling was employed to adjust the noise levels, with scaling factors of 3 for FMIOU and FMFI cases and 12 for random noise, reflecting the S/N ratios observed in actual seismic data.

The scaling factors were determined based on the mean NRMS values derived from the observe data. This detailed approach ensures reproducibility and enhances the reliability of the results by accurately modeling and evaluating noise characteristics.

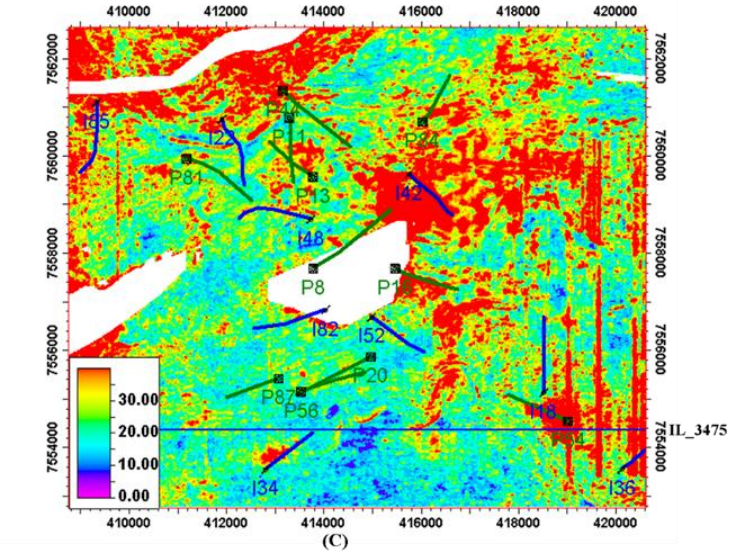

Figure 5.7: Normalized root mean square (NRMS) map of the observed seismic data.

The seismic data analyzed so far are indexed in the time domain. An essential component of the dataset is the velocity model, which is crucial for accurately converting the simulation grid from depth to time-domain. Since the velocity model was not provided, we used a preliminary model for the domain conversion. This can bring challenges in the evaluation of the different seismic modeling approaches since vertical misalignments between modeled and observed may occur, which need to be taken into consideration. Figure 5.8 compares the seismic horizons for the ABL-140 reservoir, derived from both seismic interpretation (black) and the simulation grid (red). The black curves represent the top and base horizons from seismic

interpretation, while the red curve shows the corresponding horizons from the simulation model after time conversion. Despite the tops being aligned, a misalignment between the seismic and simulation base horizons is observed, being attributed to uncertainties in the velocity data, underscoring the need for careful comparison between modeled and observed data.

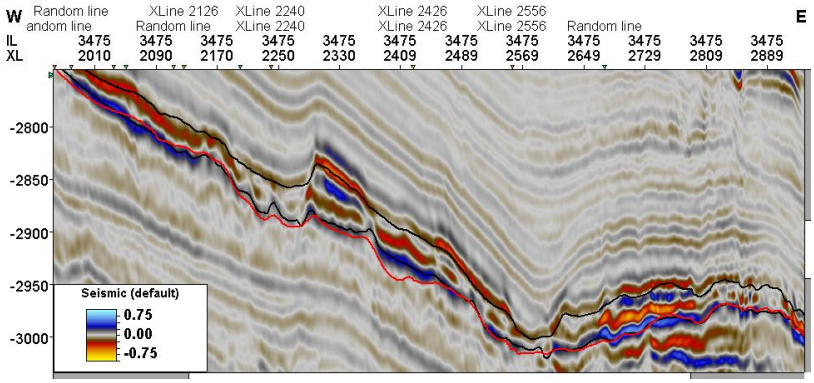

Figure 5.8: Comparison of seismic horizons derived from both seismic interpretation (black) and simulation grid (red) in the ABL-140 reservoir.

5.3.2 Simulation model

The provided simulation model comprises 10.360.391 grid cells organized into a 337 x 433 x 71 block configuration. Each cell measures 50 meters in the x and y directions and has an average thickness of 4 meters. Simulations were built using the Eclipse (E100) black-oil numerical reservoir simulator and incorporate production data from 2006 to 2012. This simulation model was used to generate the synthetic seismic data, which are compared against observed seismic data to verify the model's accuracy. Figure 5.9 shows the 3D view of the base

simulation model and well locations. The image highlights channel systems and regions of inactive cells, as indicated by red arrows.

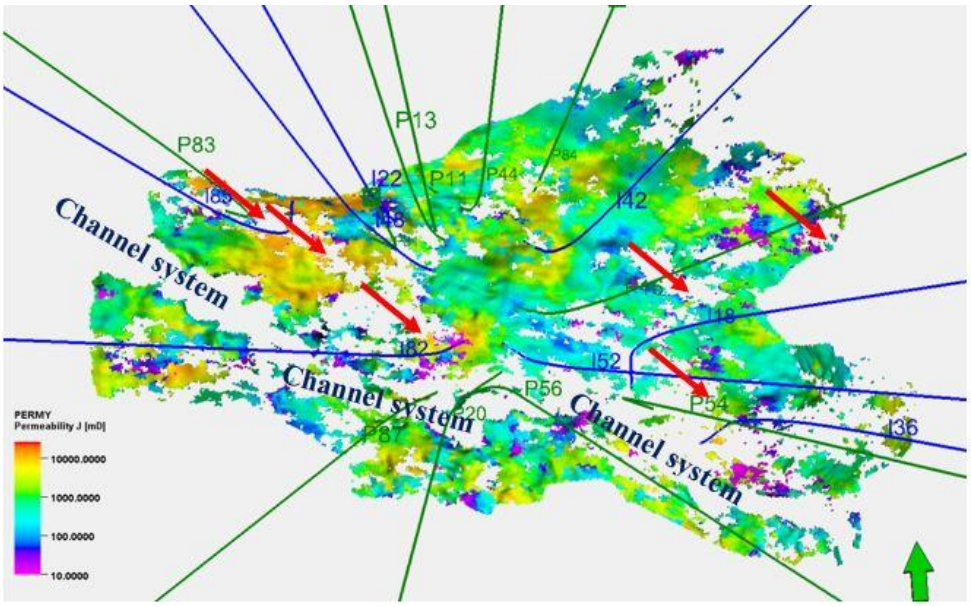

Figure 5.9: 3D view of the base simulation model showing permeability distribution (in the y-direction) and well locations (oil producers in green and water injectors in blue). The red arrows indicate channel systems and regions of inactive cell

6 RESULTS AND DISCUSSION

This chapter outlines the results derived from the proposed workflow applied to the study area.

6.1 1D feasibility study

To better understand the impact of fluid substitution on seismic properties, we conducted an analysis using Gassmann's equations across different fluid scenarios in ABL-2 well. This approach allowed us to examine changes in density (RHOB) and P-wave velocity (VP) under varying saturation conditions. The findings from these analyses are detailed below. Figure 6.1 displays the log values post-fluid substitution, with blue curve representing the water case, the red curve for the gas case, and green for the initial case based on the in-situ saturations (before the fluid substitution). From the analysis we noticed an increase in density (RHOB log) and P-velocity (VP), with an average of 7% impedance increase when oil is totally replaced with water, and an average decrease of 8% in the P-impedance when oil was replaced by 60% gas, 20% oil and 20% water. There were identified zones with high shale content at depths of 2533 m, 2540 m, 2548 m, and 2554–2558 m.

Since Gassmann's equations assume homogeneous and isotropic reservoirs and are more suited to clean sandstones, they tend to be less reliable in shale-rich zones, leading to inaccurate impedance predictions. To address this limitation, we applied a porosity cutoff (PHIE $\leq$ 0.10) \to exclude these shale-rich zones from the fluid substitution results. In these zones, we utilized the in-situ Vp, Vs, and RHOB logs, ensuring that no impedance changes occur.

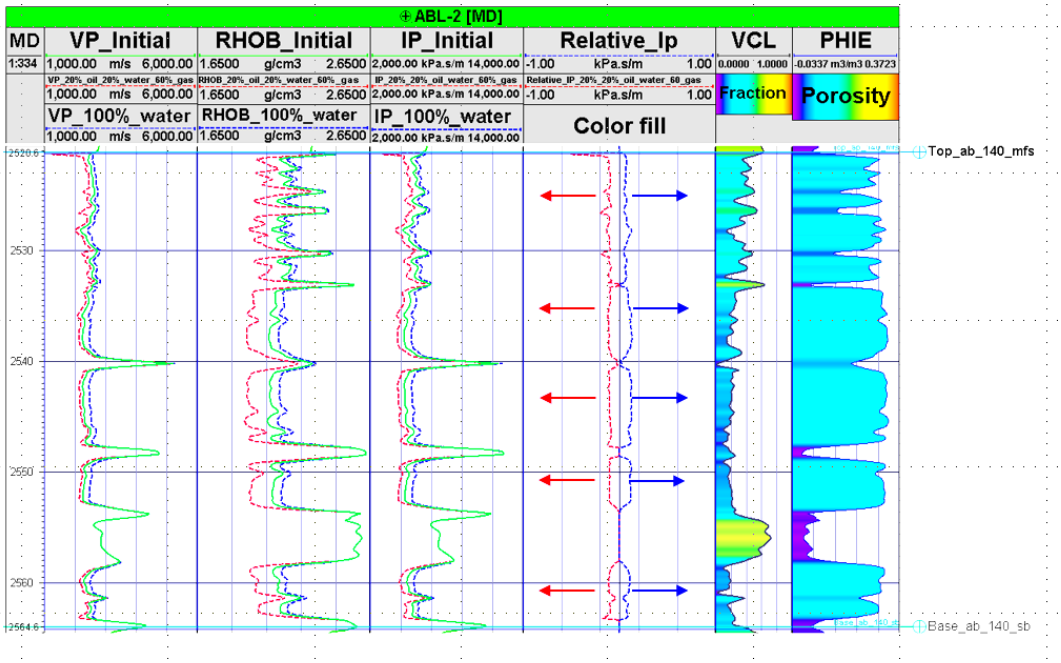

Figure 6.1: Fluid substitution exercise for ABL-2 well. Green curves: initial Vp, Vs, RHOB and IP. Red curves: Vp, Vs, RHOB and IP for gas increasing scenario. Blue curves: Vp, Vs, RHOB and IP for water increasing scenario. The relative impedance curves are also shown for both cases, including the volume of shale (VCL) and effective porosity (PHIE).

6.1.1 Petro-elastic model

The assessment of the PEM results derived from simulation models is essential for understanding how the elastic properties of the reservoir respond to changes in production conditions. This study focuses on analyzing the P-impedance values obtained for the years 2006 and 2012, more specifically by examining the relationship between their changes and the variations in fluid saturation and pressure. These changes are characterized by softening or hardening effects. The softening effect is indicated by a decrease in impedance, primarily resulting from an increase in reservoir pore pressure. The impedance variations are shown alongside the respective changes in pressure, gas saturation, and water saturation between 2006 and 2012. In the ΔIP map, areas marked in light green represent a 2% relative decrease in impedance, which correlates with an increase in pressure as indicated by the red arrows (Figure 6.2a and b).

In contrast, the hardening effect is characterized by an increase in impedance associated with rising water saturation. This is reflected in the purple regions on the ΔIP map, which show an approximate 6% relative increase in impedance, as denoted by the blue arrows (Figure 6.2a and d). It is important to note that the ΔSg map (Figure 6.2c) shows no significant

changes in gas saturation during this period, emphasizing that pressure and water saturation were the primary drivers of impedance variations.

The percentage changes in IP observed in the 1D analysis were consistent with the observations from the 3D models, confirming the reliability of PEM results.

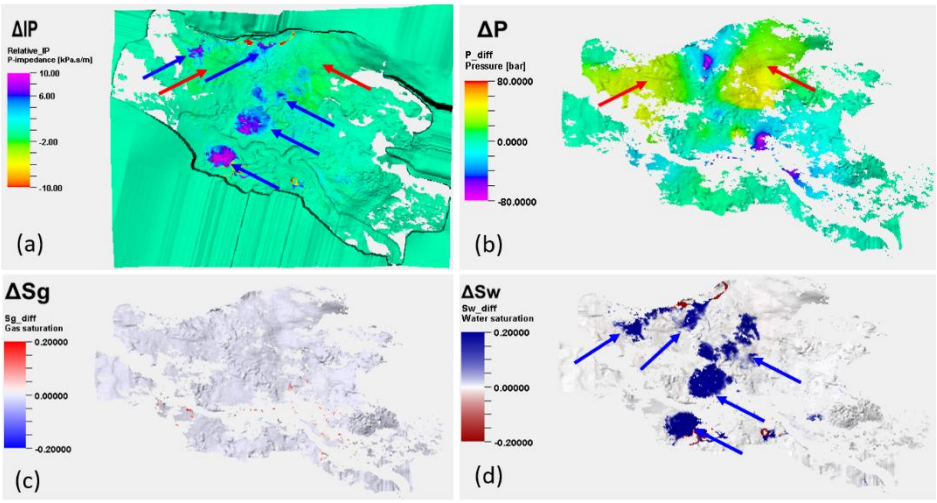

Figure 6.2: (a) Relative P-impedance difference map, (b) pressure difference map, (c) gas saturation difference map, (d) water saturation difference map. The map corresponds to layer 9 of simulation model, located in the AB140 reservoir zone. The blue arrows represent zones of increasing water saturation, corresponding to a hardening anomaly, while the red arrows indicate a pore pressure increase, which corresponds to a softening anomaly.

6.2 3D Impedance comparative analysis

This section assesses the consistency of various overburden/underburden modeling approaches by comparing the 3D impedance results with observed data (represented by acoustic inversion outcomes). Within the reservoir zone, the impedance values are generally low and exhibit a range of magnitudes characteristic of unconsolidated sandstone formations. These formations typically exhibit low acoustic impedance due to their high porosity and the presence of loose, poorly cemented grains.

Figure 6.3 illustrates the comparison of the 3D impedance sections between the modeled results and the observed data from the baseline survey. The observed data and the FMFI result (Figure 6.3a and c) correspond to the same dataset. Discrepancies arise when comparing these to FMCOU and FMIOU (Figure 6.3b and d), particularly in the upper section of the reservoir (dashed black ellipses), in which FMCOU and FMIOU exhibit significantly lower impedance values compared to FMFI, suggesting model inconsistency. Conversely, in the lower part of the reservoir (highlighted by the white ellipses), the observed data has a stronger softening than the FMCOU and FMIOU data. Around XL 2330, the observed data and FMFI reveal a high

impedance value whereas FMCOU displays a contrasting low impedance value, highlighted by the yellow dashed circles. The black continuous horizons denote the upper and lower boundaries of the AB140 reservoir.

Figure 6.4 illustrates the 3D impedances in a different section of the AB140 reservoir, where notable discrepancies between the modeled results and the observed data are also evident. Figure 6.4b and d emphasize the presence of null blocks in the simulation model, indicated by the red arrows, in which no flow occurs and therefore no PEM results are available.

Additionally, in the lower part of the reservoir (denoted by the black dashed ellipses), the observed data (Figure 6.4a and c) show significantly lower impedance (IP) values compared to the modeled results from FMCOU and FMIOU (Figure 6.4b and d).

This underestimation in the models may be related to inaccuracies in porosity and permeability or fluid and pressure distribution assumptions.

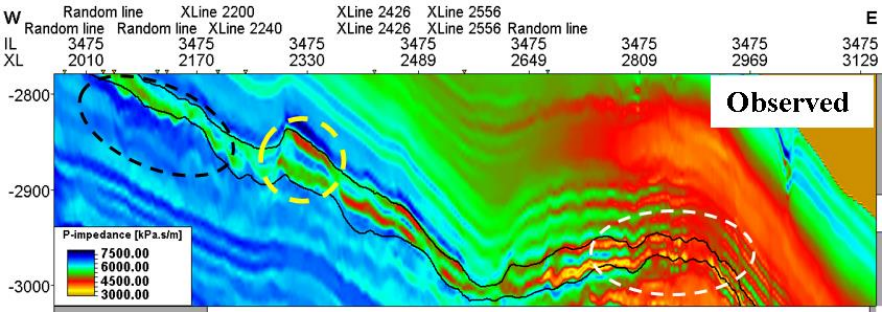

(a)

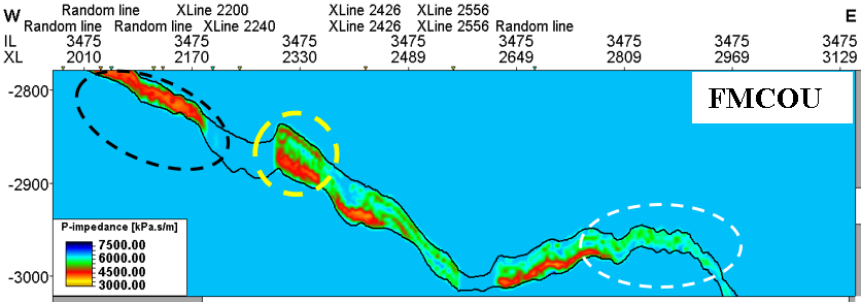

(b)

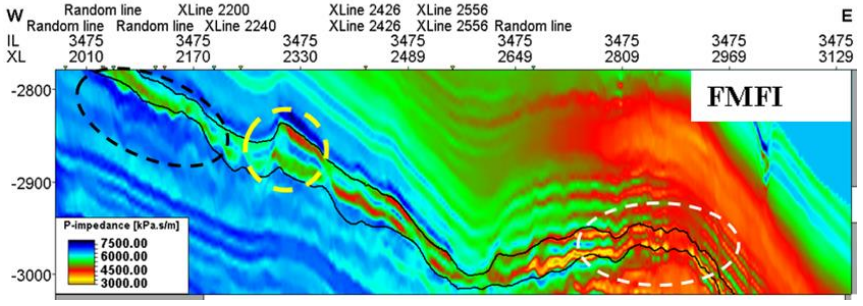

(c)

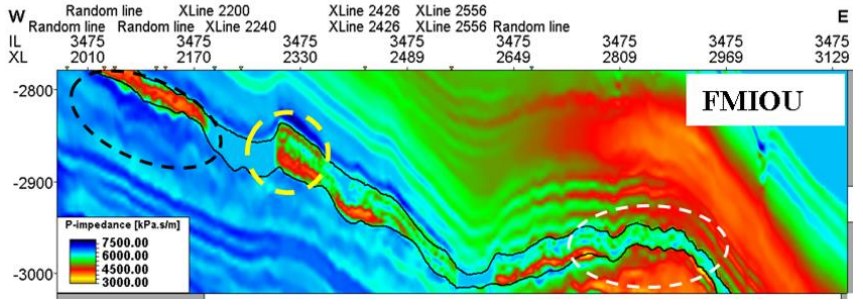

(d)

Figure 6.3: Vertical sections of 3D P-impedance of a) observed data (inversion); b) FMCOU; c) FMFI; d) FMIOU approaches. The dashed black ellipses highlight areas of lower impedance in FMCOU and FMIOU compared to FMFI. The white ellipses indicate regions with lower impedance in the observed data compared to FMCOU and FMIOU. The yellow dashed circles mark a high impedance region in the observed data and FMFI, contrasting with the low impedance in FMCOU.

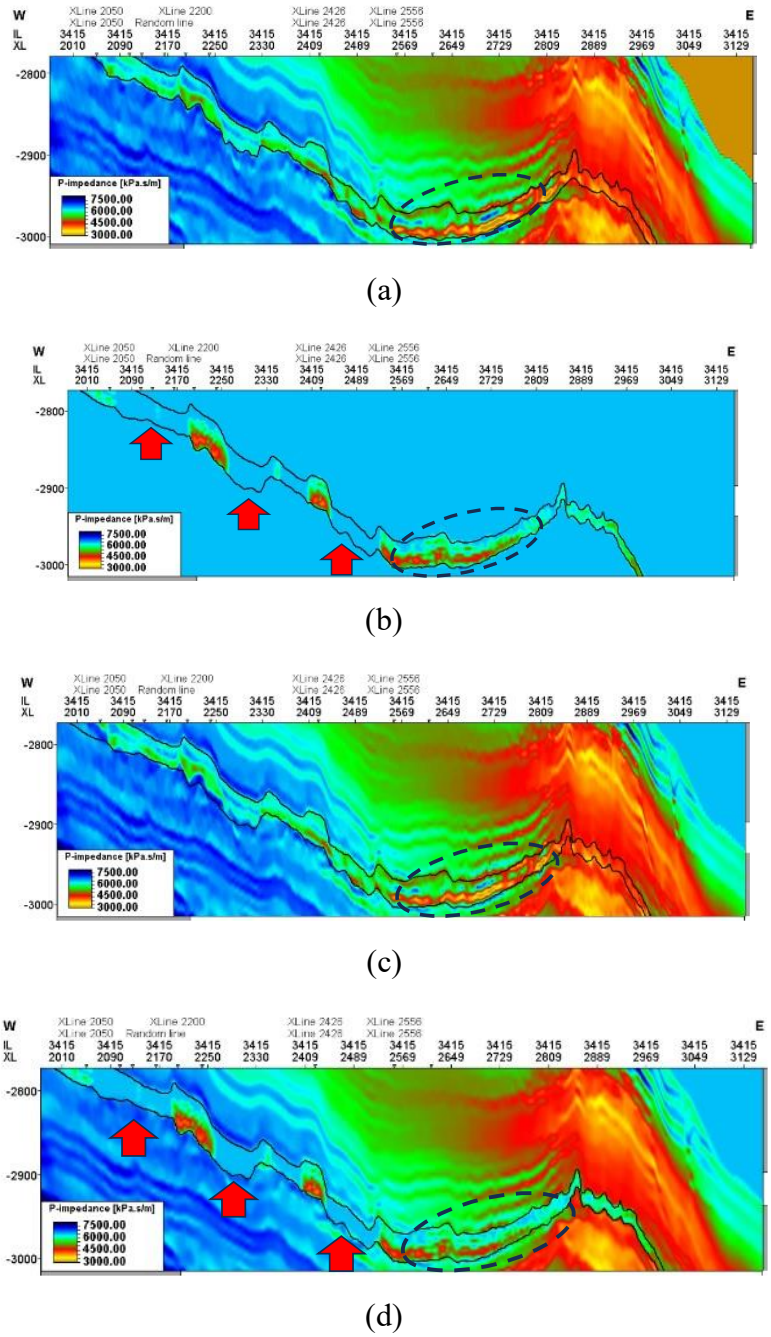

Figure 6.4: Vertical sections of 3D P-impedance of a) observed data (inversion); b) FMCOU; c) FMFI; d) FMIOU approaches. The red arrows indicate null blocks in the simulation model where no flow occurs, resulting in no PEM results. The black dashed ellipses highlight areas with significantly lower impedance values in the observed data compared to the modeled results from FMCOU and FMIOU.

6.3 Seismic forward modeling

6.3.1 3D amplitude comparative analysis

This section examines the results of applying the sim2seis methodology through three distinct approaches: FMCOU, FMIOU, and FMFI.

Figure 6.5 illustrates the synthetic 3D seismic amplitude of baseline survey without noise and the observed data. The black continuous horizons denote the upper and lower boundaries of the AB140 reservoir. FMFI shows a good correlation with the observed amplitude (Figure 6.5a and c), indicating the accuracy of inversion results. Within the reservoir zone, FMCOU and FMIOU (Figure 6.5b and d) do not match significantly with observed and FMFI (yellow arrows), probably due to the overburden influence in a case where the velocity model is inaccurate. However, FMCOU and FMIOU are similar in the regions indicated by blue arrows. The black dashed ellipses highlight zones of null blocks in the reservoir simulation model.

Figure 6.6 illustrates the 3D amplitude results for another vertical section. Figure 6.6b and d highlight the presence of null blocks in the simulation model, indicated by the red arrows, therefore no amplitude data was being generated.

In the lower part of the reservoir (denoted by the black dashed ellipses), the observed data and FMFI case Figure 6.6a and c exhibit lower amplitude values compared to the modeled results from FMCOU and FMIOU cases (Figure 6.6b and d), although their polarity matches quite well. The regions indicated by the yellow arrows highlight inconsistencies in the FMIOU when compared to the modeled and observed amplitudes. These inconsistencies are attributed to variations in the velocity model, as described in the previous figure. The discrepancies suggest that further refinement of the velocity model is required to improve the alignment between the modeled and observed data.

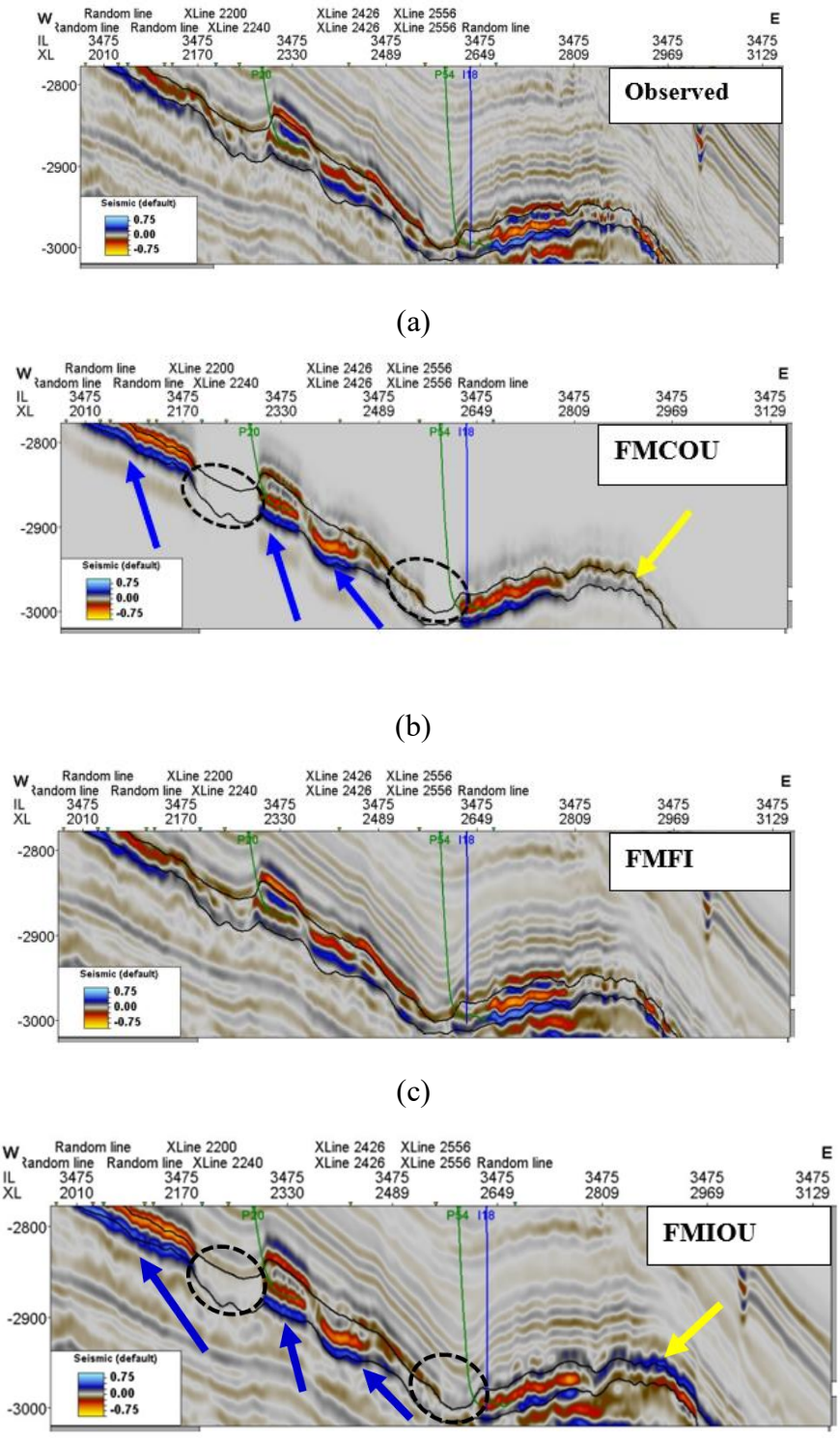

Figure 6.5: Vertical sections of 3D seismic amplitude of a) observed data; b) FMCOU; c) FMFI; d) FMIOU approaches. The yellow arrows indicate a region of polarity reversal in the FMIOU case due to overburden influence in cases of velocity model inaccuracies. The blue arrows highlight regions where FMCOU and FMIOU exhibit similar behavior. The black dashed ellipses mark zones of null blocks in the reservoir simulation model.

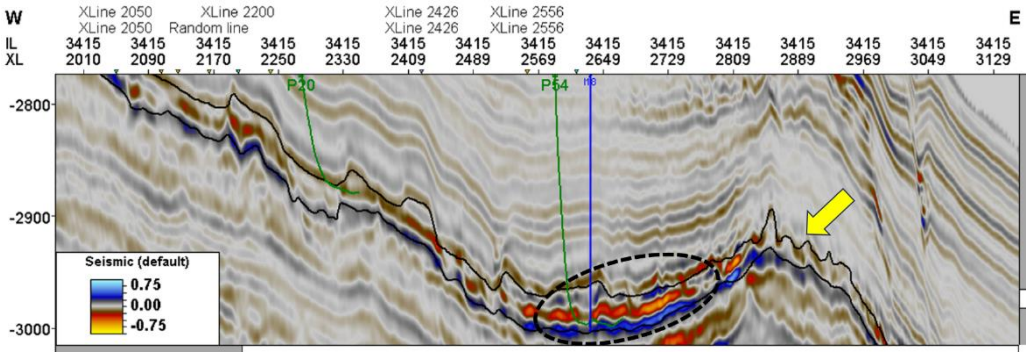

(a)

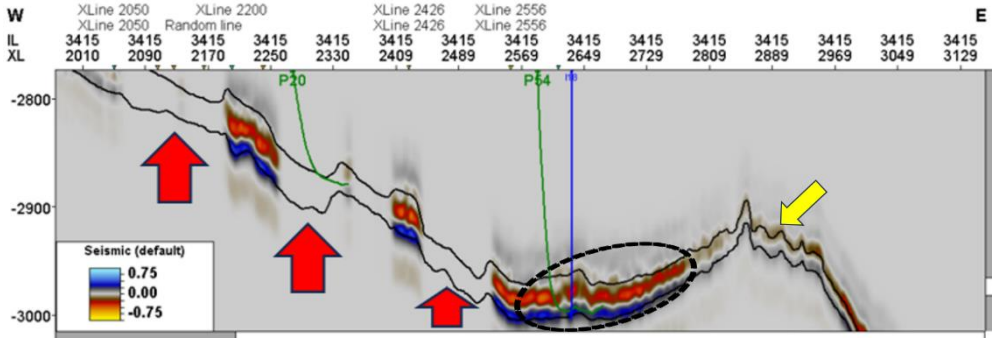

(b)

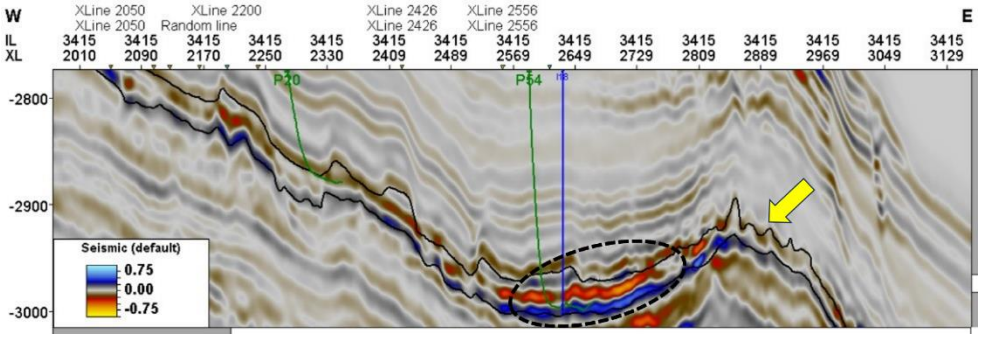

(c)

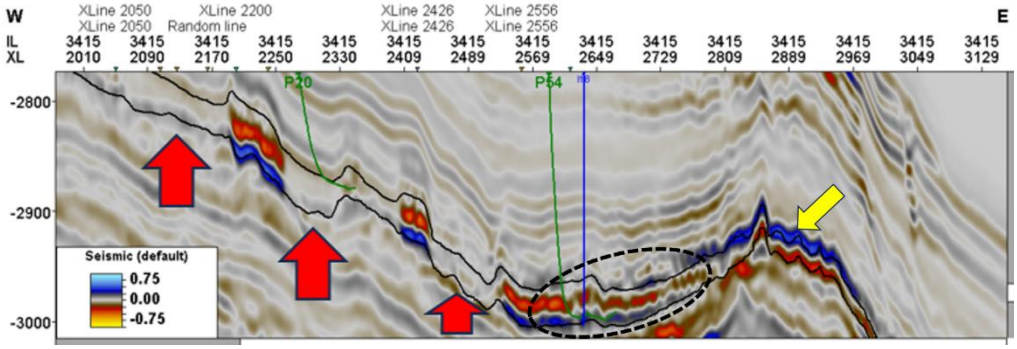

(d)

Figure 6.6: (a) Observed 3D seismic amplitude; (b) FMCOU modeled seismic amplitude; (c) FMFI modeled seismic amplitude; (d) FMIOU modeled seismic amplitude, shown as vertical sections.

This visualization underscores the significance of accurate overburden and underburden modeling on the synthetic seismic response within the reservoir unit. Notably, the reflections exhibit variations in both structure and amplitude within the reservoir, thereby highlighting the critical impact of accurate modeling approaches to properly evaluate the AB-140 reservoir's seismic response. The red arrows indicate null blocks in the simulation model where no flow occurs, while the yellow arrows indicate a region of polarity reversal in the FMIOU case due to overburden influence and velocity model inaccuracies.

6.3.2 4D Impedance comparative analysis

The 4D impedance of the observed data, obtained through acoustic inversion, was evaluated against the different modeled cases. Figure 6.7 presents vertical sections of the 4D impedances, which were calculated as the differences between the monitor and the baseline surveys. The comparative analysis shows no substantial differences between the three forward modeling approaches (Figure 6.7b, c, d). This outcome was anticipated, as all three cases are based on results derived from the PEM. Besides, none of the modeled impedances perfectly match the observed data.

In particular, regions labeled "A" in the sections indicate areas where the modeled 4D impedance shows hardening, whereas the observed data displays softening, even with some noise present in the dataset. On the other hand, regions labeled "B" exhibit a noticeable mismatch between the modeled and observed data, with the observed data showing softening effects, while the modeled data indicate hardening. It is important to note that this region is highly affected by noise and should not be relied upon as a basis for comparison.

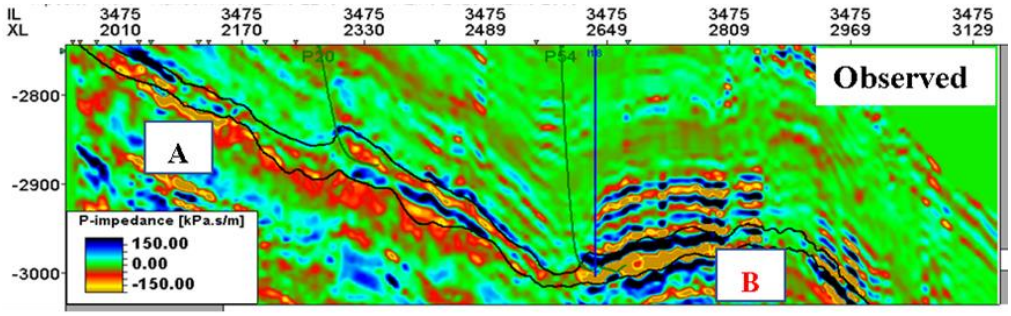

(a)

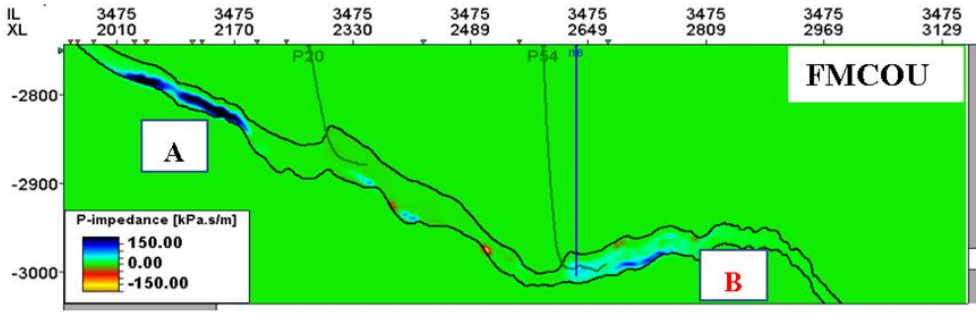

(b)

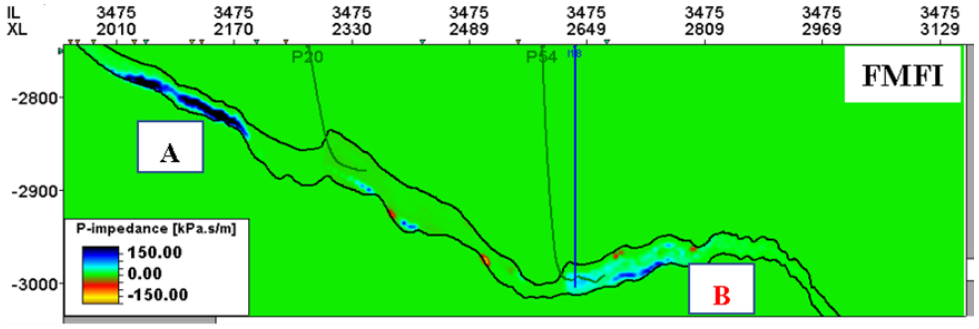

(c)

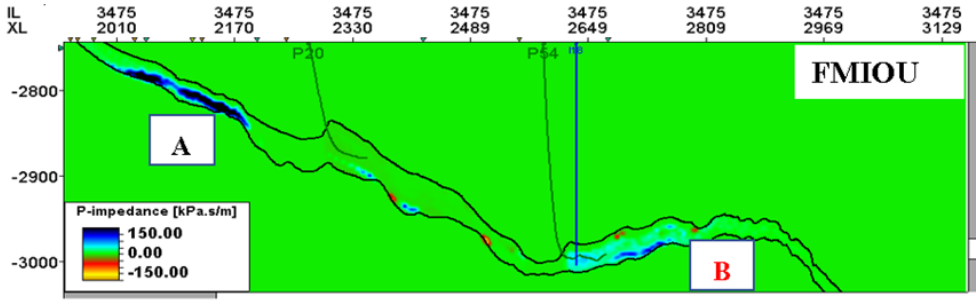

(d)

Figure 6.7: Vertical sections of 4D impedances of: a) observed; b) FMCOU; c) FMFI; d) FMIOU.

6.3.3 4D Amplitude comparative analysis – no noise

This section examines the 4D amplitude results of three distinct approaches, without considering the impact of noise addition to the modeled amplitudes. Figure 6.8 illustrates vertical sections of the 4D amplitude differences between the monitor and baseline for the observed data, as well as for the FMCOU, FMIOU, and FMFI. The results obtained from all cases are similar, indicating that the choice of modeling approach does not significantly impact the overall 4D analysis. As such, any of the modeled amplitudes can be effectively compared with the observed 4D amplitudes. The region indicated by the letter B shows very weak modeled 4D signals with no major alignment with the observed 4D amplitudes. In the up-dip section of the reservoir marked as A, the observed data shows a softening effect, while the modeled data exhibits a hardening anomaly. This discrepancy between the observed and the modeled 4D amplitudes suggests that the model may be inaccurate in this region.

Figure 6.9 illustrates another example of the 4D amplitude differences between the monitor and baseline for the observed data, as well as for the FMCOU, FMIOU, and FMFI cases. As seen previously, the comparison reveals no significant differences among the three modeled approaches. The region indicated by the letter A shows a weak modeled 4D signal (possibly hardening) with no major alignment with the observed 4D amplitude, in which a strong softening is noticed. In the up-dip section of the reservoir, the observed data shows a softening effect, while the modeled data exhibits a very weak hardening anomaly. This discrepancy between the observed and the modeled 4D amplitudes confirms the previous conclusions on the model inaccuracy. Based on the findings derived from these analyses, it is evident that the modeling methodologies exert minimal influence on the 4D amplitudes. The incorporation of noise in this case may assume a pivotal role in the comparison process, highlighting areas of low data quality in which the interpretation is uncertain. We will examine next the implications of the added noise on the modeled amplitudes.

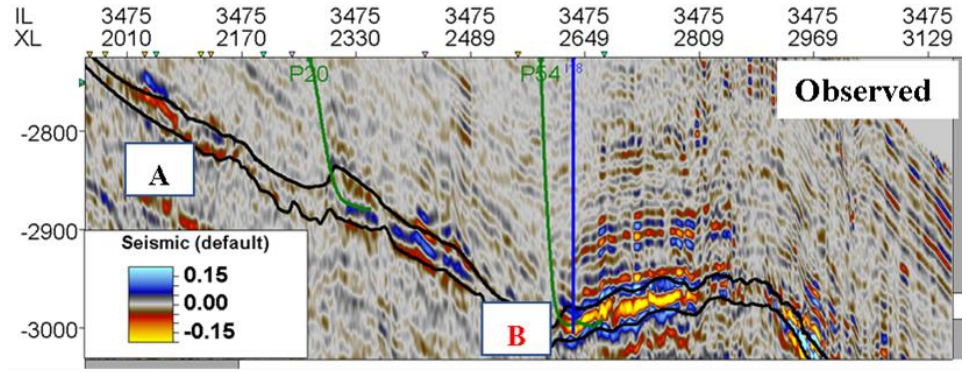

(a)

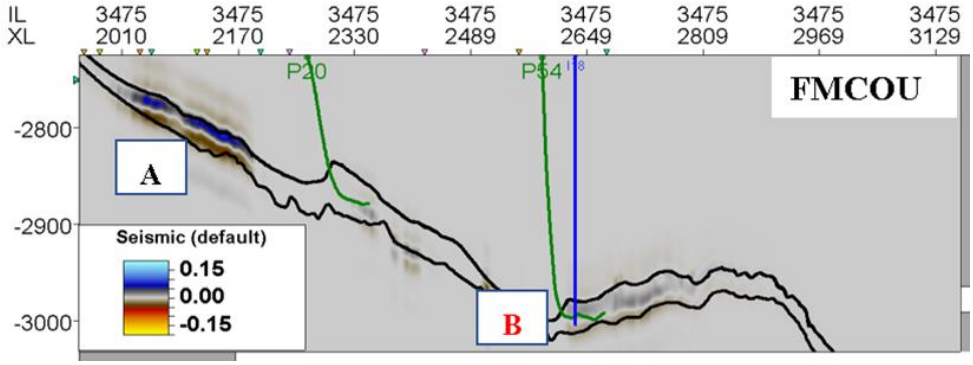

(b)

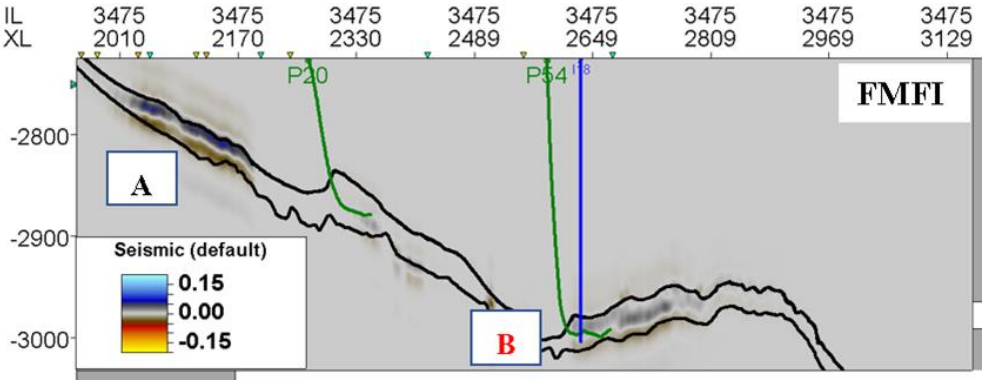

(c)

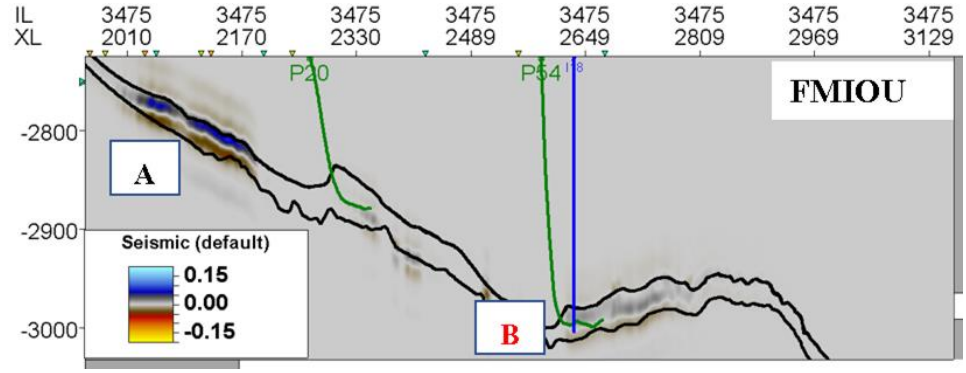

(d)

Figure 6.8: Vertical sections of 4D amplitudes of (a) observed; (b) FMCOU; (c) FMFI; (d) FMIOU.

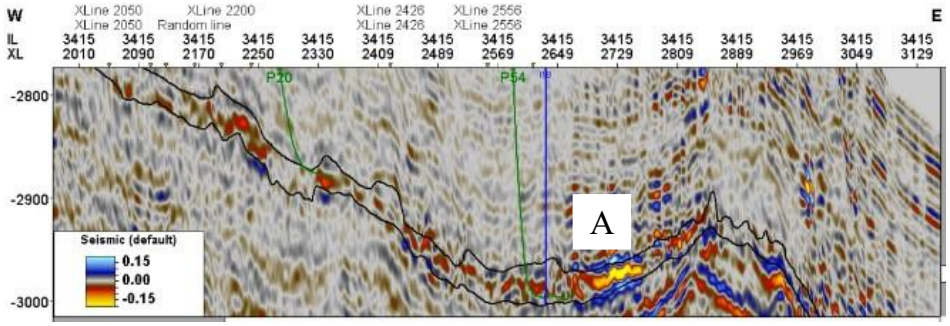

(a)

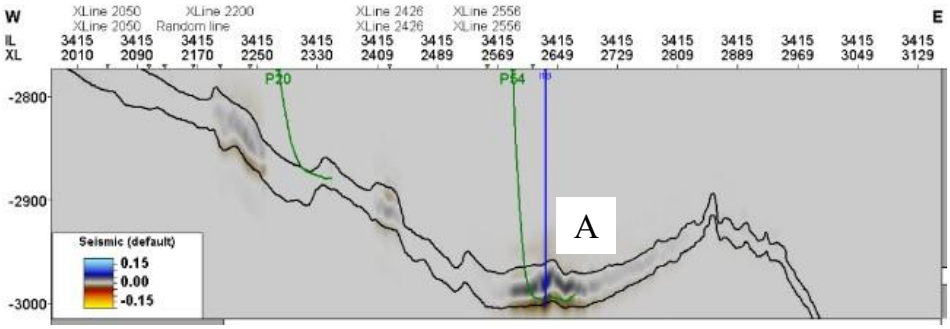

(b)

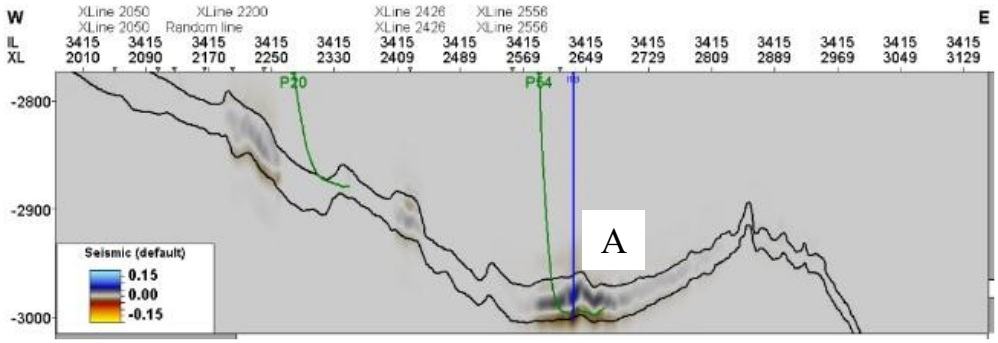

(c)

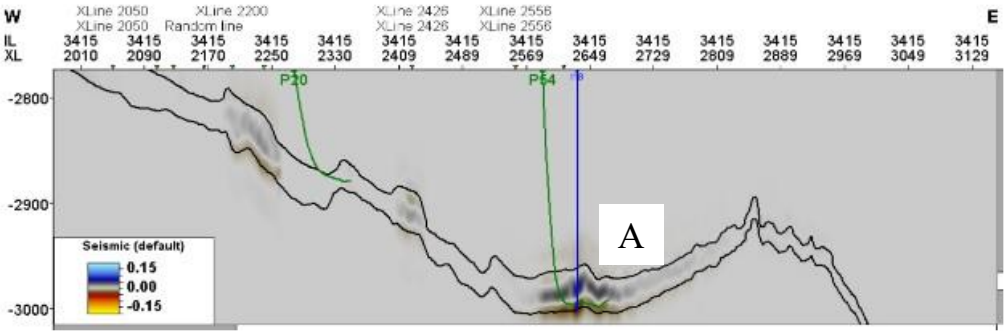

(d)

Figure 6.9: Vertical sections of 4D amplitudes of (a) observed; (b) FMCOU; (c) FMFI; (d) FMIOU.

6.4 Noise modeling

In this study, noise was added to the synthetic seismic amplitudes to closely replicate the conditions of real-world seismic acquisitions, where seismic signals are accompanied by various types of noise. Figure 6.10 shows the NRMS maps for the modeled data with noise for cases FMCOU, FMIOU, and FMFI. The red regions visible in the map corresponds to areas with significantly high NRMS values. These high NRMS values are indicative of low repeatability and high noise level, suggesting issues with data acquisition. To adjust the noise levels of modeled data to be similar to the observation, a scaling factor of 3 was applied to the residual noise added to FMIOU and FMFI cases, while a scaling factor of 12 was applied to the random noise of FMCOU. The mean NRMS values for these comparisons were recorded as 27%, 26% and 26%. These values are similar to the mean value found for the observed data (27%), see Figure **5.7**.

The analysis indicates that while the seismic data are generally within acceptable repeatability ranges for streamer acquisition, certain areas exhibit suboptimal quality due to high NRMS values, likely caused by acquisition challenges (see Figure 5.7). These problematic zones require careful consideration during our analysis, as they can impact time-lapse interpretation and reservoir monitoring accuracy. Figure 6.11 shows the vertical section of the noise added to the baseline survey for different modeling approaches, after applying scalability.

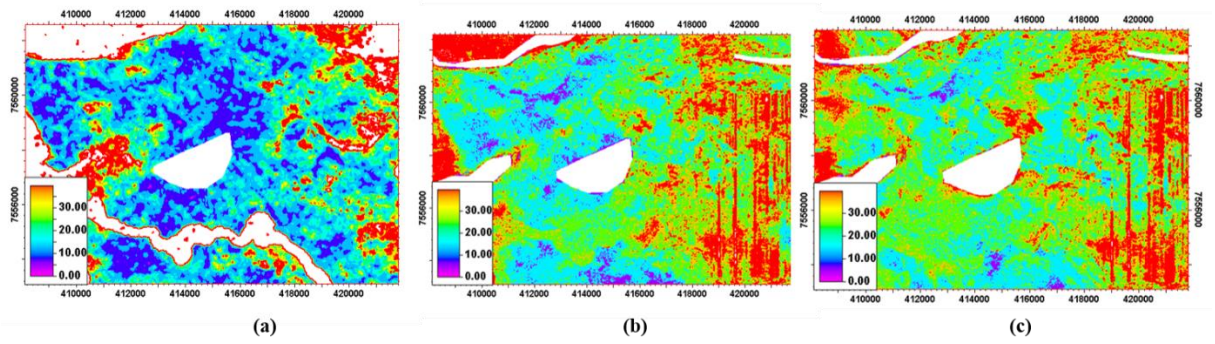

Figure 6.10: (a) Normalized root mean square (NRMS) map for FMCOU, extracted at 10ms window above and 100ms below the AB140 reservoir zone; (b) NRMS map for FMIOU, extracted at 100ms window above the AB140 reservoir zone until the AB140 top; (c) NRMS map for FMFI, extracted at 100ms window above the AB140 reservoir zone until the AB140 top.

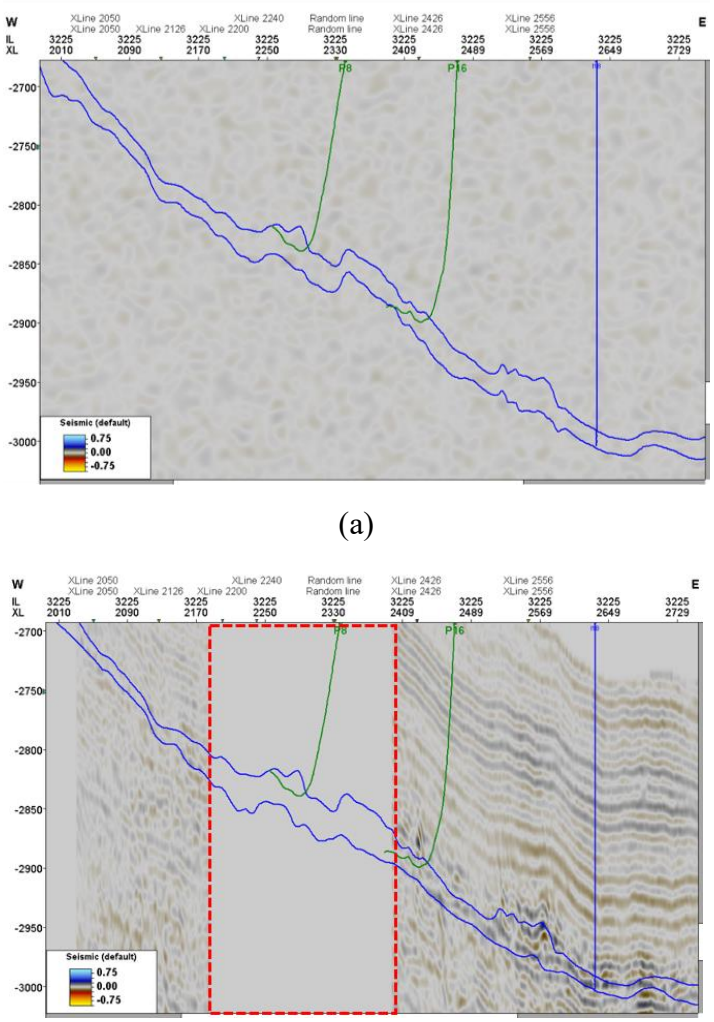

Figure 6.11: Vertical sections of 3D baseline noise: (a) random noise and (b) residual noise from seismic inversion. The red box in the residual noise highlights region affected by platform restrictions during seismic acquisition.

6.4.1 3D Amplitude comparative analysis with noise

This section presents a comparison of the 3D amplitude analysis for the different modeling approaches after adding noise to the synthetic amplitudes. The aim is to assess how noise affects the synthetic amplitudes and how closely they resemble the observed 3D amplitudes. Figure 6.12 illustrates a vertical section of the 3D seismic amplitude from the baseline survey for the observed data, as well as for the FMCOU, FMIOU, and FMFI cases with noise added. The black continuous horizons represent the top and base of the AB140 reservoir.

As noticed before, FMFI shows a good match with the observed amplitudes (Figure 6.12a and c). When the residual noise is introduced, this match is further improved, as anticipated. This observation is also true for FMIOU case, which shows an increase in the reflections magnitude in regions that include high intensity of residual noise. This is because

the high-noise level in some regions are summing up some reflections to the synthetics, making them to be stronger. Such regions, should be carefully evaluated because it is uncertain and the signals may be not real. FMCOU (Figure 6.12b and d) exhibit similar mismatch with both the observed data and FMFI when noise is added. Different scalars were applied along the tracers in FMCOU based on the NRMS of the real data. This adjustment was necessary to account for discrepancies and improve the comparability of the modeled results. Comparing these results with the earlier analysis without noise highlights the influence of data quality on evaluating the amplitude accuracy.

Nevertheless, the amplitude polarity of top and base horizons between the modeled and observed data remains consistent.

The addition of residual noise to the modeled amplitude proved beneficial as it approximates the signals and aligns the modeled data closer to the observed. This adjustment provides a clearer representation of areas where comparisons are uncertain due to high noise levels. The random noise remains a viable alternative when inversion residuals are unavailable. Random noise can still provide meaningful insights into the data distortion caused by noise and improve the comparison with observed seismic data.

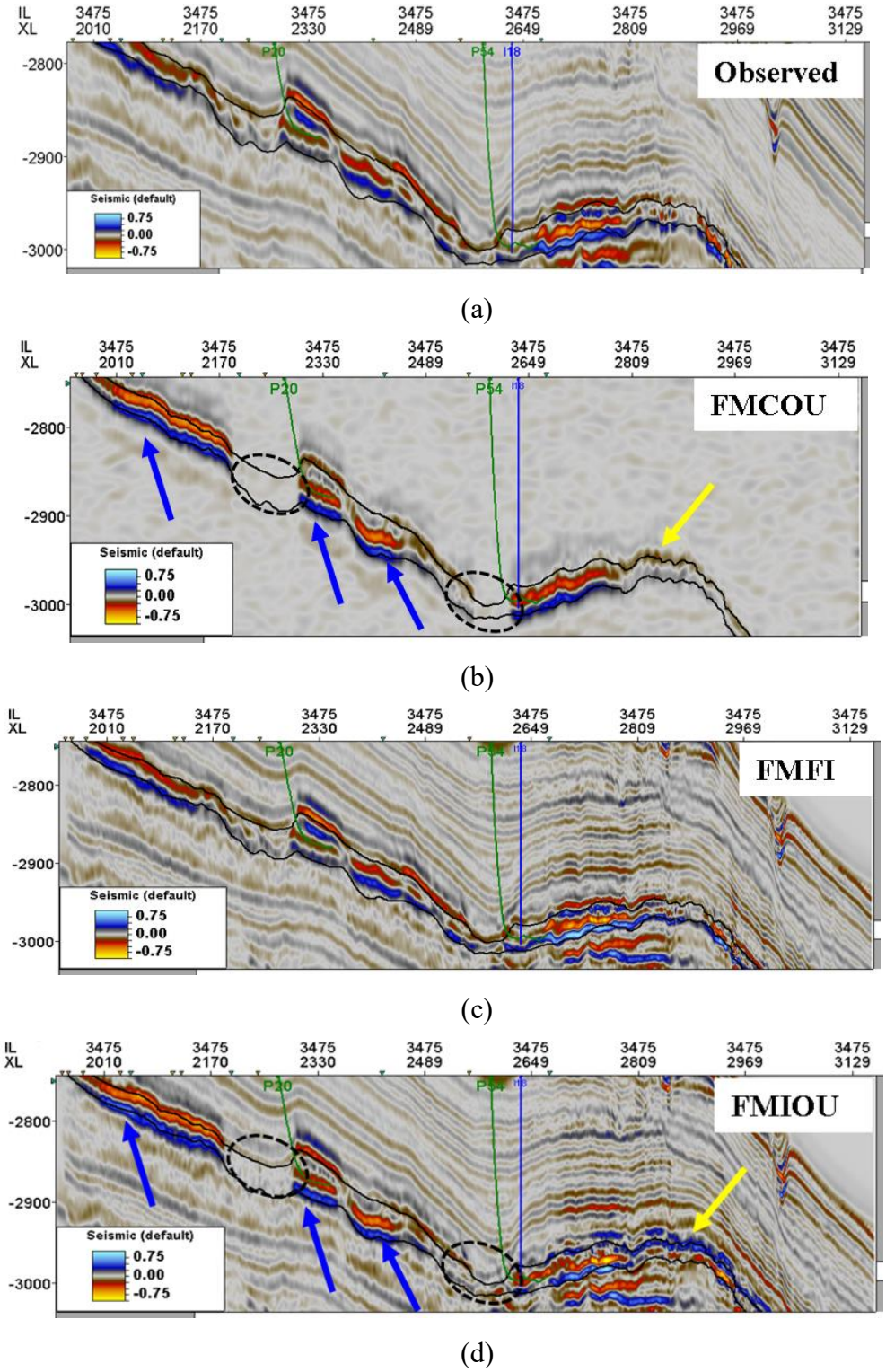

Figure 6.12: 3D seismic amplitude vertical sections of baseline survey of: a) observed; b) FMCOU; c) FMFI; d) FMIOU. The yellow arrows indicate a region of polarity reversal in the FMIOU case due to overburden influence in cases of velocity model inaccuracies. The blue arrows highlight regions where FMCOU and FMIOU exhibit similar behavior. The black dashed ellipses mark zones of null blocks in the reservoir simulation model.

6.4.2 4D Amplitude comparative analysis with noise

Figure 6.13 illustrates the 4D amplitude differences between the monitor and the baseline for the observed data and the FMCOU, FMIOU, and FMFI modeling approaches, after noise was introduced.

For interpreters, the FMFI and FMIOU models provide results more closely aligned with the observed data. However, this apparent improvement is largely influenced by the addition of noise to the modeled amplitudes rather than by the accuracy of the modeling itself. Noise artifacts in the data can mask genuine signals and introduce false anomalies, as seen in the region marked "B".

To improve the reliability of the interpretation at "B", it is critical to analyze both noisy and noise-free datasets. This differentiation ensures that the observed anomalies are genuinely related to the model and not artifacts of noise. The discrepancies observed in the FMCOU model emphasize the importance of improve the simulation model, or the petro-elastic model.

Finally, from an interpretative perspective, the FMFI and FMIOU models provide results more closely aligned with the observed data, yet this correlation is driven more by the incorporation of noise than by the precision of the overburden modeling itself

The 4D amplitudes derived from the FMIOU and FMFI cases exhibit remarkable similarity, as noted previously. In contrast, the FMCOU model shows significant differences, especially in the region labeled "B". This area highlighted by both a yellow ellipse and letter “B”), illustrates the advantage of using residual noise over random noise is evident, as the former highlights the high level of noise present in the observed data. This serves as a warning of the greater uncertainty and care required in the interpretation of 4D signals and the analysis of model accuracy. Incorporating noise into synthetic amplitudes helps create more realistic models that better replicate actual field data.

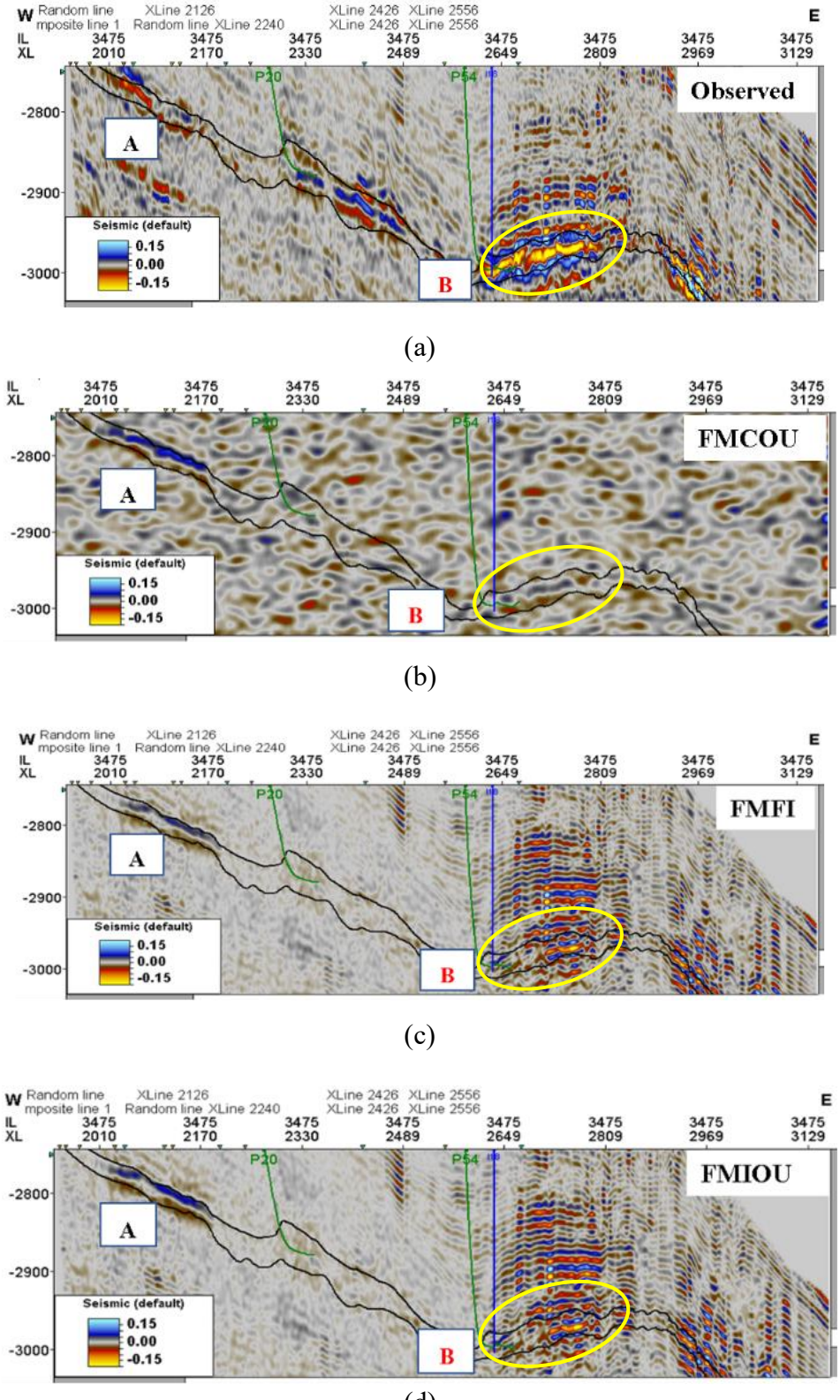

Figure 6.13: Vertical sections of 4D amplitudes of (a) observed; (b) FMCOU; (c) FMFI; (d) FMIOU. The yellow ellipse demonstrates the impact of noise, where residual noise enhances the visibility of the anomaly, revealing a higher noise level in the observed data compared to random noise

6.5 4D seismic attribute maps comparative analysis (amplitude with no noise)

The 4D seismic attribute known as dRMS, derived from differences in RMS amplitude maps (see equations 4.2 and 4.3) from baseline and monitor surveys, was utilized to identify regions of discrepancy within the reservoir. This initial map analysis does not consider noise addition. Figure 6.14 presents the dRMS maps for amplitude of both observed and modeled data, extracted between the top and base of the AB140 reservoir, in which significant deviations are evident, revealing key trends in the reservoir dynamics.

The modeled noiseless amplitudes (Figure 6.14b-d) are characterized by blue blotches, reflecting hardening effects caused by water saturation increases. These regions align with the ΔSw map in Figure 6.2d, where water saturation leads to a relative impedance increase (ΔIP, Figure 6.2a). The modeled data emphasize fluid saturation changes, specifically water injection effects, as the primary driver of impedance increases.

Regions with minimal or no hardening effects in the modeled maps indicate underrepresentation of gas saturation (ΔSg, Figure 6.2c) and pressure depletion (ΔP, Figure 6.2b). This imbalance suggests that the simulation model overemphasizes water saturation effects, leading to limited representation of areas dominated by gas exsolution and pressure-driven softening. For example, areas with increased impedance in the modeled maps (ΔSw-driven hardening) correspond to blue regions in Figure 6.14b-d, but the modeled data do not adequately capture the impact of gas exsolution or pressure depletion as indicated by trends in ΔSg and ΔP maps in Figure 6.2. The black dashed circles in Figure 6.14 highlight areas where substantial mismatches exist between the modeled and observed data. These discrepancies suggest that fluid effects, particularly water saturation, dominate the modeled responses, whereas the observed data indicate that pressure changes and gas exsolution exert a stronger influence in these regions. For instance, regions of increased impedance in the modeled maps (ΔSw-driven hardening) do not align well with the observed softening signals attributed to pressure depletion and gas exsolution. This suggests an overestimation of water saturation effects and an underrepresentation of pressure-driven impacts.

.

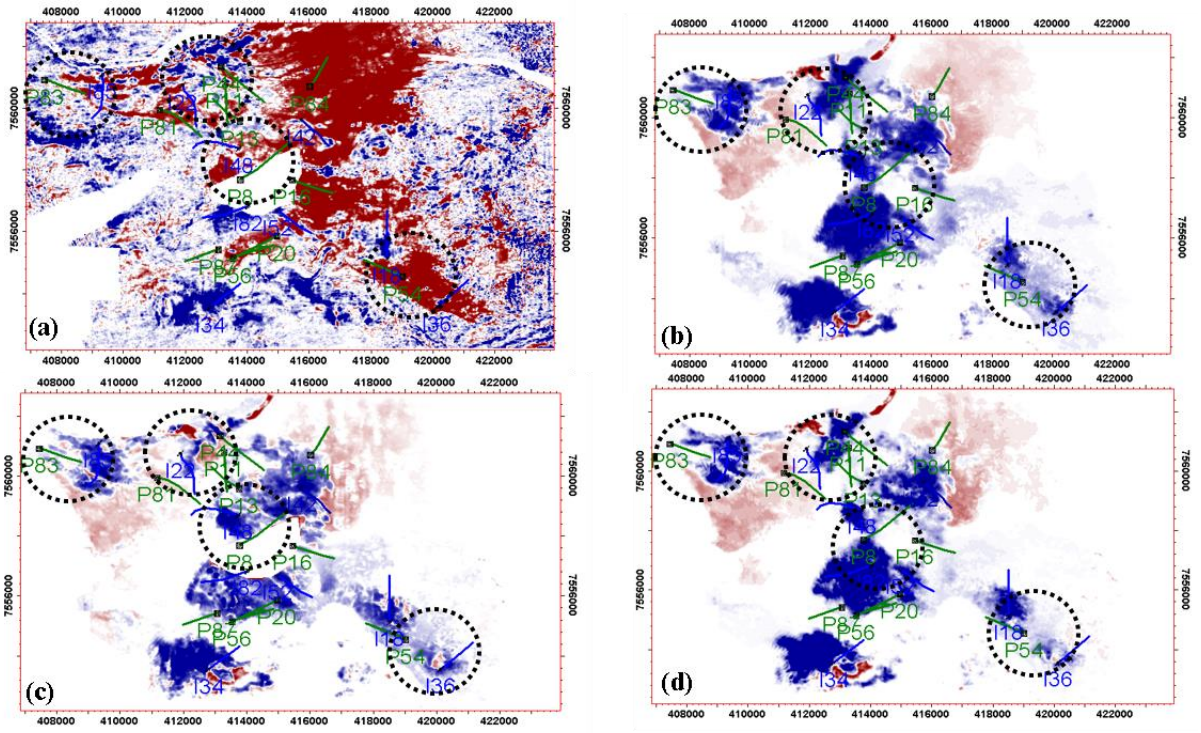

Figure 6.14: dRMS maps calculated between top to bottom of AB140 zone of: (a) observed amplitude (full stack data); (b) modeled amplitude for FMCOU case; (c) modeled amplitude for FMFI case; (d) modeled amplitude for FMIOU case. The modeled amplitude shown are noiseless. The black dashed circles highlight areas of substantial mismatch between the modeled and observed data.

6.6 4D seismic attribute maps comparative analysis (amplitude with noise added)

For a fair comparison, noise was added to the modeled amplitude and the dRMS maps were recalculated to assess the reservoir regions. Figure 6.15 illustrates the dRMS maps for observed and modeled data, extracted between the top and base of the AB140 reservoir. As in the noiseless case, significant mismatches persist between the observed and modeled 4D seismic responses, which could be attributed to a simulation model that is unreliable. A contributing factor to this is that the simulation model may not fully capture the dynamic behavior of the reservoir.

In certain regions, such as around well I34 (see red box in Figure 6.15a), there is reasonable agreement between the observed and modeled data. In contrast, the central "N" region in Figure 6.15a shows a poor match. This region corresponds to an area of poor seismic coverage, where a gap in the seismic data prevents an accurate match between the observed and modeled attributes. The observed map (Figure 6.15a) is dominated by red blotches (yellow

boxes), which suggest softening due to pressure depletion. The blue regions in the modeled data indicate areas of hardening caused by increased water saturation from water injection.

The FMCOU case (Figure 6.15b) is dominated by blue regions (designated "H" for hardening), particularly in the central and bottom parts of the map. This suggests that the modeled seismic response reflects a stiffening of the reservoir, which is inconsistent with the observed softening. Comparing this to the noiseless case discussed earlier, there are big mismatches between observed and modeled dRMS maps. In the noiseless case, the observed data primarily displayed softening (red blotches), while the modeled data showed a much larger presence of hardening (blue blotches).

The addition of noise has introduced variability into the modeled amplitudes, bringing the model closer to real reservoir conditions. For instance, in the FMFI case (Figure 6.15c), adding noise led to a slight improvement in the match between observed and modeled data. While the blue blotches (hardening) still dominate, they are now more evenly distributed across the map, particularly on the left side, reflecting better agreement with the observed data. The FMIOU case (Figure 6.15d) shows the most balanced mix of red and blue blotches, compared to the FMCOU case.

This analysis highlights the critical role of adding noise to the modeled data in improving the comparison between observed and simulated 4D seismic responses. While the discrepancies are not fully resolved, noise helps mitigate some of the oversimplifications inherent in the noiseless case.

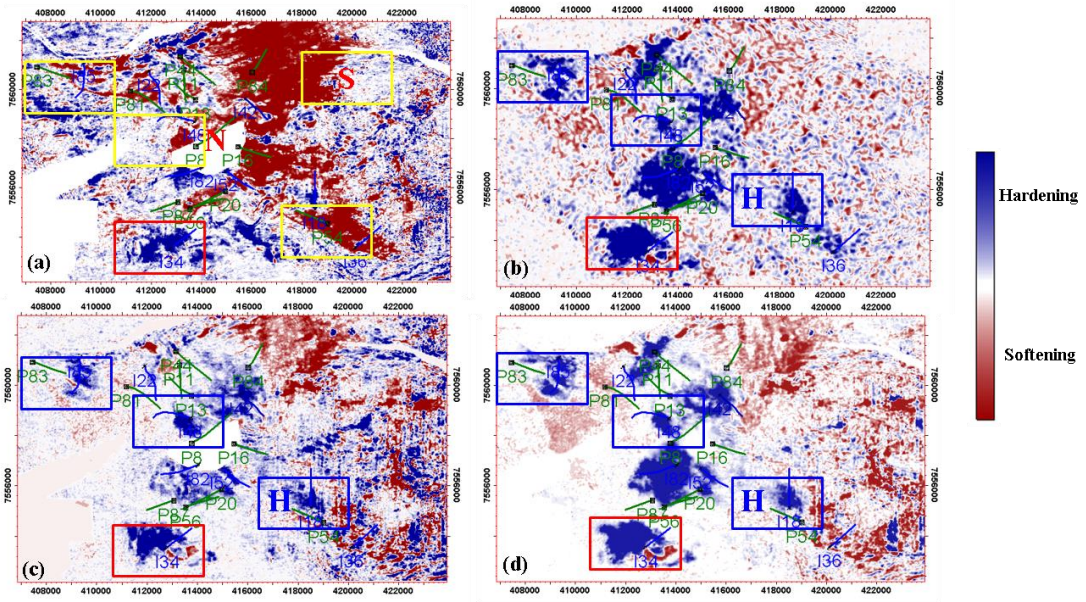

Figure 6.15: dRMS maps calculated between top to bottom of AB140 zone of: (a) observed amplitude (full stack data); (b) modeled amplitude for FMCOU case with noise added; (c) modeled amplitude for FMFI case with noise added; (d) modeled amplitude for FMIOU case with noise add The red box highlights a region where the observed and modeled data show reasonable agreement. The yellow boxes, labeled "S", indicate areas dominated by softening effects, likely due to pressure depletion, which is more prominent in the observed data. The blue boxes, labeled “H”, mark regions of hardening caused by increased water saturation from water injection, which is more dominant in the modeled data.

The mismatch between observed and modeled data suggests that the model does not fully capture the softening effects present in the observed dataset.

6.7 Production data matching evaluation and model refinement

This section evaluates the matching of the simulated production data in relation to the observed. The primary objective is to adjust the reservoir model to try improve the matching with observed 4D seismic data. For this evaluation, the NQDS is utilized to quantify the quality of the match and identify regions where the model fails to accurately replicate reservoir dynamics. These insights help pinpoint critical regions, summarize overall well performance, and propose targeted adjustments to reservoir properties such as permeability, porosity.

As running a proper history matching is out of the scope of this work, the model calibration comprises manually tuning the porosity field with the application of multipliers. This refinement process aims to reduce discrepancies by updating the model based on well performance data and seismic information. Porosity was selected as the primary parameter for modification due to its strong influence on pressure behavior and its direct relationship with acoustic impedance. However, since porosity governs pore volume, such modifications are

uncommon in reservoir studies. In this case, this approach was employed as a preliminary analysis to observe its impact on the modeled amplitudes and production curves.

Normalized quadratic distance with signs (NQDS)

In this study, a tolerance of 5% was applied to calculate NQDS for bottom-hole pressure (BHP), 10% for oil rate (Qo) and water rate (Qw), and 15% for gas/oil ratio (GOR), with an acceptable range (AR) refers to a predefined interval used to assess the quality of history-matching models in reservoir simulations, ensuring that the mismatch between simulated and observed data falls within an acceptable error margin.The AR was set within (-10, +10), meaning models with NQDS values within this range are considered acceptable matches. This threshold was chosen based on the judgment of the reservoir simulation model and found to be a reasonable limit for assessing history-matching quality while accounting for uncertainties in production and pressure data. Green points in the NQDS plots indicate positive values, signifying an overestimation of the simulated profile relative to the history data. Conversely, red points represent negative values, indicating an underestimation of the simulated data compared to the history data.

Figures 6.16 to 6.20 show the NQDS values for BHP, GOR, Qo, and Qw, respectively. For producers, BHP indicate that none of the wells fall within the acceptable range. Overestimations are observed in wells P11, P13, P16, P44, and P83, while underestimations occur in wells P8, P20, P54, and P56 (Figure 6.16). These mismatches suggest that the model struggles to capture pressure effects accurately. For injectors (Figure 6.17), BHP shows that only well Inj34 falls within the acceptable range. Overestimations dominate in wells Inj18, Inj22, Inj42, Inj48 and Inj52, while Inj36 shows underestimation. This highlights discrepancies in the model's ability to simulate pressure for injectors.

The Gas/Oil Ratio (GOR) results, shown in Figure 6.18, display smaller errors compared to BHP. Underestimations are prevalent in wells P8, P11, P13, P16, and P44, while wells P20, P54, and P56 exhibit overestimations. Wells P8 and P44 display the best matches, suggesting localized areas of reasonable agreement. The oil rate (Qo), presented in Figure 6.19, shows the best overall match, except P83 falling out of the acceptable range. This better match in oil production might be attributed to the well boundary condition used in the simulation. The wells were constrained using Liquid Rate. This means that the simulator was provided with historical total liquid production rates. Consequently, in case of low water production, the simulator adjusted the oil rate dynamically to honor this constraint.

Water rate (Qw) matching, shown in Figure 6.20, has significant underestimations in wells P8, P11, P13, P54, P56, and P83. Well P54 is the only well within the acceptable range,

while wells P16 and P20 show overestimations, with well P16 having the poorest match. The poor Qw match is indicative that the model struggles to correctly distribute water within the total liquid rate. This suggests that reservoir properties such as porosity, permeability and relative permeability curves may be innacurate. Additionally, since BHP was not the primary constraint, pressure deviations could also be affecting water production discrepancies.

Among the parameters, oil rate (Qo) exhibits the smallest discrepancies, making it the most reliable parameter in the model. In contrast, significant mismatches in BHP and Qw highlight areas requiring refinement, particularly for pressure-related effects and water saturation dynamics. Specific zones of high mismatches include wells P16 (BHP) and P56 (Qw), which require targeted adjustments and further investigation.

This analysis builds upon the evaluation of production data, providing a quantitative assessment of the alignment between simulated and observed profiles. These findings also complement earlier 4D seismic analyses, emphasizing the need for iterative adjustments to reservoir parameters to address identified mismatches. Based on these observations, adjustments to key reservoir property, porosity, will be applied using multipliers.

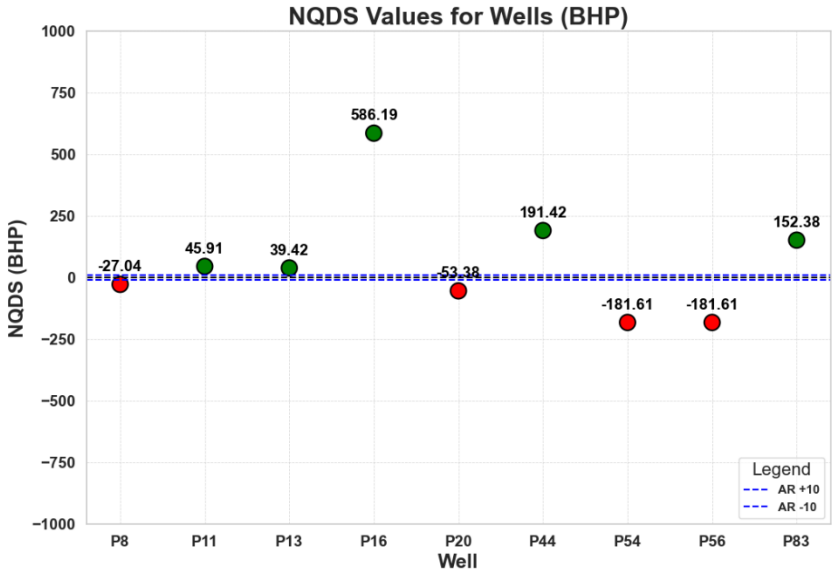

Figure 6.16: NQDS plot for BHP from producers. The dashed blue lines represent the acceptable range (AR) of ±10, which defines the threshold for determining whether the simulated data reasonably matches the observed data. Points within this range indicate an acceptable match, while points outside suggest a significant deviation between the modeled and BHP.

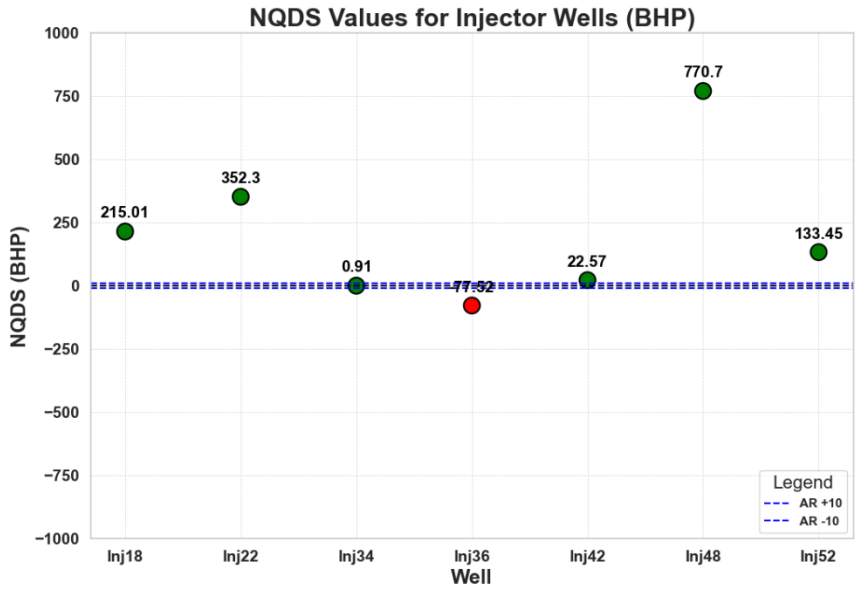

Figure 6.17: NQDS plot for BHP from injectors The dashed blue lines represent the acceptable range (AR) of ±10, which defines the threshold for determining whether the simulated data reasonably matches the observed data. Points within this range indicate an acceptable match, while points outside suggest a significant deviation between the modeled and observed BHP.

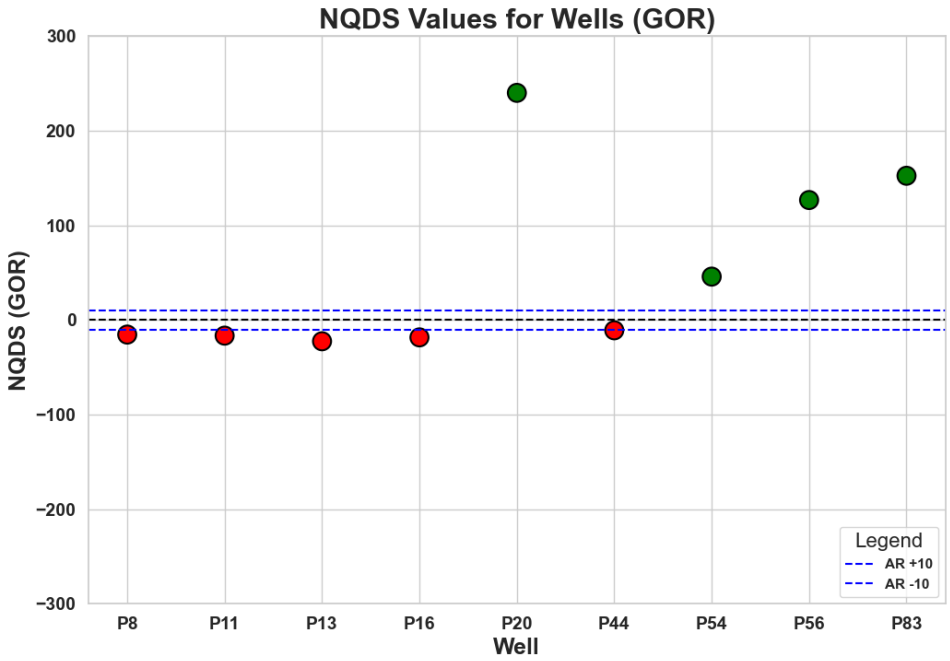

Figure 6.18: NQDS plot for GOR. The dashed blue lines represent the acceptable range (AR) of ±10, which defines the threshold for determining whether the simulated data reasonably matches the observed data. Points within this range indicate an acceptable match, while points outside suggest a significant deviation between the modeled and observed GOR.

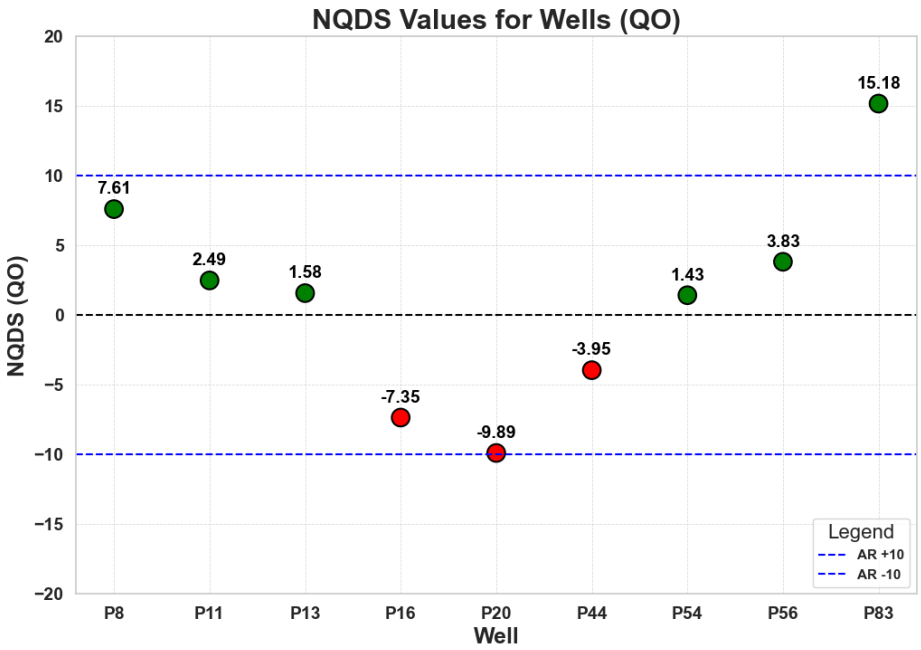

Figure 6.19: NQDS plot for (Qo). The dashed blue lines represent the acceptable range (AR) of ±10, which defines the threshold for determining whether the simulated data reasonably matches the observed data. Points within this range indicate an acceptable match, while points outside suggest a significant deviation between the modeled and observed oil rates.

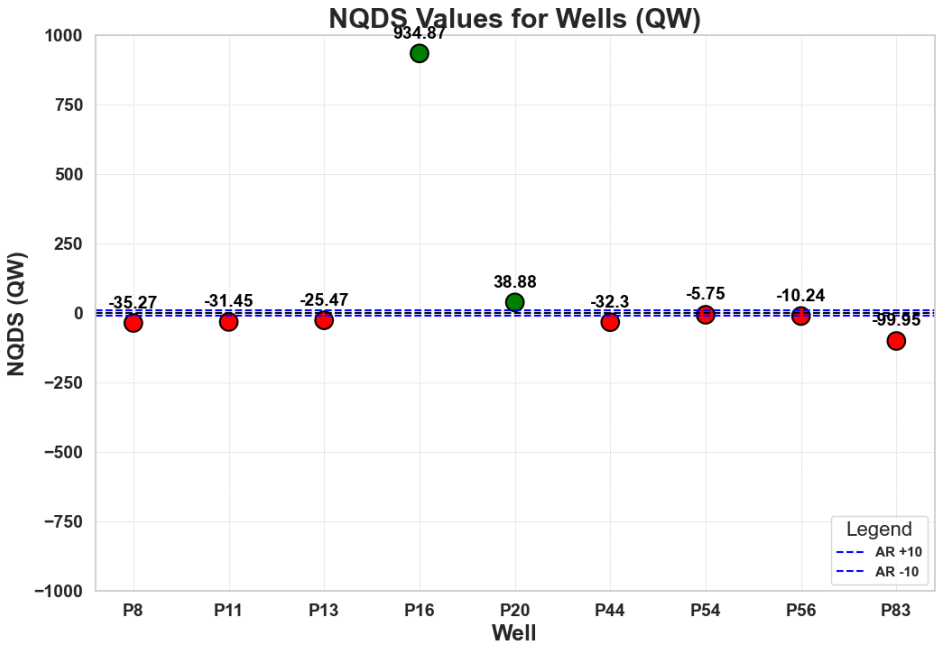

Figure 6.20: NQDS plot for (Qw). The dashed blue lines represent the acceptable range (AR) of ±10, which defines the threshold for determining whether the simulated data reasonably matches the observed data. Points within this range indicate an acceptable match, while points outside suggest a significant deviation between the modeled and observed water rates.

6.7.1 Detailed well production profiles evaluation

In this section, the (BHP) profile, oil production rates, water production rates, and gas-oil ratio profiles for selected wells are examined in detail to determine how the mismatches observed in the NQDS analysis can be reduced and better aligned with historical data. The focus on wells P8, P16, and P56 was chosen as a representative subset to evaluate whether porosity tuning can improve the observed mismatches between simulated and observed profiles. While mismatches exist across most wells, these three were selected to simplify the analysis and illustrate the impact of porosity modifications.

For well P8 Qw (Figure 6.21d) shows a poor correlation between the historical and simulated data. A noticeable increase in water production is observed from 2008 onwards, with the simulated water saturation being underestimated. Despite this, the model reasonably captures the timing of water breakthrough, indicating that the water influx mechanisms are well-represented.

Significant discrepancies are also evident in the BHP profile (Figure 6.21a), particularly at the beginning of the production history, where the simulated pressure fails to align with the historical data. This pressure mismatch is critical, as accurate BHP simulation is essential for predicting reservoir performance and fluid movement. The observed deviations indicate that pressure-related properties, including permeability and porosity, require further refinement. Moreover, potential well productivity issues, such as variations in skin factor or well interference, may be influencing the pressure mismatch and should be examined.

The GOR profile (Figure 6.21b) for P8 displays considerable deviations between the historical and simulated data, particularly from 2009 onwards. The model consistently underestimates the gas-oil ratio, indicating potential inaccuracies in modeling gas saturation or relative permeability to gas. Adjustments in these parameters may be necessary to improve the match. The insights from this analysis justify the need for refining key reservoir parameters.

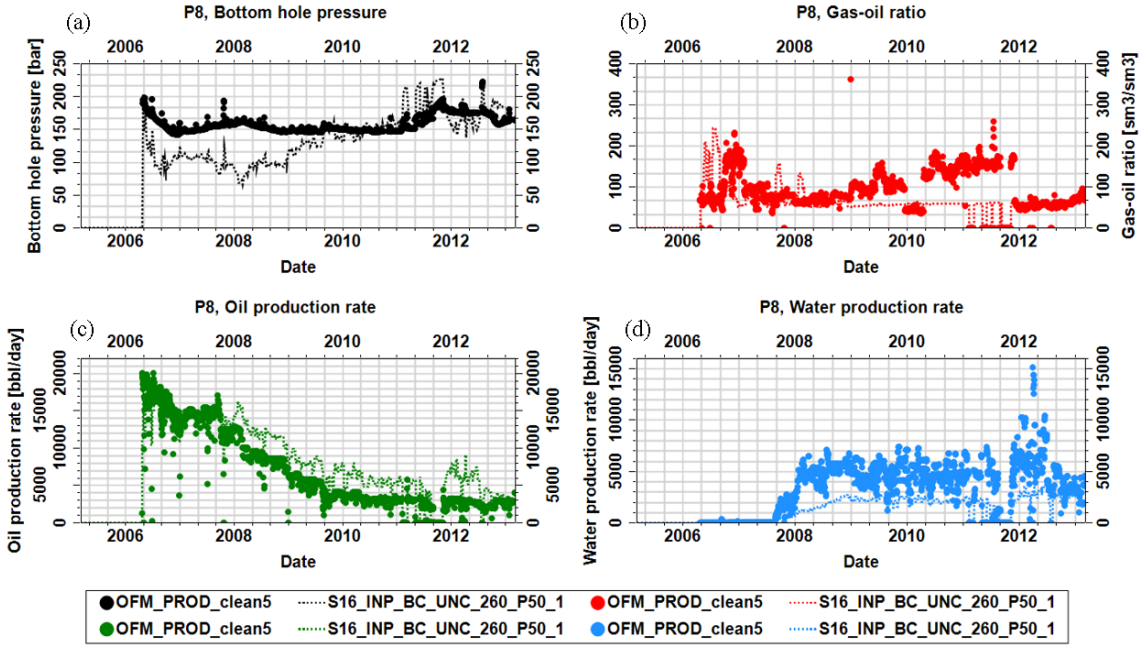

Figure 6.21: Comparison of historical and simulated profiles for well P8 across key production indicators: (a) Bottom Hole Pressure, (b) Gas-Oil Ratio, (c) Oil Production Rate, and (d) Water Production Rate. History data is represented by solid points, while simulated data is shown by dashed lines. The figure highlights the alignment and discrepancies between the model's predictions and observed field data over the production period from 2006 to 2012.

Well P16 was selected for detailed analysis as it exemplifies critical mismatches observed across the field, particularly in BHP and Qw. These issues highlight common challenges in the model's ability to accurately simulate reservoir dynamics, making it a representative case for refinement.

For well P16 the model performs reasonably well in capturing Qo (see Figure 6.22c), with the simulated aligning closely with historical trends. Qw (Figure 6.22d) exhibits a flat behavior, which the model successfully replicates. However, an overestimation of simulated water rate is observed during the later stages of production.

The most significant mismatch for well P16 lies in the BHP profile (Figure 6.22a), where the model consistently overestimates pressure throughout the entire production period. This overestimation is supported by the NQDS values (see Figure 6.16), and is further evidenced by the high mismatch in the 4D seismic comparison. Specifically, the modeled 4D seismic data indicate hardening in the region around Well P16, while the observed data show softening. This contrast highlights discrepancies in how the model represents pressure and fluid saturation changes in this area, requiring further investigation to improve model reliability.The GOR profile for P16 shows relatively low gas production. Although the model captures the overall

trend, minor underestimations are evident during gas production. These deviations in GOR have a limited impact on the overall performance of the well.

The consistent overestimation of BHP necessitates targeted adjustments in pressure-related properties, such as porosity.

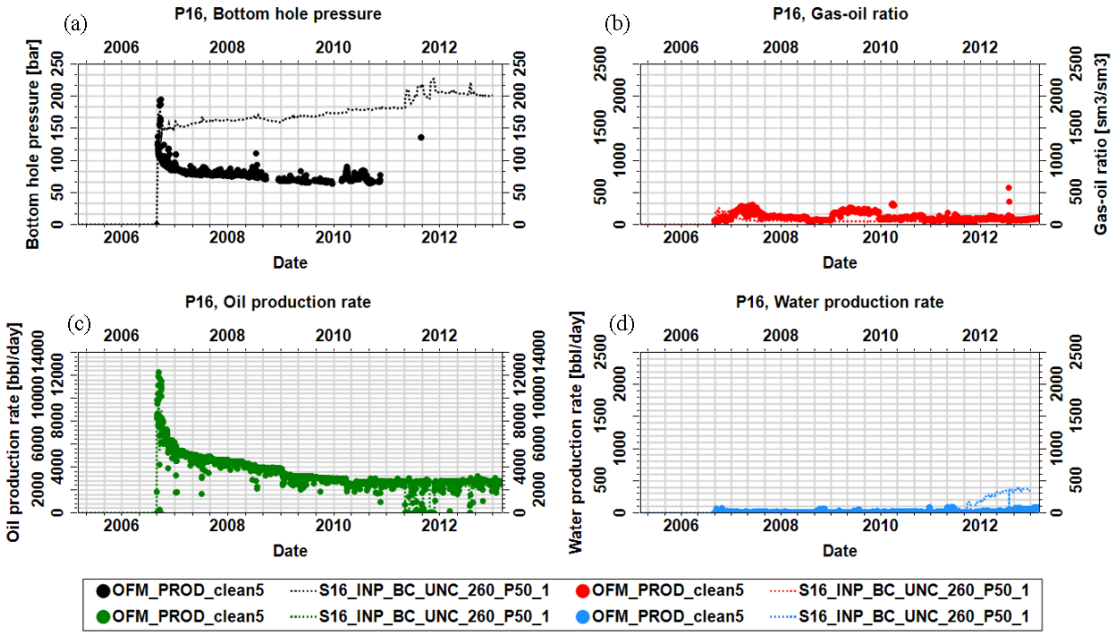

Figure 6.22: Comparison of historical and simulated profiles for well P16 across key production indicators.(a) Bottom Hole Pressure, (b) Gas-Oil Ratio, (c) Oil Production Rate, and (d) Water Production Rate.

The third well here present, P56, was chosen for its consistent underestimation of BHP, which highlights a recurring issue in pressure dynamics modeling across the field. This well also demonstrates reliable Qo predictions, providing a balanced view of model performance.

The GOR (Figure 6.23b) profile shows an overestimation in the early years (2006 – 2008), this is probably related to the pressure decrease that made gas come out of solution. The Qo (Figure 6.23c) exhibits a good match between the historical and simulated data. The Qw (Figure 6.23d) is reasonably well-captured by the model during most of historical period.

However, slight refinements may be necessary to ensure consistency across the entire production period.

The analysis of well P56 underscores the importance of refining pressure behavior in the model. These refinements aim to address the consistent BHP underestimation and improve the alignment of gas production trends in the early years of the production period.

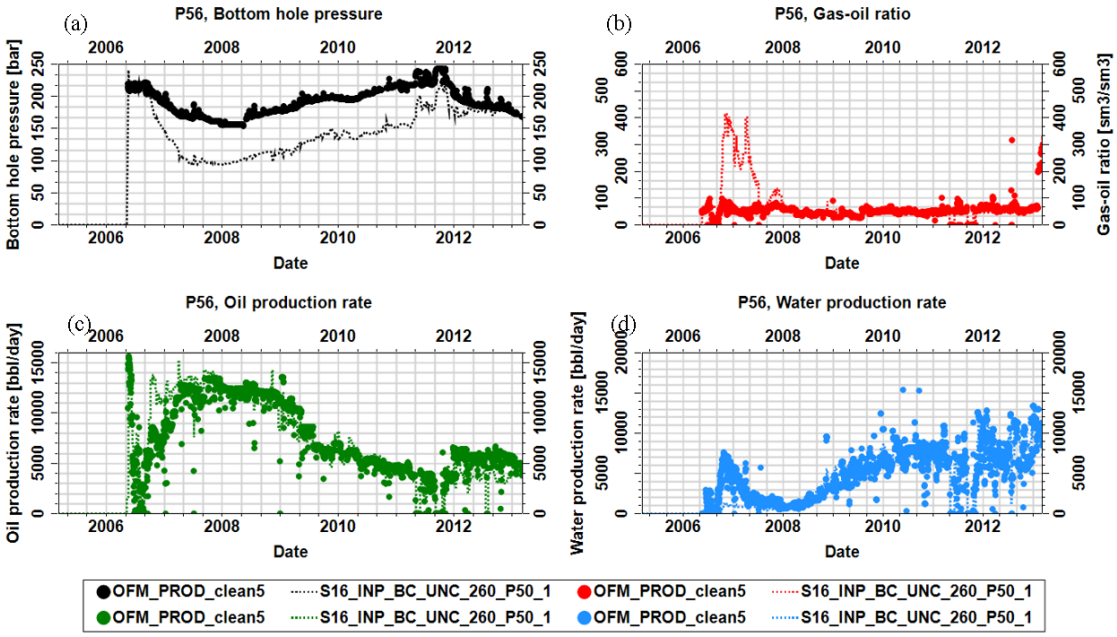

Figure 6.23: Comparison of historical and simulated profiles for well P56 across key production indicators: (a) Bottom Hole Pressure, (b) Gas-Oil Ratio, (c) Oil Production Rate, and (d) Water Production Rate.

6.7.2 Modification of reservoir properties to improve matching

Manual model adjustment was employed to improve the model accuracy, based on the analysis of the matching of well historical data, amplitude, and impedance attributes. More specifically, the primary target of these adjustments was to reduce the mismatches between observed and simulated BHP and other production variables (oil, water, and gas rates) to help improve the model's reliability.

The adjustment was made in the porosity field, which was modified across the whole model by applying three different constant multipliers: 1.1 (10% increase), 1.2 (20% increase), and 0.8 (20% decrease). The decision to focus on porosity tuning was driven by its critical influence on reservoir pressure, which showed the most significant mismatch in the NQDS analysis. Additionally, porosity strongly affects acoustic impedance, making it a key parameter for improving both pressure matching and the accuracy of seismic-based evaluations. Figure 6.24 shows the profiles for BHP obtained after applying each porosity modification for well P8. Despite the porosity adjustments, none of the modifications led to a significant improvement in

matching the simulated data to the observed production history, we noticed that tuning porosity, whether through increases or decreases, did not lead to an improved match between the observed and simulated data for well P8. This suggests that tuning porosity alone is insufficient to improve the model reliability.

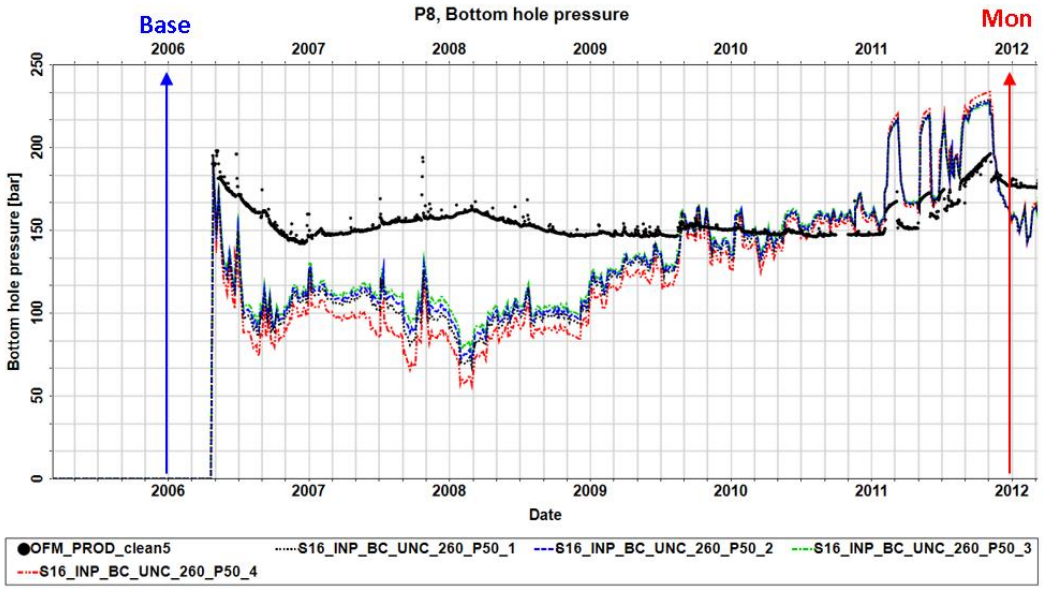

Figure 6.24: Bottom Hole Pressure profile for well P8 showing the observed and simulated data after porosity modifications. The base seismic survey (2006) and monitor survey (2012) are marked with vertical arrows, while the dashed lines represent the simulated profiles (black dash line), with 10% (blue color) and 20% (green color) increases and 20% (red color) decrease in porosity and the base model. The black points are the observed data.

The BHP profile for well P16 is shown in Figure 6.25. The results obtained after modifying the porosity indicate that none of these adjustments significantly improved the match between the simulated and observed BHP data. The overall trend of the observed pressure shows a decline, whereas the simulated BHP continues to increase in all cases. A similar pattern is observed for well P56 (Figure 6.26) .

As with well P8, these results suggest that further tuning of other reservoir parameters is necessary to resolve the discrepancies and improve the model's reliability.

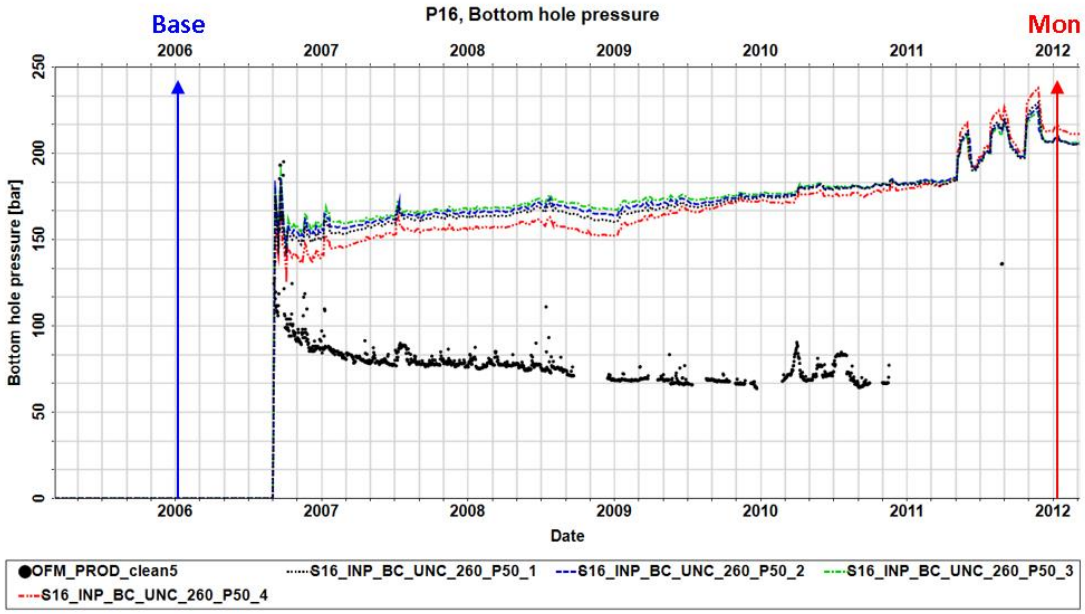

Figure 6.25: Bottom Hole Pressure profile for well P16 showing the observed and simulated pressures before (gray color curve) and after porosity modifications (blue, green and red color curves). The base seismic survey (2006) and monitor survey (2012) are marked with arrows, while the dashed lines represent the simulated profiles for each porosity modification and the base model. The black points are the observed data.

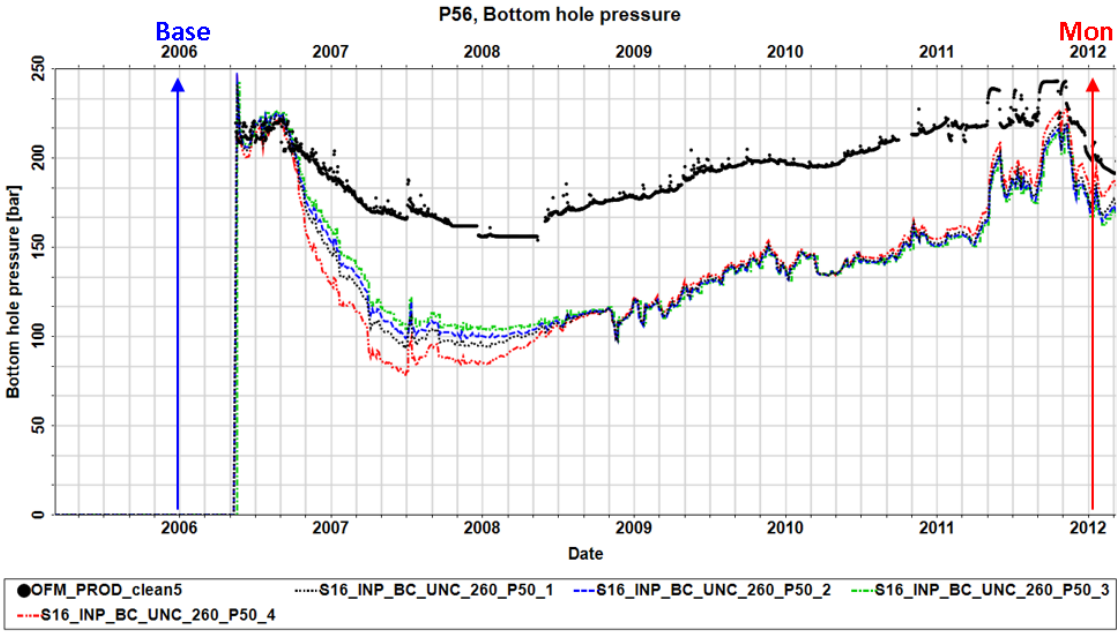

Figure 6.26: Bottom Hole Pressure profile for well P56 showing the observed and simulated pressures after porosity modifications. The base seismic survey (2006) and monitor survey (2012) are marked with vertical arrows, while the dashed lines represent the simulated profiles for each porosity modification and the base model. The black points are the observed data.

The analysis of porosity modifications on GOR of different wells (Figure 6.27, Figure 6.28 and Figure 6.29) shows that the simulated profiles exihibit a persistent mismatch between the observed and the simulated data indicating that these adjustments had minimal impact on improving alignment.

Regarding Qo (Figure 6.30, Figure 6.31 and Figure 6.32) , porosity modifications also resulted in small changes. However, for well P56 the outcomes showed mixed results, with some models demonstrating good alignment with the observed data while one model exhibited significant deviations, highlighting potential issues in capturing reservoir dynamics accurately at this location.

The Qw profiles (Figure 6.33, Figure 6.34 and Figure 6.35) demonstrated moderate alignment improvements with porosity increases, yet earlier mismatches remained unresolved.

Overall, the results indicate that porosity adjustments were insufficient to resolve discrepancies in the BHP, GOR, Qo, and Qw profiles. These findings suggest that additional factors, such as permeability or other dynamic reservoir properties, should be considered to improve model accuracy.

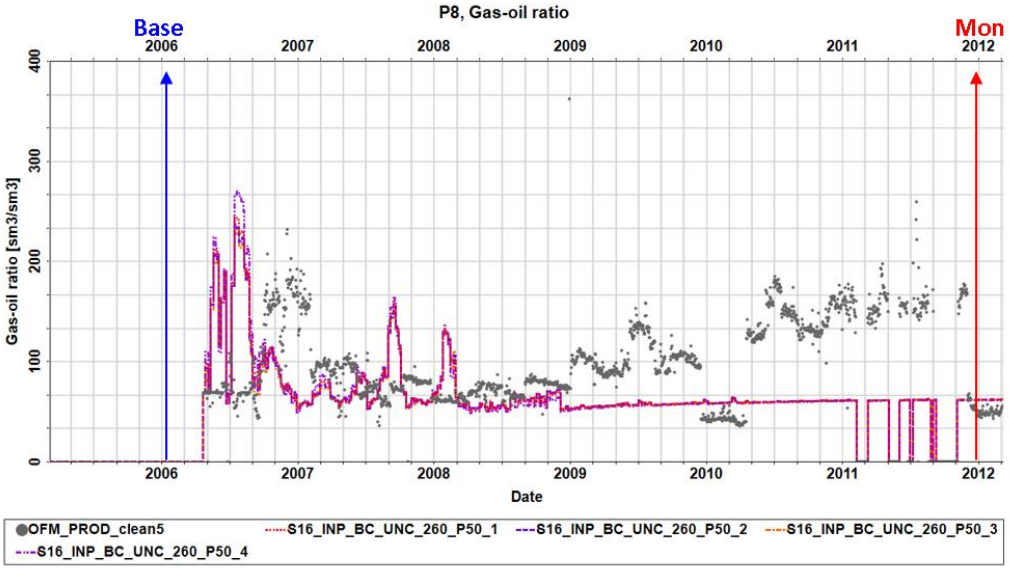

Figure 6.27: Gas-Oil Ratio profile for well P8, comparing the observed GOR with simulated profiles after porosity modifications (10% increase, 20% increase, and 20% decrease). The base seismic survey (2006) and monitor survey (2012) are marked with vertical arrows. The base model is represented by the red, cyan orange and purple color and the observed data by the gray points.

The simulated profiles show the persistent mismatch between observed and simulated data in later production years.

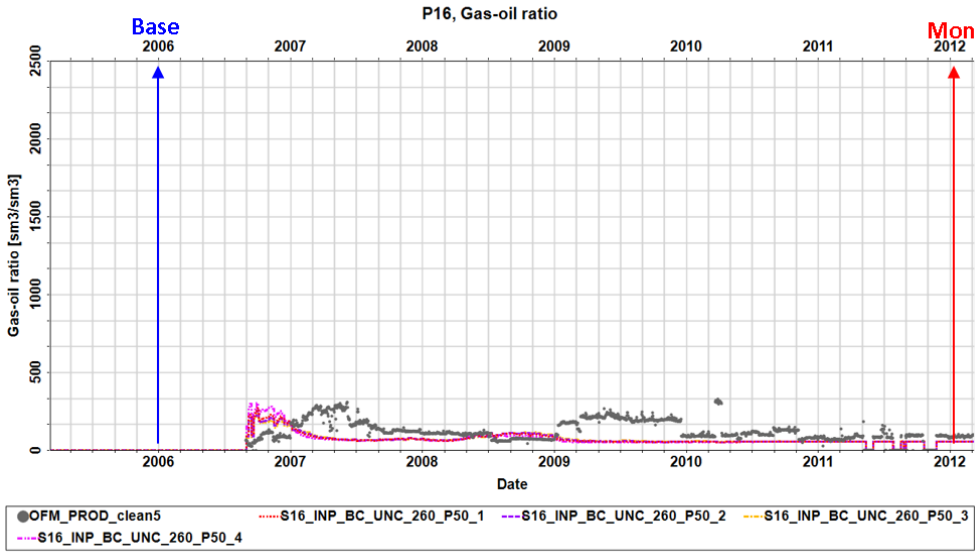

Figure 6.28: Gas-Oil Ratio profile for well P16, comparing the observed GOR with simulated profiles after porosity modifications (10% increase, 20% increase, and 20% decrease). The base seismic survey (2006) and monitor survey (2012) are marked with vertical arrows. The base model is represented by the red, cyan orange and purple color and the observed data by the gray points.

The simulated profiles show the persistent mismatch between observed and simulated data.

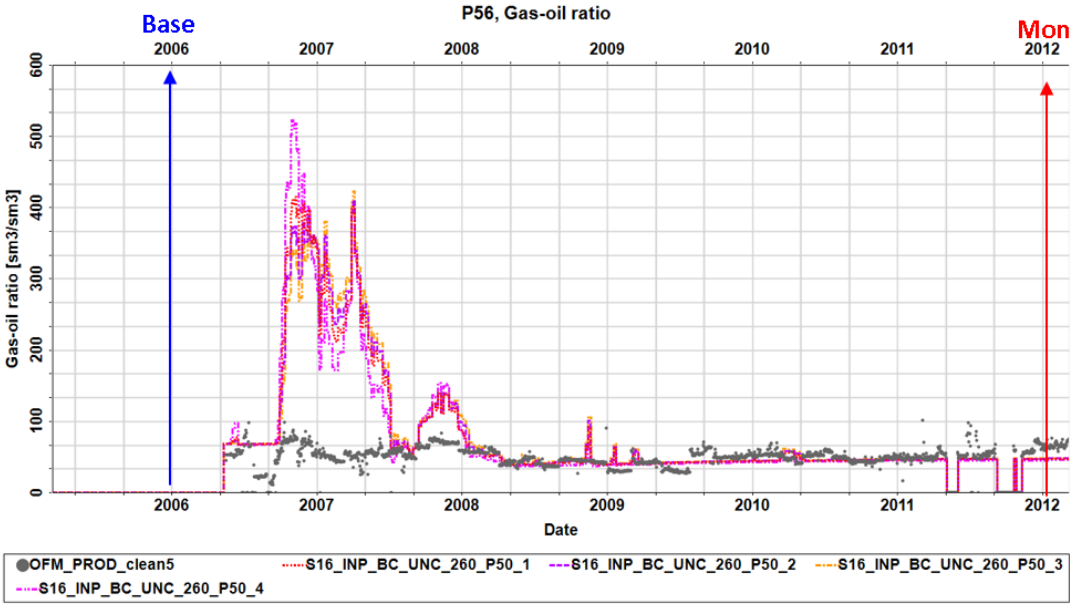

Figure 6.29: Gas-Oil Ratio profile for well P56, comparing the observed GOR with simulated profiles after porosity modifications (10% increase, 20% increase, and 20% decrease). The base seismic survey (2006) and monitor survey (2012) are marked with vertical arrows. The base model is represented by the red, cyan orange and pink color and the observed data by the gray points.

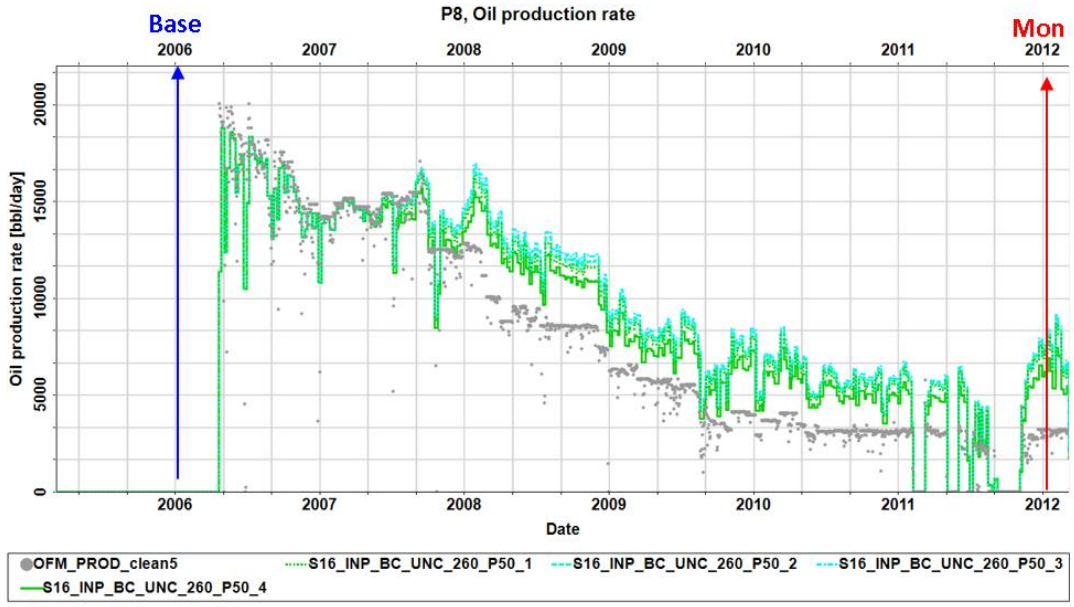

Figure 6.30: Oil production rate profile for well P8, comparing the observed (Qo) with simulated profiles after porosity modifications (10% increase, 20% increase, and 20% decrease). The base seismic survey (2006) and monitor survey (2012) are marked with vertical arrows. The base model is represented by the deep green (20% decrease, blue (20% increase, and light blue (10% increase) lines color and the observed data by the gray points.

The simulated profiles show the persistent mismatch between observed and simulated data in later production years.

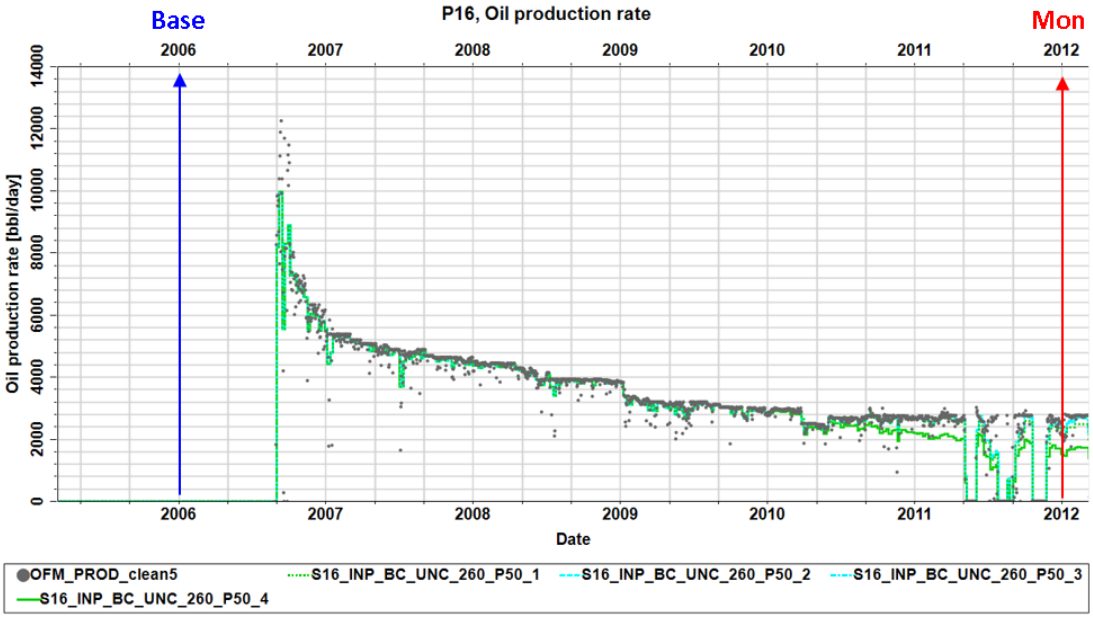

Figure 6.31: Oil production rate profile for well P16 showing the observed and simulated production rates after porosity modifications (10% increase, 20% increase, and 20% decrease).
The observed data is represented by black dots. The green dotted line represents the simulation for the base case, the cyan dashed line corresponds to the 10% and 20% porosity increase respectively, and the green dashed line represents the 20% porosity decrease. The base seismic survey (2006) and monitor survey (2012) are marked by the blue and red vertical arrows.

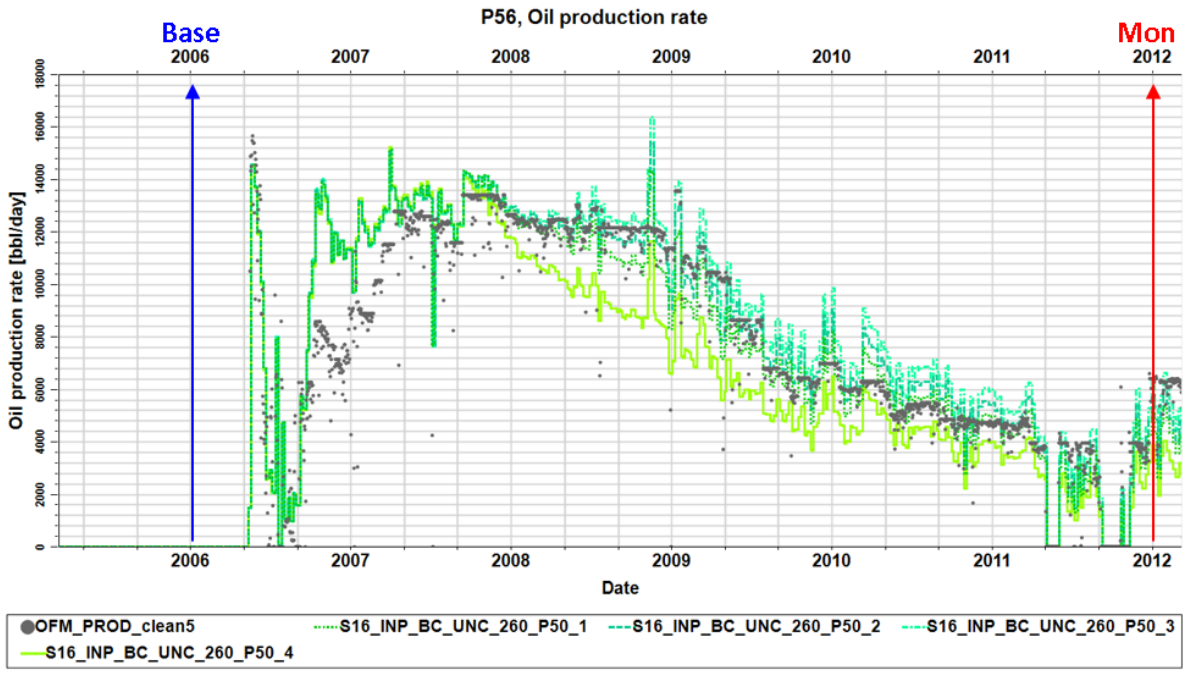

Figure 6.32: Oil production rate profile for well P56 showing the observed and simulated production rates after porosity modifications (10% increase, 20% increase, and 20% decrease).
The observed data is represented by black dots. The green dotted line represents the simulation for the base case, the cyan dashed line corresponds to the 10% and 20% porosity increase respectively, and the green dashed line represents the 20% porosity decrease. The base seismic survey (2006) and monitor survey (2012) are marked by the vertical arrows.

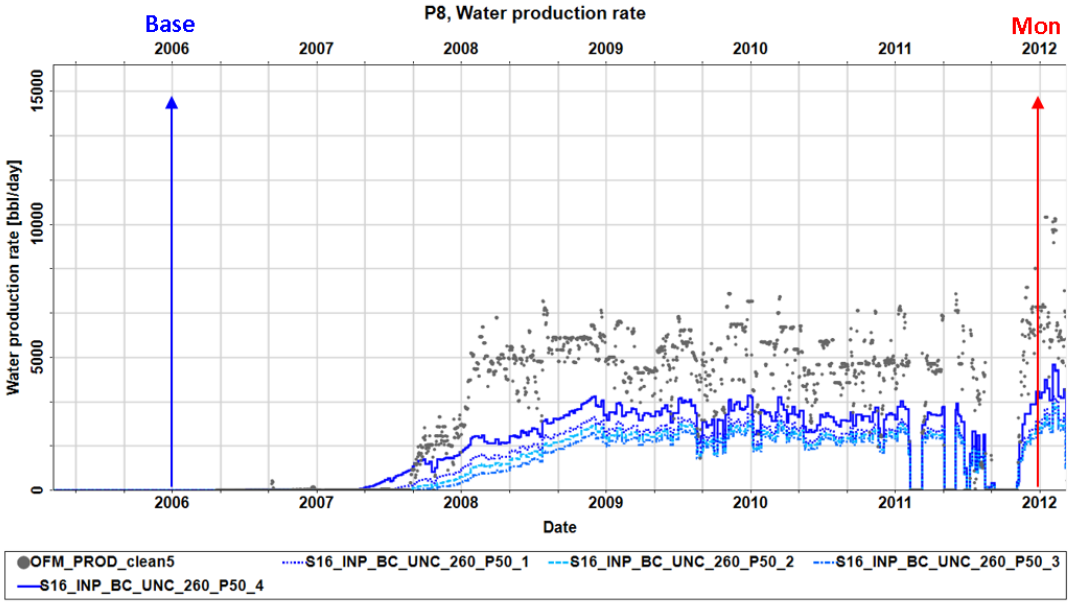

Figure 6.33: Water production rate profile for well P8 showing the observed and simulated production rates after porosity modifications (10% increase, 20% increase, and 20% decrease). The base seismic survey (2006) and monitor survey (2012) are marked, with the blue and red lines.

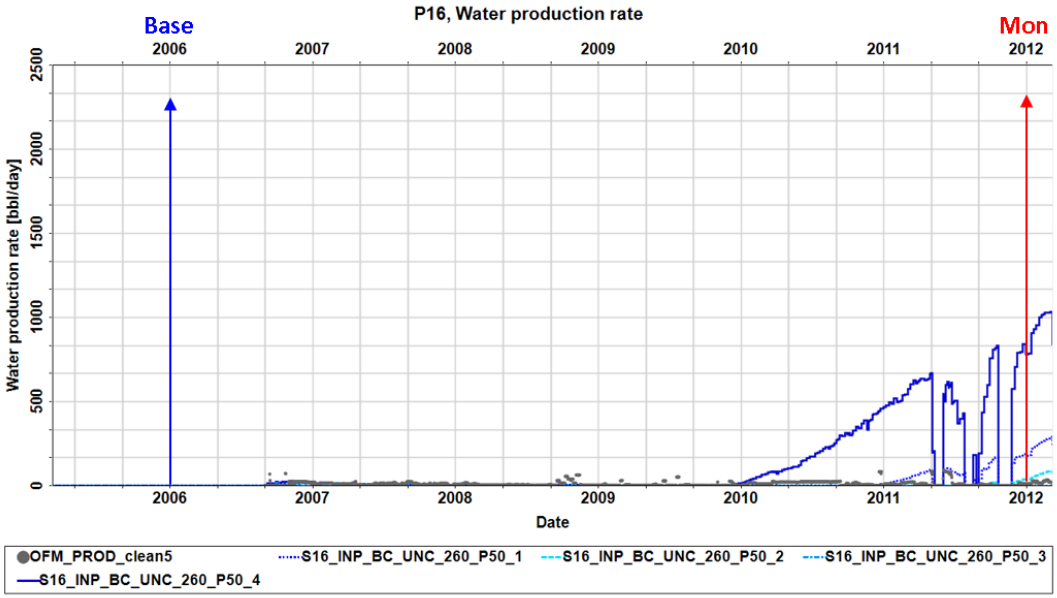

Figure 6.34: Water production rate profile for Well P16, showing observed and simulated production rates after porosity modifications: 10% increase (blue), 20% increase (light blue), and 20% decrease (dark blue). The blue and red lines represent base seismic survey (2006) and monitor survey (2012).

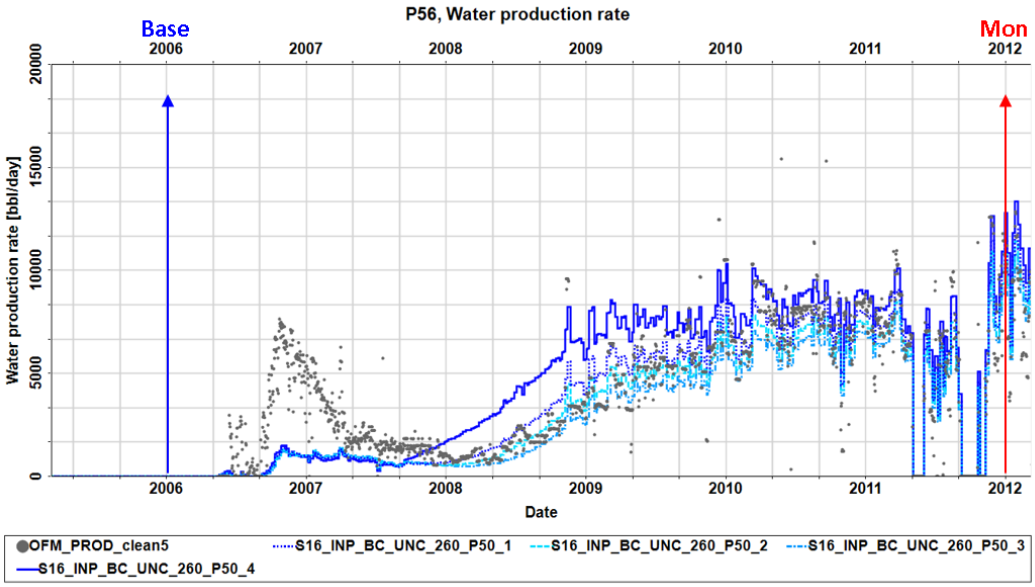

Figure 6.35: Water production rate (Qw) profile for well P56 showing the observed and simulated production rates after porosity modifications: 10% increase (blue), 20% increase (light blue), and 20% decrease (thick blue). The blue and red lines represent base seismic survey (2006) and monitor survey (2012).

6.7.3 4D seismic attribute evaluation after model modification and their relation with production profiles

Although satisfactory well matching could not be achieved through porosity modifications, the impact of these changes on the modeled 4D seismic responses was investigated. Previous analyses focused on the influence of manual model adjustments on production data. In this section, attention shifts to examining the modeled 4D seismic data. Following the porosity adjustments described earlier, the petro-elastic model was re-run to generate synthetic seismic attributes, specifically amplitude and impedance. These synthetic attributes were then compared with the observed 4D seismic data. The primary objective of this comparison was to evaluate whether the porosity modifications reduced the mismatch between the modeled and observed seismic responses.

Figure 6.36 presents the difference root mean square (dRMS) maps for both observed and modeled amplitude data (with no noise added), including the initial model and the models after modifying porosity by 20% increase and 20% decrease. These maps were generated for the interval ranging from top to base of the AB140 zone.

The initial modeled map (Figure 6.36b) shows a predominantly blue-dominated amplitude response, indicating regions of hardening. Porosity modifications (±20%, Figure 6.36d and c) did not improve the match between the observed and modeled maps.

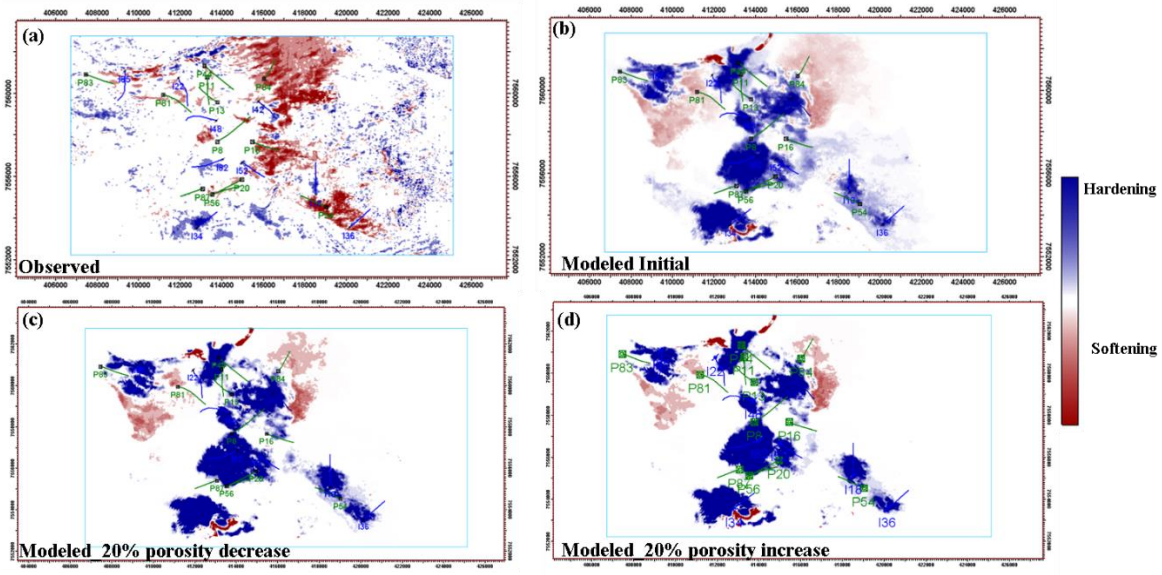

Figure 6.36: Comparison of observed and modeled dRMS amplitude maps for the AB140 reservoir. (a) Observed; (b) Modeled for the initial reservoir model; (c) Modeled after a 20% porosity decrease;(d) Modeled after a 20% porosity increase.

Figure 6.37 illustrates the dRMS amplitude maps, with the observed data showing significant reservoir softening (red region) around well P8, likely caused by gas replacing oil or water and/or pore pressure increase, as indicated by the red arrow (Figure 6.37a). However, the modeled dRMS map (Figure 6.37c) predominantly shows hardening (blue regions) also marked by the red arrow, reflecting the model's inability to capture the observed dynamic behavior. The pressure difference map (Figure 6.37d) indicates minimal pressure changes around well P8, suggesting that the hardening in the modeled data is primarily driven by an increase in water saturation (Sw). These findings highlight the limitations of the model in accurately replicating reservoir dynamics.

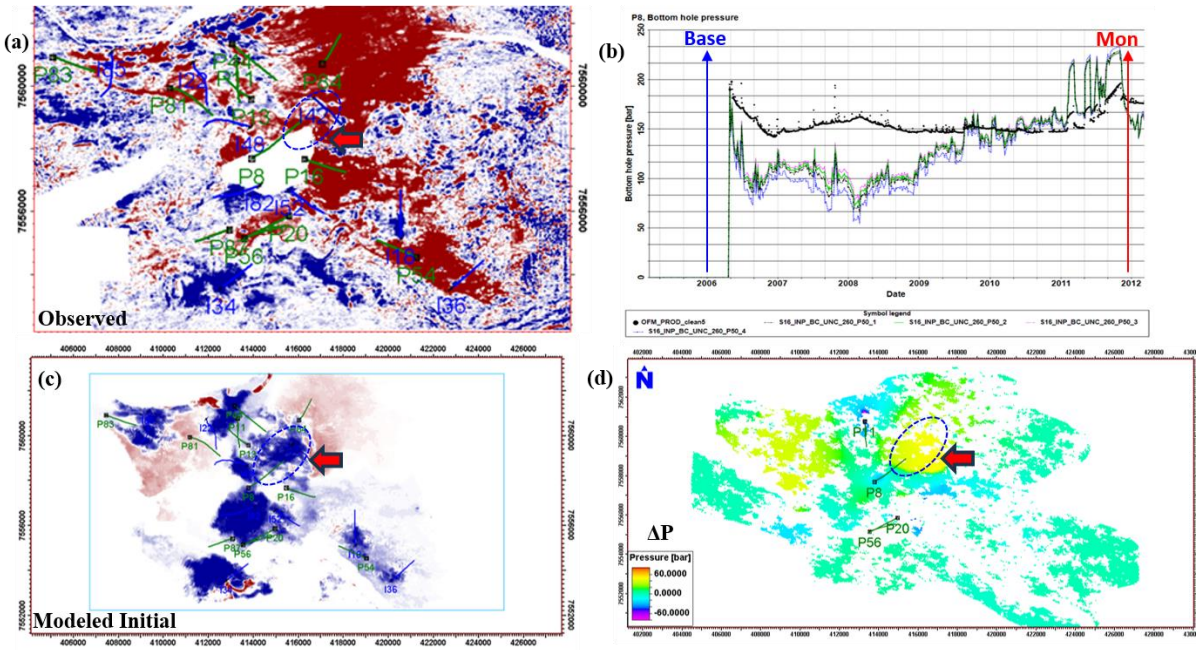

Figure 6.37: Comparison of observed and modeled reservoir dynamics at Well P8: (a) observed dRMS amplitude map showing a softening anomaly around well P8; (b) BHP profile for well P8; (c) initial modeled dRMS amplitude map showing hardening effects in the same region; (d) pressure diference map (ΔP) showing pore pressure increase around well P8. The red arrow highlights regions where the observed and modeled dRMS responses differ, indicating softening in (a) and hardening in (c). The blue ellipse, present in (a), (c), and (d), marks the region where pressure variations influence the reservoir behavior.

Despite porosity modifications, the modeled dRMS response remained largely unchanged. The observed softening in the dRMS data was not captured in the modeled response, which continued to show hardening effects. This indicates that porosity changes alone did not improve the alignment between modeled and observed responses.

7 CONCLUSION

This study examines time-lapse seismic modeling using various forward modeling techniques to compare their ability to capture 4D seismic effects and reservoir property changes over time. The research reservoir is a deep-water turbidite field situated in Brazil.

Three distinct modeling approaches were compared: FMCOU, FMIOU, and FMFI. FMCOU simplifies the process by assuming a constant acoustic impedance for the overburden and underburden intervals, while FMIOU enhances this by incorporating inversion results for these same intervals. FMFI combines inversion outcomes for baseline seismic data with petroelastic modeling for the monitor survey.

Although all three has their uniqueness in terms of 3D amplitude results, FMIOU and FMFI offered a more detailed and accurate representation of the subsurface, particularly with respect to overburden and underburden. Modeling these intervals with inversion results brought real effects of wave propagation phenomena and acquisition issues happening in the field, significantly influencing the 3D amplitude analysis. However, a distinct drawback of both methodologies is the requirement to perform a seismic inversion, which can be computationally expensive and may take several months to be run. In this context, FMCOU emerges as an alternative method due to its simplicity, efficiency, and cost-effectiveness, especially in scenarios where time and budget constraints are a priority. We also recommend avoiding the FMFI approach when there are uncertainties in the velocity model, as misalignments between observed and modeled data could introduce seismic artifacts in the 4D analysis.

In the 4D seismic analysis, the different modeling approaches did not produce substantial variations. All approaches yielded comparable outcomes, allowing for direct comparison with observed seismic amplitudes. This 4D analysis highlighted inconsistencies in certain regions between the model and observed data, indicating areas where the model requires updating or where the seismic data is uncertain (too noisy).

This mismatch was also confirmed in the dRMS map analysis, which showed a considerable difference between the modeled and observed seismic responses. The observed data was dominated by softening regions (red), while the modeled cases exhibited mostly hardening areas (blue). The importance of noise modeling cannot be overstated. When seismic inversion results are utilized in time-lapse seismic forward modeling, incorporating noise

through residuals has demonstrated greater advantage compared to the addition of random noise.

This approach plays a pivotal role in enhancing the comparison between modeled and observed seismic data.The assessment of production data matching also supported the idea of a model mismatch. For all variables, especially BHP, GOR, and Qw, most wells showed significant discrepancies between the simulated and the observed data. Aiming to improve production and 4D seismic data matching, there were made manual modifications to the model. More specifically, we applied different multipliers in the porosity.

Adjusting porosity by 10% and 20% increases or 20% decreases did not result in significant improvement in the production match between observed and simulated data. Across all parameters, the model consistently failed to reflect the observed reservoir behavior. This further emphasized the model's inability to capture dynamic fluid flow and pressure depletion behavior.

The poor 4D seismic data matching also remained after the porosity adjustments. Through the dRMS map comparisons, we observed that the modeled maps did not fully capture the observed softening signals, as they continued to exhibit hardening effects. This discrepancy highlights the need for further refinement in the model to improve consistency with the seismic observations.

It is important to note that a more robust data assimilation processcould potentially enhance the model's accuracy. However, implementing such a methodology is beyond the scope of this study This study discusses the diverse stages of employing 4D seismic data to evaluate and improve the accuracy of simulation models, emphasizing the integration of noise modeling, seismic attributes, and production data to refine the reservoir model's accuracy and reliability.

7.1 Suggestion for future work

This study primarily focused on the use of porosity modifications to improve model's mismatches. Future research could expand upon this by incorporating additional modeling parameters beyond porosity to improve the match between observed and simulated data.

Integrating advanced techniques such as assisted algorithms for seismic history matching can provide further insights into reservoir properties, particularly saturation estimates. Including angle stacks of seismic data in future studies may also help decouple the effects of pressure and saturation, leading to more precise interpretation of 4D seismic data.

For the FMFI modeling approach, it is suggested that future studies could add the relative impedance changes of PEM, instead of the absolute differences, to the inverted baseline data. This approach can be more appropriate since it avoids errors caused by different balancing between inverted and modeled results.

Additionally, repeating this analysis with different simulation models could reveal biases in current reservoir models and offer valuable insights into the role of seismic data in reservoir history matching. This approach could help quantify the impact of 4D seismic data on improving model reliability and support decision-making for field development strategies.

REFERENCES

ALLO, F., RIFFAULT, D., DOYEN, P., NUNES, J. P., DOS SANTOS, M. S., & JOHANN, P. (2013). Reducing turn-around time for time-lapse feasibility studies. In 13th International Congress of the Brazilian Geophysical Society & EXPOGEF, Rio de Janeiro, Brazil, 26–29 August 2013 (pp. 1013-1018). Society of Exploration Geophysicists and Brazilian Geophysical Society. https://doi.org/10.1190/sbgf2013-210.

ALLO, F. (2019). Consolidating rock-physics classics: A practical take on granular effective medium models. The Leading Edge, 38(5), 334-340.

AMINI, H. (2014). A pragmatic approach to simulator-to-seismic modelling for 4D seismic interpretation (Doctoral Thesis, Heriot-Watt University).

AMINI, H., MACBETH, C., & SHAMS, A. (2020). Seismic modelling for reservoir studies: a comparison between convolutional and full-waveform methods for a deep-water turbidite sandstone reservoir. Geophysical Prospecting, 68(5), 1540-1553.

BATZLE, M., & WANG, Z. (1992). Seismic properties of pore fluids. Geophysics, 57(11), 1396–1408. https://doi.org/10.1190/1.1443207.

BYBEE, K. (2006). Albacora Leste field development: reservoir aspects and development strategy. Journal of petroleum technology, 58(10), 53-55. doi: https://doi.org/10.2118/1006-0053-JPT.

CALVERT, R. (2005). Insights and methods for 4D reservoir monitoring and characterization. Society of Exploration Geophysicists and European Association of Geoscientists and Engineers..

CALVERT, M. A., HOOVER, A. R., VAGG, L. D., OOI, K. C., & HIRSCH, K. K. (2016). Halfdan 4D workflow and results leading to increased recovery. The Leading Edge, 35(10), 840–848. https://doi.org/10.1190/tle35100840.1.

CAVALCANTE, C. C., MASCHIO, C., SANTOS, A. A., SCHIOZER, D., & ROCHA, A. (2017). History matching through dynamic decision-making. PLoS ONE, 12(6), e0178507. https://doi.org/10.1371/journal.pone.0178507.

CERVENÝ, V. (2001). Seismic ray theory (Vol. 110). Cambridge: Cambridge university press.

CHAPMAN, C. (2004). Fundamentals of seismic wave propagation. Cambridge University Press. https://doi.org/10.1017/CBO9780511616835.

DANAEI, S., NETO, G. M. S., SCHIOZER, D. J., & DAVOLIO, A. (2022). Substituting petro-elastic model with a new proxy to assimilate time-lapse seismic data considering model errors. Journal of Petroleum Science and Engineering, 210, 109970. DOI: 10.1016/j.petrol.2021.109970.

DAVOLIO, A., MASCHIO, C., & SCHIOZER, D. J. (2013). Local history matching using 4D seismic data and multiple models combination. In SPE Europec featured at EAGE Conference and Exhibition (pp. SPE-164883). SPE.

DAVOLIO, A., SANTOS, J. M. C. D., ROSA, D. R., DEIRÓ, N. F. R., SILVA, E., NETO, G. S., & SCHIOZER, D. J. (2021). 4D seismic detectability on a pre-salt like reservoir. In Second EAGE Conference on Pre-Salt Reservoir (Vol. 2021, No. 1, pp. 1-5). European Association of Geoscientists & Engineers.

DEPLANTE, C., COSTA, M., & SANTOS, M. S. (2019). Using full wave seismic modeling to test 4D repeatability for Libra pre-salt field. In 16th International Congress of the Brazilian Geophysical Society. Rio de Janeiro: Sociedade Brasileira de Geofísica.

DILLON, L., SCHWEDERSKY, G., NUNES, C., DE MELO FILHO, L., ROISENBERG, H., & DAVOLIO, A. (2023). Optimizing the 4D QI process – A Brazilian turbidite case study. 18th International Congress of the Brazilian Geophysical Society & Expogef, October 16-19, Rio de Janeiro, Brazil.dos Santos, M. S. (2015). Processo integrado de caracterização de incertezas para estudos de valoração da sísmica 4D. Doctoral dissertation, Universidade Estadual de Campinas, UNICAMP.

DVORKIN, J., & NUR, A. (1996). Elasticity of high-porosity sandstones: Theory for two North Sea data sets. Geophysics, 61(5), 1363–1370.

EMERICK, A. A. (2016). Analysis of the performance of ensemble-based assimilation of production and seismic data. Journal of Petroleum Science and Engineering, 139, 219–239.

FAHIMUDDIN, A., AANONSEN, S. I., & SKJERVHEIM, J. A. (2010). Ensemble based 4D seismic history matching: Integration of different levels and types of seismic data. In SPE Europec featured at EAGE Conference and Exhibition (pp. SPE-131453). SPE.

FICHTNER, A. (2011). Full seismic waveform modelling and inversion. Springer Science & Business Media.. https://doi.org/10.1007/978-3-642-15807-0.

FORMENTO, J.L., DOS SANTOS, M. S., SANSONOVSKI, R. C., JUNIOR, N. M. D. S. R., & VASQUEZ, G. F. (2007). 4D seismic modeling workflow over the Marlim field. In 10th International Congress of the Brazilian Geophysical Society (pp. cp-172). European Association of Geoscientists & Engineers.https://doi.org/10.1190/sbgf2007-473.

GASSMANN, F. (1951). Elastic waves through a packing of spheres. Geophysics, 16(4), 673-685.

JOHNSTON, D. H. (2013). Practical applications of time-lapse seismic data. Society of Exploration Geophysicists. https://doi.org/10.1190/1.9781560803126.

KRAGH, E. D., & CHRISTIE, P. (2002). Seismic repeatability, normalized RMS, and predictability. The Leading Edge, 21(7), 640-647.

Lemos, W.P., de Castro, M.R. Lemos, W. P., Baião de Castro, M. R., Soares, C. M., Rosalba, J. F., & Meira, A. A. G. (2006). Albacora Leste Field Development: Reservoir Aspects and Development Strategy. Presented at the Offshore Technology Conference, Houston, Texas, USA, May 2006. doi: https://doi.org/10.4043/18056-MS.

MALEKI, M., DAVOLIO, A., & SCHIOZER, D. J. (2018). Qualitative time-lapse seismic interpretation of Norne Field to assess challenges of 4D seismic attributes. The Leading Edge, 37(10), 754-762. https://doi.org/10.1190/tle37100754.1.

MASCHIO, C., & SCHIOZER, D. J. (2016). Probabilistic history matching using discrete Latin Hypercube sampling and nonparametric density estimation. Journal of Petroleum Science and Engineering, 147, 98-115.Mavko, G., Mukerji, T., & Dvorkin, J. (2020). The rock physics handbook. Cambridge university press.

MELLO, V. L. D., SANTOS, M. S. D., PENNA, R. M., ROSSETO, J. A., & DEPLANTE, C. (2019). 4D Petroelastic Modeling for a Brazilian Pre-Salt Field: What to Expect From Interpretation? In 81st EAGE Conference and Exhibition 2019 (Vol. 2019, No. 1, pp. 1-5). European Association of Geoscientists & Engineers. https://doi.org/10.3997/2214-4609.201901401.

MUKERJI, T., & DVORKIN, J. (1998). The rock physics handbook: Tools for seismic analysis in porous media. Cambridge University Press.

NUR, A., MAVKO, G., DVORKIN, J., & GALMUDI, D. (1998). Critical porosity: A key to relating physical properties to porosity in rocks. The Leading Edge, 17(3), 357-362. doi: 10.1190/1.1437977.

OLIVEIRA, R. M. (2008). The Marlim field: incorporating 4D seismic in reservoir-management decisions. Journal of Petroleum Technology, 60(04), 52-110.

RIBEIRO, C., REISER, C., DOYEN, P., LAU, A., & ADILETTA, S. (2007). Time-lapse simulator-to-seismic study-Forties field, North Sea. In SEG International Exposition and Annual Meeting (pp. SEG-2007). SEG. https://doi.org/10.1190/1.2793082

ROSA, D. R., SCHIOZER, D. J., & DAVOLIO, A. (2023). Evaluating the impact of 4D seismic data artefacts in data assimilation. Petroleum Geoscience, 29(3), petgeo2022-069. https://doi.org/10.1144/petgeo2022-069.

ROSA, D., DOS SANTOS, M. S., SCHWEDERSKY, G., PILATO, M., PINHEIRO, C., DE MELO FILHO, L. S., & DAVOLIO, A. (2024). Best Practices on Forward 4D Seismic Modelling from Dynamic Reservoir Models. In 85th EAGE Annual Conference & Exhibition (including the Workshop Programme) (Vol. 2024, No. 1, pp. 1-5). European Association of Geoscientists & Engineers.

Santos, J. M. C., Rosa, D. R., Schiozer, D. J., & Davolio, A. (2022). Fast diagnosis of reservoir simulation models based on 4D seismic similarity indicators. Journal of Petroleum Science and Engineering, 210, 110083.

SIMM, R., & BACON, M. (2014). Seismic amplitude: An interpreter's handbook. Cambridge university press.

Neto, G.M.S., Davolio, A., & Schiozer, D.J. (2021). Assimilating time-lapse seismic data in the presence of significant spatially correlated model errors. Journal of Petroleum Science and Engineering, 207, 109127.

Oliver, D. S., Fossum, K., Bhakta, T., Sandø, I., Nævdal, G., & Lorentzen, R. J. (2021). 4D seismic history matching. Journal of Petroleum Science and Engineering, 207, 109119.

STAMMEIJER, J. G. F., & HATCHELL, P. J. (2014). Standards in 4D feasibility and interpretation. The Leading Edge, 33(2), 134-140.

WEBB, B., RIZZETTO, C., PIRERA, F., PAPAROZZI, E., MILLUZZO, V., MASTELLONE, D., ... & BERTARINI, M. (2019). 4D seismic opportunity: from feasibility to reservoir characterization–a case study offshore West Africa. First Break, 37(2), 69-77.